Image reconstruction of physiological edema using electrical impedance tomography (EIT) with ratiometric preprocessing and Sparse Bayesian Learning (SBL)

レシオメトリック前処理とスパースベイズ学習(SBL)を用いた電気インピーダンストモグラフィ（EIT）法による生体浮腫の画像再構成

February 2023

Ryoma Ogawa
小川 良磨

Graduate School of Science and Engineering
CHIBA UNIVERSITY

(千葉大学審査学位論文)

Image reconstruction of physiological edema using electrical impedance tomography (EIT) with ratiometric preprocessing and Sparse Bayesian Learning (SBL)

レシオメトリック前処理とスパースベイズ学習(SBL)を用いた電気インピーダンストモグラフィ（EIT）法による生体浮腫の画像再構成

February 2023

Ryoma Ogawa
小川 良磨

Graduate School of Science and Engineering
CHIBA UNIVERSITY

Abstract

Monitoring volume/concentration balance in the extracellular fluid (ECF) is critical to maintaining physiological wellbeing because fluctuated volume/concentration beyond normal level causes physiological edema. Electrical impedance tomography (EIT) has recently attracted increasing attention as an alternative to the above conventional monitoring modalities because EIT is able to monitor both "spatio" and "temporal" (spatiotemporal) change of components volume/concentration in ECF as well as easy operation, non-invasive, harmless, low cost, and capable of real-time monitoring. EIT injects an alternating current I through a sensor consisting of several electrodes placed around the periphery and reconstructs a conductivity distribution $\boldsymbol{\sigma}$ from a measured impedance $\mathbf{Z}$. However, to date, there has been little investigation on physiological edema by EIT. Moreover, conventional EIT suffers from image deterioration in the case of high conductivity contrast of biological tissue between the region of interest (ROI) (e.g., subcutaneous adipose tissue) and background (e.g., muscle), as well as the excess amount of measurement noise. Furthermore, local-spatiotemporal change (LSTC) is not accurately monitored by conventional EIT in the unstable-background fields where the background conductivity changes more significantly than the LSTC in ROI. Therefore, the aims are obtained through systematic stages of the following objectives: 1) Investigation of physiological edema on $\boldsymbol{\sigma}$ in lower leg subcutaneous tissue; 2) Investigation of the relationship between frequency-dependence and absolute conductivity value in the reconstructed image through the miniature EIT sensor as fundamental research towards developing data preprocessing; 3) Development of multifrequency EIT (*mf*-EIT) with a ratiometric preprocessing for boosting robustness under high conductivity contrast of biological tissue and suppressing excessive noise; 4) Monitoring of local-spatiotemporal change (LSTC) in the extracellular fluid (ECF) by time-variation-constraint sparse Bayesian learning (*tvc*SBL) implemented into frequency-difference EIT (*fd*EIT).

Firstly, the investigation of physiological swelling on $\boldsymbol{\sigma}$ in lower leg subcutaneous tissue by EIT is explained in this thesis. There is a strong need for a non-invasive monitoring technique that can accurately assess the physiological condition change or heterogeneity of subcutaneous adipose tissue (SAT) by localizing the abnormalities within the compartment. Here, the image-based reference EIT (IBR-EIT) with fat-weighted threshold method has been proposed in order to assess the interstitial fluid in SAT as an improvement of bioelectrical

impedance spectroscopy (BIS). The proposed method is evaluated by a physiological swelling experiment with a wearable 16 EIT electrodes sensor where BIS is applied as a comparative method. The experimental results show that the proposed IBR-EIT appears to identify the physiological swelling condition and effectively remove the unexpected background noise. Furthermore, the conductivity variation in SAT shows a good correlation with extracellular water volume change measured by BIS; the correlation coefficient R^2 = 0.927. In conclusion, the proposed method provides a great prospect for SAT assessment.

Secondly, the investigation of the relationship between frequency-dependence and absolute conductivity value in the reconstructed image is explained in this thesis through the miniature EIT sensor as fundamental research towards the development of data preprocessing. The use of 3D cell culture for tissue engineering and regenerative medicine applications often challenges conventional biochemical and optical assays. Impedance-based cellular assays have shown their potential to retrieve dielectric parameters about cell behavior, such as viability, proliferation, and differentiation for 2D adherent cell culture. Herein, simultaneous 3D impedance imaging and viability measurements of multiple large (>2mm) 3D cell cultures embedded in collagen gels are demonstrated. The method is facilitated by low-resistance 3D printed scaffolds that can hold a 3D cell–gel system throughout cell culture while being transparent to impedance imaging. It is shown in silico and in vitro that frequency-difference electrical impedance tomography (*fd*EIT) can nondestructively and in a label-free way differentiate a variety of cell concentrations with a single miniature sensor in real time. Moreover, the relationships between frequency-dependence and absolute conductivity value in *fd*EIT image are numerically explained using multiple samples. This study paves the way toward developing *fd*EIT imaging for the quantitative and noninvasive evaluation of tissue engineering products.

Thirdly, the development of multifrequency EIT (*mf*-EIT) with a ratiometric preprocessing for boosting robustness under high conductivity contrast of biological tissue and suppressing excessive noise is explained in this thesis. In addition to the micro-scale *fd*EIT as a cellular assay, the macro-scale *fd*EIT as point-of-care imaging is highly desired since reference data over time is not necessary. Reconstructing the structural images of human body compartments could be possible using electrical impedance tomography (EIT), but the reconstructed image deteriorates due to high conductivity contrast μ between anomaly and background. In this chapter, a multifrequency EIT with a ratiometric preprocessing (ratiometric EIT) has been developed in order to minimize μ while maintaining high

distinguishability without any *a priori* information. The preprocessing of ratiometric EIT is achieved by extending the framework of ratiometric methods that uses the ratio of two measurement signals. Based on the proposed ratiometric preprocessing, ratiometric frequency-difference adjacent EIT (*rfda*-EIT) is newly derived. The *rfda*-EIT is qualitatively and quantitatively evaluated by numerical simulation under the variant conditions of μ (= 95%-10%) and experiment with eight subjects' calves. As the results, the *rfda*-EIT scores the area ratio error of subcutaneous adipose tissue (SAT) 17.09% < ARE^{SAT} < 28.13%, the position error of bone tibia 0.14% < PE^{tibia} < 10.19%, the position error of bone fibula 9.51% < PE^{fibula} < 1.74%, and the correlation coefficients 0.79 < CC < 0.91 in the numerical simulation. The total-mean area ratio error <ARE^{SAT}> by the *rfda*-EIT is lower than the error by the classical frequency-difference adjacent EIT (*fda*-EIT) from 12.70% to 5.18% in the experiment. Moreover, the true positive rate TPR^{tibia} for the bone tibia detection by the *rfda*-EIT is increased from 50.0% to 87.5% as compared with the rate by the *fda*-EIT.

Fourthly, the monitoring of local-spatiotemporal change (LSTC) in the extracellular fluid (ECF) by time-variation-constraint sparse Bayesian learning (*tvc*SBL) implemented into frequency-difference EIT (*fd*EIT) is explained in this thesis. Local-spatiotemporal change (LSTC) of frequency-difference conductivity distribution $\Delta\boldsymbol{\sigma}$ in extracellular fluid (ECF) has been monitored in subcutaneous adipose tissue (SAT) to evaluate leg edema by time-variation-constraint sparse Bayesian learning (*tvc*SBL) implemented into frequency-difference electrical impedance tomography (*fd*EIT) (*tvc*SBL-*fd*EIT). The *tvc*SBL-*fd*EIT has three steps which are Step 1: formulation of blocked column vector (BCV), Step 2: SAT separation by time variation constraint, and Step 3: temporal correlation extraction by hyperparameter learning. The *tvc*SBL-*fd*EIT is qualitatively and quantitatively evaluated by numerical simulation under the unstable-background fields and experiment with 15 subjects' calves. Two types of numerical simulations are conducted to model lymphedema (LE) and venous edema (VE) that cause LSTC in $\boldsymbol{\sigma}$ of subcutaneous tissue fluids in human calf phantom which consists of three parts: great saphenous vein (GSV) as ROI and SAT and muscle as background. From the results, LSTC in $\boldsymbol{\sigma}$ are clearly extracted only near GSV by the proposed method, even in a field where the time-varying $\boldsymbol{\sigma}$ in the background is large. Furthermore, the accuracy of the proposed method is evaluated under the variant conditions of conductivity ratios of SAT and muscle relative to GSV, i.e., $\rho^{GSV/SAT}$ and $\rho^{GSV/muscle}$, respectively, and area ratio accuracy ARA^{GSV} is the highest in the case where $\rho^{GSV/SAT} = \rho^{GSV/muscle}$, which achieves $ARA^{GSV} = 2.241$ regardless of the values of $\rho^{GSV/SAT}$ and $\rho^{GSV/muscle}$.

Moreover, the *tvc*SBL-*fd*EIT was applied to the monitoring of 15 subjects' calves along with an experimental protocol of prolonged standing and leg elevation. The spatial-mean conductivity $<\Delta\boldsymbol{\sigma}>^{SAT}$ in the separated SAT has a strong positive correlation with conventional impedance z^{BIA} by bioelectrical impedance analysis (BIA) (correlation coefficient $0.715 < R < 0.957$; $n = 15$, $p < 0.05$), which is decreased during the prolonged standing while $<\Delta\boldsymbol{\sigma}>^{SAT}$ is increased during the leg elevation. Frequency-dependency of $\Delta\boldsymbol{\sigma}$ is associated with LSTC of sodium ion concentration in ECF while the local maximum position of $\Delta\boldsymbol{\sigma}$ is associated with the great saphenous vein (GSV) position. Furthermore, the superiority of the proposed algorithm is numerically evaluated under the unstable-background fields.

In summary, extracellular fluid (ECF) in subcutaneous adipose tissue (SAT) has been monitored for evaluating physiological edema by 1) investigating conductivity distribution $\boldsymbol{\sigma}$ as a preliminary study, 2) investigating the relationship between frequency-dependence and absolute conductivity value in frequency-difference electrical impedance tomography (*fd*EIT) image, 3) developing multifrequency EIT (*mf*-EIT) with a ratiometric preprocessing, and 4) implementing time-variation-constraint sparse Bayesian learning (*tvc*SBL) into *fd*EIT to reconstruct local-spatiotemporal change (LSTC) as a detailed evaluation.

Table of Contents

Chapter 1 Introduction

1. Introduction

1.1. Physiological edema

More than 60% of the human body consists of fluid, which is roughly categorized into the intracellular fluid (ICF) and extracellular fluid (ECF), separated by cell membranes. Moreover, the ECF is categorized into interstitial fluid and plasma, separated by the capillary walls. While the ICF is mainly responsible for metabolic reactions, such as energy production and protein synthesis, the ECF is mainly responsible for the regulation of circulating blood flow, which transports nutrients and oxygen to the cells and transports waste products and carbon dioxide to outside the cells. Fluid volume is balanced mainly by regulating circulating blood flow, and once its balance is disrupted, edema develops. **Figure 1.1** shows the human circulatory system based on transcapillary fluid dynamics, where plasma filtered through the capillaries is reabsorbed directly to the blood vessels, whereas the remaining in the interstitial fluid is returned by the lymphatic system [1]. The fluid exchange is balanced by hydrostatic pressure P and osmotic pressure π, which determines the direction of fluid flow between the capillaries and the interstitium [2]–[4]. Since the development of edema is due to abnormalities in either or both parameters (P and π), such as increased capillary hydrostatic pressure P due to venous stasis and increased interstitial oncotic pressure π due to protein retention in subcutaneous tissue, the mechanisms of edema are quite diverse resulting in a

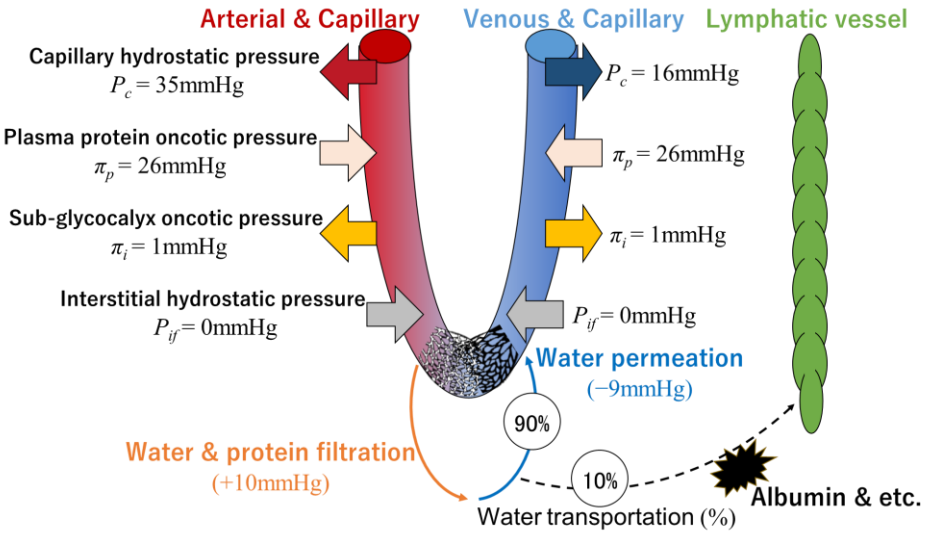

Figure 1.1 Overview of transcapillary fluid dynamics.

Table 1.1. Types of edematous disorders.

Generalized edema	Regional edema
• Cardiac disease • Renal disease • Chronic Venous Insufficiency • Hepatic disease • Elderly edema • Lipedema • Malnutrition • Pregnancy/premenstrual • Idiopathic edema • Medication • Orthostatic edema	• Lymphedema • Deep venous thrombosis • Post thrombotic syndrome • Varicose vein • Compartment Syndrome • Arthritis • Presence or recurrence of cancer

variety of edematous disorders, as shown in **Table 1.1**. There are two major types of edematous disorders, 1) Generalized edema, which is mainly treated by internal medicine and rarely a target for treating the edema itself, whereas 2) Regional edema is often a target for treating the edema itself. In most cases of regional edema, a typical example is lymphedema, a bilateral difference is observed as a clinical finding. Since our final goal is the early diagnosis of lymphedema, the following paragraphs focus specifically on lymphedema, among other types of physiological edema.

Lymphedema is a swelling of arms or legs due to the fluid accumulation in the interstitium containing high concentrations of albumin and other proteins that are not collected in the lymph vessels, which is known as severely reducing quality of life (QOL) disease. The lymphatic disorder is often the result of regional lymph node dissection (LND), postoperative irradiation, and taxane-based chemotherapy [5], [6], with a high incidence of lymphedema at around 15.5% [7]. In total, lymphedema is reported to affect 0.2 million in Japan, 1.2 million in Africa and Southeast Asia, and 40 million worldwide [8]. While lymphedema is difficult to cure once it develops, appropriate risk management is known to be an effective deterrent to its onset. Continuous treatment with regular follow-up surveillance is essential to avoid exacerbations, especially in the early stages, such as stage 0, which is described as a subclinical state without peripheral swelling, but with evidence of impaired lymphatic function, or stage I, which is described as reversible pitting edema without palpable fibrosis [9]. In recent years, an increasing number of reports have been published that early intervention provides a clinically evident improvement in many cases, thus preventing the progression to the chronic phase [10]–[13]. Despite the recognized importance of early diagnosis, lymphedema is frequently misdiagnosed, treated too late, or not treated at all [14]. The treatment might be delayed without a proper diagnosis, resulting in secondary fibrosis

and lipid deposition. Therefore, early diagnosis of lymphedema can benefit from quantitative and non-invasive methods to monitor “local” change of ECF in subcutaneous adipose tissue (SAT), which are especially specific to early symptoms.

1.2. Conventional Monitoring Methods and Problems

The conventional monitoring method for lymphedema diagnosis currently recommended by the International Society for Lymphology (ISL) is Technetium-99m lymphoscintigraphy [15]. A radioactive contrast agent is injected subcutaneously into the dorsum of the hands and feet, allowing the rough observation of lymphatic pathways and obstruction. While its advantage lies in its ability to visualize the state of the lymphatic system from the abdominal cavity to the thoracic duct and venous horn, its disadvantage lies in the difficulty of obtaining detailed images to monitor “local” change in the affected limb. Moreover, the test is not suitable for early diagnosis due to the high burden on the patient (radiation exposure, pain) as well as the limited number of facilities where lymphoscintigraphy is available.

Another conventional monitoring method for lymphedema diagnosis is indocyanine green fluorescent lymphography (ICG-LG), which is currently applied mainly in plastic surgery [16]. ICG is injected intradermally into the periphery of the affected limb, which majorly binds to albumin to be transported into the lymph vessels, allowing the observation of lymphatic pathways and obstruction in more detail than lymphoscintigraphy. While its advantage lies in its useful and low-cost assessment of lymphatic vessels in real-time, its disadvantage lies in the inability to monitor “local” change in the deep lymphatic system (>1.5 cm) as well as the limited number of repeated tests because injected ICG remains in the subcutaneous tissue for 2-3 weeks.

In order to monitor “local” change in morphological structure as a conventional monitoring method, ultrasound imaging (UI) is also widely used for observing the state of edema even if a definitive diagnosis is not possible [17]. However, UI still does not monitor components volume/concentration in ECF because UI focuses only on tissue morphological structure of the whole cross-sectional diseased tissue, e.g., SAT, which makes early diagnosis extremely difficult after all because it is not a “finding of lymphedema” but a general “finding of edema.” In this sense, other imaging modalities that focus on morphological structure, such as magnetic resonance imaging (MRI) and X-ray computed tomography (CT), still remain insufficient for early diagnosis [18].

As an alternative monitoring method, bioelectrical impedance analysis (BIA) is

commonly used as a non-invasive, harmless, and simple method for monitoring impedance arising from change in components volume but not concentration in ECF [19]. Numerous reports in recent years have supported its usefulness for early diagnosis, especially coupled with the patient surveillance model (PSM) [11], [13], [20], [21]. However, BIA is not able to monitor "local" change in components volume in ECF because the measurement target is too broad on the whole section of human limbs [22].

In the end, conventional monitoring methods are insufficient for the early diagnosis of lymphedema, as summarized in **Table 1.2**. Under these circumstances, electrical impedance tomography (EIT) is getting more desirable than the above conventional monitoring methods because EIT is able to monitor both "local spatiotemporal" change (LSTC) of components volume/concentration in ECF as well as easy operation, non-invasive, harmless, low cost, and capable of real-time monitoring [23].

Table 1.2. Conventional monitoring methods and problems.

Methods	Features	Problems
Lymphoscintigraphy	• Rough visualization of lymphatic pathways and obstruction from the abdominal cavity to the thoracic duct and venous horn	• Difficulty of obtaining detailed images to monitor "local" change • High burden on the patient (radiation exposure, pain) • Limited number of available facilities
Indocyanine green fluorescent lymphography (ICG-LG)	• Detailed visualization of lymphatic pathways and obstruction • Low-cost • Real-time	• Inability to monitor "local" change in the deep lymphatic system (>1.5 cm) • Limited number of repeated tests
Ultrasound imaging (UI)	• Observation of a general "finding of edema" • Low-cost, harmless, already widespread • Real-time	• Inability to observe a "finding of lymphedema" • Low inter-rater reliability
Bioelectrical impedance analysis (BIA)	• Monitoring impedance arising from change in components volume in ECF • Harmless, simple • Numerous reports for its usefulness for early diagnosis	• Inability to monitor "local" change in components volume • Inappropriate for bilateral lymphedema

1.3. Thesis Objective

In order to resolve the conventional methods' problems, the author has proposed EIT for monitoring "local" volume/concentration change in the extracellular fluid (ECF). In particular, the physiological edema, which can be examined in healthy subjects, has been deeply investigated as fundamental research towards the early diagnosis of lymphedema. The thesis objectives are systematically structured as follows:

1) Investigation of physiological edema on conductivity distribution **σ** in lower leg subcutaneous tissue. Firstly, this thesis provides the study of **σ** in lower leg subcutaneous tissue. The reconstructed results of **σ** show a good correlation with ECF volume measured by BIA, which suggests the possibility of monitoring volume/concentration change.

2) Investigation of the relationship between frequency-dependence and absolute conductivity value in the reconstructed image through the miniature EIT sensor as fundamental research towards developing data preprocessing. Secondly, this thesis explores frequency-difference electrical impedance tomography (*fd*-EIT) to understand why multiple objects are elucidated, even when the steps of conductivity increments are identical among the objects.

3) Development of multifrequency EIT (*mf*-EIT) with a ratiometric preprocessing for boosting robustness under high conductivity contrast of biological tissue and suppressing excessive noise. Thirdly, this thesis investigates imaging of calf compartments by minimizing the conductivity contrast μ that is inherently high in the human body. Based on the reconstructed results, the proposed ratiometric EIT could minimize μ while maintaining high distinguishability in the heterogeneous background without any *a priori* information.

4) Monitoring of local-spatiotemporal change (LSTC) in the extracellular fluid (ECF) by time-variation-constraint sparse Bayesian learning (*tvc*SBL) implemented into frequency-difference EIT (*fd*-EIT). Fourthly, this thesis explains the possibility of monitoring the LSTC in ECF by the proposed *tvc*SBL-*fd*EIT, which consists of three steps; Step 1: formulation of blocked column vector (BCV), Step 2: SAT separation by time variation constraint, and Step 3: temporal correlation extraction by hyperparameter learning.

Finally, the proposed EIT offers an innovative reconstruction technique for monitoring "local" volume/concentration change in ECF with the aid of ratiometric preprocessing and Sparse Bayesian Learning (SBL), which are particularly focused on physiological edema.

References

[1] D. O. Bates, J. R. Levick, and P. S. Mortimer, "Starling pressures in the human arm and their alteration in postmastectomy oedema.," *J. Physiol.*, vol. 477, no. 2, pp. 355–363, 1994, doi: 10.1113/jphysiol.1994.sp020197.

[2] S. H. Ridner, "Breast cancer lymphedema: pathophysiology and risk reduction guidelines.," *Oncol. Nurs. Forum*, vol. 29, no. 9, pp. 1285–93, 2002, doi: 10.1188/02.ONF.1285-1293.

[3] P. S. Mortimer and J. R. Levick, "Chronic peripheral oedema: The critical role of the lymphatic system," *Clinical Medicine, Journal of the Royal College of Physicians of London*, vol. 4, no. 5. pp. 448–453, 2004.

[4] P. Marcks, “Lymphedema. Pathogenesis, prevention, and treatment,” *Cancer Pract.*, vol. 5, no. 1, pp. 32–38, 1997.

[5] W. L. Olszewski, “Pathophysiological aspects of lymphedema of human limbs: I. Lymph protein composition,” *Lymphat Res Biol*, vol. 1, no. 3, pp. 235–243, 2003, doi: 10.1089/153968503768330265.

[6] N. Liu, “Metabolism of macromolecules in tissue.,” *Lymphat. Res. Biol.*, vol. 1, no. 1, pp. 67–70, 2003, doi: 10.1089/15396850360495718.

[7] I. S. of L. E. Committee, “The diagnosis and treatment of peripheral lymphedema. Consensus document of the International Society of Lymphology Executive Committee.,” *Lymphology*, vol. 42, pp. 51–60, 2009.

[8] N. Matsui, H. Sanada, and A. Hirota, “Lymphoedema in Japan : current issues,” *Intern. Med.*, vol. 3, no. 2, pp. 36–37, 2008.

[9] E. Committee, “The diagnosis and treatment of peripheral lymphedema: 2016 consensus document of the international society of lymphology,” *Lymphology*, vol. 49, no. 4, pp. 170–184, Mar. 2016.

[10] J. a Petrek, P. I. Pressman, and R. a Smith, “Lymphedema: current issues in research and management.,” *CA. Cancer J. Clin.*, vol. 50, no. 5, pp. 292–307; quiz 308–311.

[11] S. A. McLaughlin, N. L. Stout, and M. V. Schaverien, “Avoiding the Swell: Advances in Lymphedema Prevention, Detection, and Management,” *Am. Soc. Clin. Oncol. Educ. B.*, no. 40, pp. e17–e26, 2020, doi: 10.1200/edbk_280471.

[12] S. H. Ridner *et al.*, “A prospective study of L-Dex values in breast cancer patients pretreatment and through 12 months postoperatively,” *Lymphat. Res. Biol.*, vol. 16, no. 5, pp. 435–441, 2018, doi: 10.1089/lrb.2017.0070.

[13] C. Shah, D. W. Arthur, D. Wazer, A. Khan, S. Ridner, and F. Vicini, “The impact of early detection and intervention of breast cancer-related lymphedema: a systematic review,” *Cancer Med.*, vol. 5, no. 6, pp. 1154–1162, 2016, doi: 10.1002/cam4.691.

[14] J. Todd, A. Scally, D. Dodwell, K. Horgan, and A. Topping, “A randomised controlled trial of two programmes of shoulder exercise following axillary node dissection for invasive breast cancer,” *Physiotherapy*, vol. 94, no. 4, pp. 265–273, 2008, doi: 10.1016/j.physio.2008.09.005.

[15] J. Maegawa, T. Mikami, Y. Yamamoto, T. Satake, and S. Kobayashi, “Types of lymphoscintigraphy and indications for lymphaticovenous anastomosis,” *Microsurgery*, vol. 30, no. 6, pp. 437–442, 2010, doi: 10.1002/micr.

[16] S. Akita *et al.*, “A phase III, multicenter, single-arm study to assess the utility of indocyanine green fluorescent lymphography in the treatment of secondary lymphedema,” *J. Vasc. Surg. Venous Lymphat. Disord.*, vol. 10, no. 3, pp. 728-737.e3, 2022, doi: 10.1016/j.jvsv.2021.09.006.

[17] K. Suehiro, N. Morikage, K. Ueda, and M. Samura, “Local Echo-Free Space in a Limb with Lymphedema Represents Extracellular Fluid in the Entire Limb,” vol. 00, no. 00, pp. 1–6, 2017, doi: 10.1089/lrb.2017.0053.

[18] M. Pappalardo, M. Starnoni, G. Franceschini, A. Baccarani, and G. De Santis, “Breast cancer-related lymphedema: Recent updates on diagnosis, severity and available treatments,” *J. Pers. Med*, p. 402, 2021, [Online]. Available: https://doi.org/10.3390/jpm.

[19] S. F. Khalil, M. S. Mohktar, and F. Ibrahim, “The theory and fundamentals of bioimpedance analysis in clinical status monitoring and diagnosis of diseases,” *Sensors (Switzerland)*, vol. 14, no. 6, pp. 10895–10928, 2014, doi: 10.3390/s140610895.

[20] S. H. Ridner *et al.*, “A Comparison of Bioimpedance Spectroscopy or Tape Measure Triggered Compression Intervention in Chronic Breast Cancer Lymphedema Prevention,” *Lymphat. Res. Biol.*, vol. 00, no. 00, 2022, doi: 10.1089/lrb.2021.0084.

[21] M. Asklöf, P. Kjølhede, N. B. Wodlin, and L. Nilsson, “Bioelectrical impedance analysis; a new method to evaluate lymphoedema, fluid status, and tissue damage after gynaecological surgery - A systematic review,” *Eur. J. Obstet. Gynecol. Reprod. Biol.*, vol. 228, pp. 111–119, 2018, doi: 10.1016/j.ejogrb.2018.06.024.

[22] M. Y. Jaffrin and H. Morel, “Body fluid volumes measurements by impedance: A review of bioimpedance spectroscopy (BIS) and bioimpedance analysis (BIA) methods,” *Med. Eng. Phys.*, vol. 30, no. 10, pp. 1257–1269, 2008, doi: 10.1016/j.medengphy.2008.06.009.

[23] J. Yao and M. Takei, “Application of Process Tomography to Multiphase Flow Measurement in Industrial and Biomedical Fields: A Review,” *IEEE Sens. J.*, vol. 17, no. 24, pp. 8196–8205, 2017, doi: 10.1109/JSEN.2017.2682929.

Chapter 2 Electrical Impedance Tomography

2. Electrical Impedance Tomography (EIT)

2.1. EIT Overview

Electrical impedance tomography (EIT) is a non-invasive, non-ionizing, fast-response, easy operation, and inexpensive monitoring technique that visualizes the internal conductivity distribution **σ** based on the boundary voltage **V** [1]. EIT was developed around three decades ago as a functional monitoring to analyze the pathology and physiology of the human body, including limbs [2], breasts [3], lung [4], and brain [5]. Similar to bioimpedance analysis (BIS), EIT employs impedance measurement using a four-electrode method. The difference is that EIT performs multi-projection measurements using four or more electrodes to reconstruct an image of the object. **Figure 2.1** shows the schematic of the EIT system configuration where the domain (e.g., bone, muscle, fat) is excited electrically by the electrical currents *I* injected through the electrodes, which are discretely placed along the domain boundary (e.g., skin). EIT focuses on the electrical impedance characteristics of organs and tissues, which diversify according to physiological and pathological conditions [6], which utilizes various excitation patterns to apply safe driving current/voltage to the human body, measures the response information through the safe excitation of biological tissues, and reconstructs **σ** inside the human body [7]. The current excitation is applied into the measurement section through a pair of electrodes and excites the sensing field. The changes of impedance **Z** in the measurement domain **Ω** are detected by the sensing field resulting in the change of the electrical potential distribution $\boldsymbol{\varphi}$. Similarly, the boundary voltage of the sensing field changes accordingly. The measured voltage therefore contains information about the impedance in the sensing field.

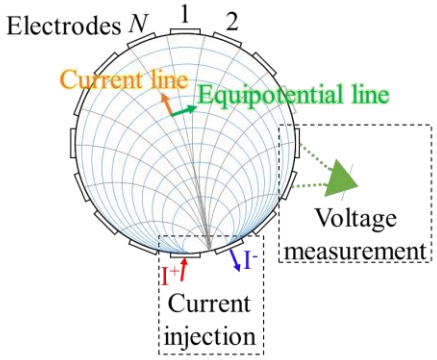

Figure 2.1 Schematic diagram of EIT system configuration.

In **Figure 2.1**, when a periodic constant current is applied to the domain Ω at a angular frequency ω from the boundary surface $\partial\Omega$, the electric and magnetic fields at $\partial\Omega$ also vary periodically at the same ω, which are expressed as $Ee^{j\omega t}$ and $He^{j\omega t}$, respectively. In this case, Ampere's law and Faraday's law are as follows [8]

$$\nabla \times H - j\omega D = i \tag{2.1}$$

$$\nabla \times E + j\omega B = 0 \tag{2.2}$$

where i is the current density, D is the electric flux density, and B is the magnetic flux density. Given the isotropic materials, the following relationship between D, B, E, and H is as follows

$$D = \varepsilon_r \varepsilon_0 E \tag{2.3}$$

$$B = \mu_r \mu_0 H \tag{2.4}$$

where ε_r, ε_0, μ_r, and μ_0 are the relative permittivity, the vacuum permittivity, the relative permeability, and the vacuum permeability, respectively. Moreover, a differential form of Ohm's law is expressed as follows

$$i = \sigma E \tag{2.5}$$

The following equations are obtained by substituting Equations (2.3) and (2.4) into Equations (2.1) and (2.2)

$$\nabla \times H = (\sigma + j\omega \varepsilon_r \varepsilon_0) E \tag{2.6}$$

$$\nabla \times E = -j\omega \mu_r \mu_0 H \tag{2.7}$$

Using the following relationship between the electric field E and the potential φ,

$$E = -\nabla \varphi \tag{2.8}$$

Equation (2.6) can be written as follows

$$\nabla \times H = -\left(\sigma + j\omega \varepsilon_r \varepsilon_0\right) \nabla \varphi \tag{2.9}$$

By multiplying both sides by $\nabla \cdot$, the left-hand side of Equation (2.9) can be written as follows

$$\nabla \cdot \nabla \times H = 0 \tag{2.10}$$

Considering the real part, the following Laplace equation is obtained in the absence of interior current sources

$$\nabla \cdot (\sigma \nabla \varphi) = 0 \tag{2.11}$$

This is the governing equation between the conductivity σ and the potential φ in Ω. Moreover, the Neumann boundary condition on the excited electrode is written by

$$i = \sigma \nabla u \cdot \mathbf{n}_{\partial\Omega} \tag{2.12}$$

where $\mathbf{n}_{\partial\Omega}$ is the outward unit normal vector. In EIT, Ω is discretized into N elements to yield the conductivity distribution $\boldsymbol{\sigma} = [\sigma_1,\ldots, \sigma_n,\ldots, \sigma_N]\in\mathbb{R}^N$. Subsequently, the boundary voltage $\mathbf{V}$ is $\mathbf{V} = [v_1,\ldots, v_m,\ldots, v_M]\in\mathbb{R}^M$, where M is the total number of measurement pairs. Since EIT is an optimization-based method, the derivative of the voltage measurements with respect to a conductivity parameter often needs to be calculated. In other words, the sensitivity matrix $\mathbf{J}\in\mathbb{R}^{M\times N}$ is required

$$\mathbf{J} = \begin{pmatrix} \frac{\partial v_1}{\partial \sigma_1} & \cdots & \frac{\partial v_1}{\partial \sigma_N} \\ \vdots & \ddots & \vdots \\ \frac{\partial v_M}{\partial \sigma_1} & \cdots & \frac{\partial v_M}{\partial \sigma_N} \end{pmatrix} \tag{2.13}$$

with which the element J_{mn} of m-th measured voltage pattern at n-th mesh element is obtained by [9]

$$J_{mn} = \frac{\partial v_m}{\partial \sigma_n} = \int_{\Omega} \nabla u\left(i^e\right).\nabla u\left(i^m\right)\mathrm{d}\Omega \tag{2.14}$$

where $u(i^e)$ is the potential field produced by injecting current i into the e-th electrode, $u(i^m)$ is the potential field produced by injecting current i into the m-th measured voltage pattern, v_m is the measured voltage at the m-th measured electrode pattern ($1\leq m\leq M$). Finally, the following governing equation is obtained

$$\mathbf{V} = \mathbf{J}\boldsymbol{\sigma} \tag{2.15}$$

Unfortunately, $\mathbf{J}$ is known not to have an inverse matrix; thus no unique solution. Furthermore, since $M < N$, EIT is an ill-posed inverse problem; therefore, an approximate solution must be sought by a suitable algorithm. Since the least-squares approach mostly fails in the ill-posed inverse problem, the approximate solution is sought by regularizing the optimization problem

$$\boldsymbol{\sigma} = \arg\min_{\boldsymbol{\sigma}}\left(\left\|\mathbf{J}\boldsymbol{\sigma} - \mathbf{V}\right\|^2 + \lambda\left\|\boldsymbol{\sigma}\right\|^2\right) \tag{2.16}$$

where $\mathbf{J}$ is usually calculated under the homogeneous condition $\boldsymbol{\sigma}_0$ [10] and λ is the regularization hyperparameter. The λ controls the trade-off between the exact and approximate solution. Equation (2.16) is conventionally solved by the Gauss-Newton algorithm because it is the most often used solver for the biomedical EIT due to its robustness to noise [11], which is computed with the Tikhonov regularization [12]

$$\boldsymbol{\sigma}^{it+1} = \boldsymbol{\sigma}^{it} + (\mathbf{J}^T\mathbf{J} + \lambda\mathbf{I})^{-1}[\mathbf{J}^T(\mathbf{V} - \mathbf{J}\boldsymbol{\sigma}^{it})] + \lambda\mathbf{I}(\boldsymbol{\sigma}_0 - \boldsymbol{\sigma}^{it}) \quad (2.17)$$

where $\boldsymbol{\sigma}^{it}$ is the conductivity image at the *it*-th iteration step. Even though the Gauss-Newton algorithm is helpful for relatively mildly noisy environments, the difficulties still lie in the real clinical world; therefore, other promising algorithms, such as Sparse Bayesian Learning (SBL), are investigated as well as efficient preprocessing called "ratiometric" in the following chapters.

2.2. Electrical Properties of Biological Tissues

The human body is mainly composed of hydrogen, oxygen, carbon, and nitrogen, which comprise 63 %, 25 %, 9 %, and 1.4 %, respectively, within the body [13]. These four main atoms within the human body form covalently bonded ions based on the electron pairing of two atoms, such as water. Human biological tissue is composed mainly of water. Therefore, human biological tissue is able to be classified as a conductive medium. **Figure 2.2(b)** and **(c)** shows the reference values for the conductivity and relative permittivity of biological tissues measured *in vitro* by the Italian Institute of Applied Physics [16]. These reference values are beneficial to understand the basic principle of biomedical visualization in EIT, for example, monitoring of physiological edema at low frequency by analyzing the extracellular fluid (ECF) [17].

In order to evaluate the physiological edema by EIT in healthy subjects, the electrical properties of the human calf are considered. **Figure 2.2** shows an example of human calf compartments and corresponding dielectric properties with a diversified spectrum over frequency. The calf compartments comprise seven compartments as shown in **Figure 2.2(a)**; skin (Ω^{sk}), SAT (Ω^{SAT}), muscle (Ω^{mu}), bone cortical (Ω^{bc}), bone marrow (Ω^{bm}). Each compartment has a various dielectric relationship with frequency, as shown in **Figure 2.2(b)** and **(c)** (adapted from [15]), which provides structural information about changes in physiological conditions via frequency-difference EIT (*fd*-EIT) [16]. The conductivity value σ_f on each compartment Ω parameterizes the raw impedance $z_{m,f}$ variously depending on Ω by the nonlinear transformation $\sigma_f \rightarrow z_{m,f}$ on the boundary $\partial\Omega$. In this study, σ_f in Ω^{sk}, Ω^{SAT}, Ω^{bc}, and Ω^{bm} are considered as anomalies $\sigma^a{}_f \approx \chi^a{}_f(\Omega^{sk}, \Omega^{SAT}, \Omega^{bc}, \Omega^{bm})$; in contrast, σ_f in Ω^{mu} is regarded as a background $\sigma^{bg}{}_f \approx \chi^{bg}{}_f(\Omega^{mu})$. Here $\chi^a{}_f$ and $\chi^{bg}{}_f$ denote the characteristic function

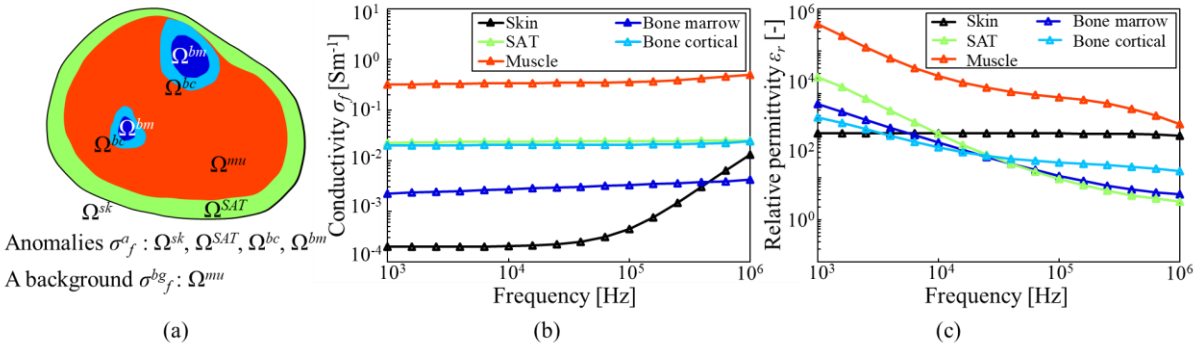

Figure 2.2 Example of segmented human calf compartment and change in electrical properties of human calf compartment over frequency. (a) Calf compartment. The superscripts represent the corresponding tissues. (b) electrical conductivity, (c) relative permittivity.

to specify σ_f in the FEM mesh of the anomalies and background, respectively. Under these circumstances, several hypotheses are come up with, especially beneficial for monitoring of physiological edema; for example, *fd*-EIT is theoretically able to monitor the spatiotemporal change of components volume/concentration in ECF because **σ** of NaCl solution as the main component in ECF is frequency-independent below frequency f = 1MHz [17], whereas **σ** of protein solution as the subcomponent in ECF is frequency-dependent [18]. According to this explanation, spatiotemporal change of components volume/concentration in ECF is considered a key target for monitoring physiological edema. In the case of lymphedema, the very-small change must be monitored, especially for early diagnosis; therefore, the investigation of the EIT algorithm with "high distinguishability" and ability to reconstruct "local-spatiotemporal change (LSTC)" is reasonable; in this thesis, the former is sought by "ratiometric preprocessing" whereas the latter is sought by "time-variation-constraint sparse Bayesian learning (*tvc*SBL)" implemented into *fd*-EIT.

References

[1] T. Dowrick, C. Blochet, and D. Holder, "In vivo bioimpedance changes during haemorrhagic and ischaemic stroke in rats: towards 3D stroke imaging using electrical impedance tomography," *Physiol. Meas.*, vol. 37, no. 6, p. 765, 2016.

[2] R. Ogawa, M. R. Baidillah, S. Akita, and M. Takei, "Investigation of physiological swelling on conductivity distribution in lower leg subcutaneous tissue by electrical impedance tomography," *J. Electr. Bioimpedance*, vol. 11, no. May, pp. 19–25, 2020.

[3] V. Cherepenin *et al.*, “A 3D electrical impedance tomography (EIT) system for breast cancer detection,” *Physiol. Meas.*, vol. 22, no. 1, p. 9, 2001.

[4] J. A. Victorino *et al.*, “Imbalances in regional lung ventilation: a validation study on electrical impedance tomography,” *Am. J. Respir. Crit. Care Med.*, vol. 169, no. 7, pp. 791–800, 2004.

[5] T. Tidswell, A. Gibson, R. H. Bayford, and D. S. Holder, “Three-dimensional electrical impedance tomography of human brain activity,” *Neuroimage*, vol. 13, no. 2, pp. 283–294, 2001.

[6] Y. Zou and Z. Guo, “A review of electrical impedance techniques for breast cancer detection,” *Med. Eng. Phys.*, vol. 25, no. 2, pp. 79–90, 2003.

[7] M. Cheney, D. Isaacson, and J. C. Newell, “Electrical Impedance Tomography,” *SIAM Rev.*, vol. 41, no. 1, pp. 85–101, 1999, doi: 10.2307/2653168.

[8] D. S. Holder, *Electrical impedance tomography: methods, history and applications*. Bristol, UK: IOP Publishing, 2005.

[9] P. N. Darma, M. R. Baidillah, M. W. Sifuna, and M. Takei, “Real-time dynamic imaging method for flexible boundary sensor in wearable electrical impedance tomography,” *IEEE Sens. J.*, vol. 20, no. 16, pp. 9469–9479, 2020, doi: 10.1109/JSEN.2020.2987534.

[10] C. Kotre, “A sensitivity coefficient method for the reconstruction of electrical impedance tomograms,” *Clin. Phys. Physiol. Meas.*, vol. 10, no. 3, pp. 275–281, 1989.

[11] B. Harrach and J. K. Seo, “Exact shape-reconstruction by one-step linearization in electrical impedance tomography,” *SIAM J. Math. Anal.*, vol. 42, no. 4, pp. 1505–1518, 2010, doi: 10.1137/090773970.

[12] M. Vauhkonen, D. Vadâsz, P. A. Karjalainen, E. Somersalo, and J. P. Kaipio, “Tikhonov regularization and prior information in electrical impedance tomography,” *IEEE Trans. Med. Imaging*, vol. 17, no. 2, pp. 285–293, 1998, doi: 10.1109/42.700740.

[13] M. A. Zoroddu, J. Aaseth, G. Crisponi, S. Medici, M. Peana, and V. M. Nurchi, “The essential metals for humans: a brief overview,” *J. Inorg. Biochem.*, vol. 195, pp. 120–129, 2019.

[14] C. Basile *et al.*, “Phase angle as bioelectrical marker to identify elderly patients at risk of sarcopenia,” *Exp. Gerontol.*, vol. 58, pp. 43–46, 2014.

[15] D. Andreuccetti, R. Fossi, and C. Petrucci, “An internet resource for the calculation of the dielectric properties of body tissues in the frequency range 10 Hz - 100 GHz,” *IFAC-CNR, Florence (Italy), Based data Publ. by C Gabriel al. 1996.*, 1997.

[16] H. Griffiths and A. Ahmed, “A dual-frequency applied potential tomography technique: computer simulations,” *Clin. Phys. Physiol. Meas.*, vol. 8, pp. 103–107, 1987.

[17] A. Peyman, C. Gabriel, and E. H. Grant, “Complex permittivity of sodium chloride solutions at microwave frequencies,” *Bioelectromagnetics*, vol. 28, no. 4, pp. 264–274, 2007, doi: 10.1002/bem.20271.

[18] M. W. Sifuna, M. R. Baidillah, D. Kawashima, P. N. Darma, E. O. Odari, and M. Takei, “Determination of sensitive frequency margin for aggregated protein concentration quantification by fd-electrical impedance tomography,” *Meas. J. Int. Meas. Confed.*, vol. 186, no. September, p. 110135, 2021, doi: 10.1016/j.measurement.2021.110135.

Chapter 3 Investigation of physiological swelling on conductivity distribution in lower leg subcutaneous tissue by EIT

3. Investigation of physiological swelling on conductivity distribution in lower leg subcutaneous tissue by EIT

3.1. Research Motivation

Variation of the physiological condition of subcutaneous adipose tissue (SAT) has been diagnosed as a part of metabolic syndrome (MetS) [1], lymphedema [2], Dercum's disease [3], and obesities [4]. Multi-Frequency Bioelectrical Impedance Analysis (MFBIA) or Bio-Electrical impedance spectroscopy (BIS) is proposed as a rapid tool for SAT assessment as it has demonstrated a significant impedance difference between healthy and abnormal SAT [2,4,5]. MFBIA uses 8 resistive electrodes attached to the ankle and wrist through multi-frequency impedance measurements on the whole body. Its portability and non-invasive characteristic make MFBIA more attractive for routine physiology measurement [6].

MFBIA is used based on the fact that the current flow through biological tissue is frequency-dependent [7]. At low frequencies, the membrane cell acts as a high impedance. It makes the current flows only at extracellular fluid. Meanwhile, at the increase of frequency, the impedance of the cell membrane is decreased and makes the current possible to penetrate into the intracellular fluid. Several Anthropometric parameters need to be considered to relate the measured impedance with the water content at interstitial fluid, such as body weight, body height, gender, age, and postures [8]. MFBIA assumes a human body as a single object to be measured in which only single volumes of particular compartments are measurable [9]. However, there are a number of potential limitations to MFBIA, such as an inability to assess heterogeneity of SAT and to differentiate edema type accurately and albumin accumulation location [9,10], and the performance depends on the accuracy of the controlled clinical condition [11]. These issues make a shortcoming and lead to the modification of MFBIA to localize body segment impedance evaluation [10,12].

Our objective is, therefore, to develop non-invasive and low-cost medical equipment using impedance measurement with several multi-projection, i.e., using Electrical Impedance Tomography (EIT). EIT is a non-invasive medical imaging method that can show the conductivity distribution of the human body [13–15]. In EIT, the domain (e.g., bone, muscle) is excited electrically by the electrical currents injected through the electrodes, which are discretely placed along the domain boundary (e.g., skin). The exciting electric field in the domain is determined in accordance with the geometry, the boundary conditions, and the

internal distribution of the electrical properties such as conductivity. The excited voltages on the electrodes can be measured and then used to reconstruct the internal conductivity distribution. As the human body has been demonstrated to have different electrical properties [16], a cross-sectional view can be reconstructed with EIT to identify any abnormalities; on the subject of the early detection of lymphedema, which is the protein accumulation in subcutaneous adipose tissue. The relative value is mostly used for the image reconstruction, i.e., homogeneous data is taken as a reference to image the difference owing to the abnormality. However, it is troublesome considering that homogeneous reference data cannot be taken in biomedical instrumentation as they always vary over different subjects, and the human body is composed of complex properties.

This paper aims to investigate the feasibility of EIT to assess interstitial fluid in SAT as a preliminary step in lymphedema early detection. We measure the right lower leg to examine to what extent our EIT system with the novel threshold technique has the quality to show the morphologically same image as a sample of the MRI image. A physiological swelling experiment is then carried out to scrutinize the relationship between MFBIA and our EIT system. In order to effectively focus on the varying water contents, image-based reference EIT is proposed.

3.2. Materials and Methods

3.2.1. Image-based reference Electrical Impedance Tomography (IBR-EIT)

The aim of EIT is to recover conductivity distribution $\boldsymbol{\sigma} \in \mathbb{R}^N$ inside the domain Ω from Neumann boundary voltage $\mathbf{V}$ where N is the number of mesh ($1 \leq n \leq N$). Considering the high ill-posedness of the inverse problem of EIT, the solution $\boldsymbol{\sigma}$ is estimated by minimizing the output least-squares concerning the actual measured voltage $\mathbf{V}^{meas}$ and the simulated voltage $\mathbf{V}=\mathbf{S}\boldsymbol{\sigma}$;

$$\boldsymbol{\sigma} = \arg\min_{\boldsymbol{\sigma}} \left[\left\| \mathbf{V}^{meas} - \mathbf{S}\boldsymbol{\sigma} \right\|^2 + \lambda \left\| \mathbf{R}\boldsymbol{\sigma} \right\|^2 \right] \tag{3.1}$$

where $\mathbf{S}$, λ, and $\mathbf{R}$ denote the sensitivity matrix, the regularization parameter, and a regularization matrix, respectively. In most cases, $\mathbf{R}$ is the diagonal matrix with the expected conductivity $\boldsymbol{\sigma}_0^2$, i.e., $\mathbf{R}_{m,m}=\boldsymbol{\sigma}_0^2$, and this penalty term relates to the prior information.

As the human body is very complex and has inhomogeneous electrical properties, there are problems not only to refer homogeneous reference conductivity but also with obtaining

the prior conductivity distribution. Thus, the problems can be compensated by considering the first measurement voltage data as the initial conductivity distribution and subtracting the conductivity distribution at a different time point relative to the initial conductivity. The initial conductivity distribution $\boldsymbol{\sigma}^{abs}$ are reconstructed using the absolute EIT method [18]. In order to observe the minuscule change of conductivity in subcutaneous tissue over the long-term standing (expressed in the subsection Experimental setup and condition), the subtraction can be performed based on the assumption that there is no distortion except for the influence from the change associated with the extracellular matrix in the subcutaneous layer. The general schematic flow of the proposed method or image-based reference EIT (IBR-EIT) with fat-weighted threshold method is as follows:

Table 1. Schematic flow of image-based reference EIT (IBR-EIT).

Step 1:
Defining filter method to eliminate the muscle's conductivity distribution and unexpected noise background
Obtain: Equation (3.2)
Step 2:
Using voltage data t = 0 as an initial conductivity distribution, selecting the mesh of SAT on the forward problem mesh condition, calculating the fat-weighted threshold value $<\boldsymbol{\sigma}^{fat}>+std(\boldsymbol{\sigma}^{fat})$
Obtain: Fat weighted threshold value $<\boldsymbol{\sigma}^{fat}>+std(\boldsymbol{\sigma}^{fat})$
Step 3:
Applying the filter on Equation (3.2) to experimental data
Obtain: $\boldsymbol{\sigma}^{abs}$ and $\boldsymbol{\sigma}$
Step 4:
Using voltage data t = 30, 60, and 90 mins to evaluate the varying water content to obtain the conductivity distribution, applying Equation (3.3)
Obtain: $\boldsymbol{\sigma}^{diff}$

Considering the fact that skin is a highly resistive material and the human body has a complex conductivity distribution, we first apply the nonlinear absolute Gauss-Newton imaging [19], where we set $\boldsymbol{\sigma}_0$ based on reference conductivity data [16] for each body part such that the muscle is the most conductive, which is followed by the fat and the bone in order. We choose the Laplace prior, in which the regularization matrix is interpreted as a 2nd order High Pass Filter (HPF) [20]. After obtaining the inhomogeneous reference, we implement the filtering process to all the data that weights the subcutaneous layer

$$\begin{cases} \sigma_n = \sigma_n, \text{ if } \sigma_n \le \left\langle \boldsymbol{\sigma}^{fat} \right\rangle + std(\boldsymbol{\sigma}^{fat}) \\ \sigma_n = \left\langle \sigma^{muscle} \right\rangle, \text{ if } \sigma_n > \left\langle \boldsymbol{\sigma}^{fat} \right\rangle + std(\boldsymbol{\sigma}^{fat}) \end{cases} \tag{3.2}$$

where σ_n is the n-th element of the estimated $\boldsymbol{\sigma}$ while $<\boldsymbol{\sigma}^{fat}>$ and $<\boldsymbol{\sigma}^{muscle}>$ are the spatial-mean of the estimated $\boldsymbol{\sigma}$ in the SAT layer and the muscle layer according to the FEM mesh (**Figure 3.1**), respectively. The operator $std(\cdot)$ returns the standard deviation. As for the elements lower than the threshold, those still entail the effect arising from fat and bone, considering the conductivity of bone is lower than that of fat. This FEM forward mesh is generated based on a sample of an MRI image using Netgen software (Netgen 4.9.13). Then the predicted absolute conductivity $\boldsymbol{\sigma}^{abs}$ is used as the image-based reference in the later image reconstruction as follows;

$$\boldsymbol{\sigma}^{diff} = \boldsymbol{\sigma} - \boldsymbol{\sigma}^{abs} \tag{3.3}$$

in which not only to reconstruct the absolute conductivity value but also to focus on the relative value. The $\boldsymbol{\sigma}^{diff}$ denotes the difference in conductivity distribution compared to the absolute $\boldsymbol{\sigma}^{abs}$. Based on the assumption regarding the muscle and bone area, the distortion in its area is also smoothened to reduce the background noise further. Here, importantly, the image error derived from the existence of the tibia, which does not accumulate liquid, could be mitigated when that influence acquired is constant across the experiments. The advantage of this method is to be able to focus on only the abnormalities, even if the background is inhomogeneous.

We implemented the quasi-adjacent stimulation and measurement pattern to accelerate the sensitivity near the boundary and the sensitivity map area [21] as the subcutaneous layer is located on the peripheral side of the domain, as depicted in **Figure 3.1**.

In order to compare the quality of the proposed method, a time-difference EIT was carried out [13], where the reference was taken from the simulation data

$$\boldsymbol{\sigma}^{tdEIT} = \boldsymbol{\sigma} - \boldsymbol{\sigma}^{\text{homo}} \tag{3.4}$$

where $\boldsymbol{\sigma}^{homo}$ represents the homogeneous conductivity distribution. In this simulation, we assume that the lower leg has three different values, i.e., the SAT layer, muscle, and bone. Those values were as identical to those used in FEM. Other settings such as the stimulation pattern, the magnitude of current, and the frequency, were the same as in the experiment.

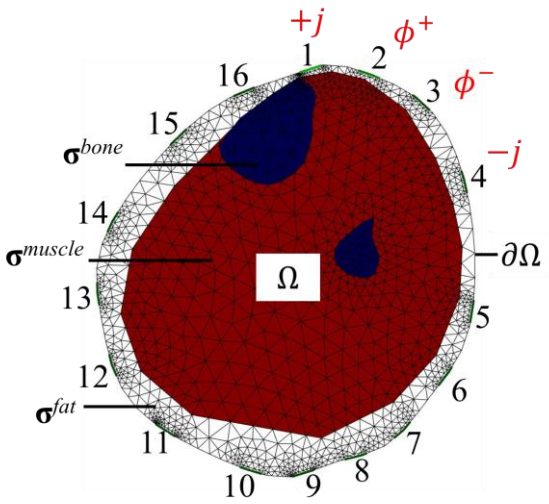

Figure 0.1 FEM forward mesh based on an MRI image. White, red, and blue part indicate SAT layer, muscle, and bone, respectively.

3.2.2. Wearable Sensor

As the human body is not a precise circle and the shape varies significantly among the subjects, the sensor configuration is often troublesome, especially for human subjects. Therefore, we developed a wearable EIT sensor, which has a row of 16 equidistant silver yarn electrodes and these electrodes are attached on a flexible cloth made of polyester. The electrodes are shielded by thermoplastic polyurethane (TPU) as a countermeasure for the high contact impedance [22]. It is worth mentioning that this sensor is excellent in adhesion to the skin so that contact impedance can be reduced. Furthermore, this sensor can adapt its size and shape to any subject with less discomfort.

3.2.3. Experimental setup and Conditions

Figure 3.2 shows an impedance analyzer (Impedance analyzer IM3570, HIOKI) and a multiplexer (multiplexer 34970A, Agilent) as the data acquisition system, which is connected to the wearable EIT sensor and a PC using coaxial cable and USB cable, respectively. The PC has installed LabVIEW (LabVIEW 2015, National Instruments) in order to visualize the spectrum and control the data acquisition system. The amplitude of the sinusoidal current is set as 1 mA, and 1 kHz frequency is selected to focus on the extracellular fluid as the low-frequency current penetrates only in the interstitium [23,24]). A multi-frequency impedance body composition analyzer (InBodyS10, InBody Japan Inc.) was used to measure

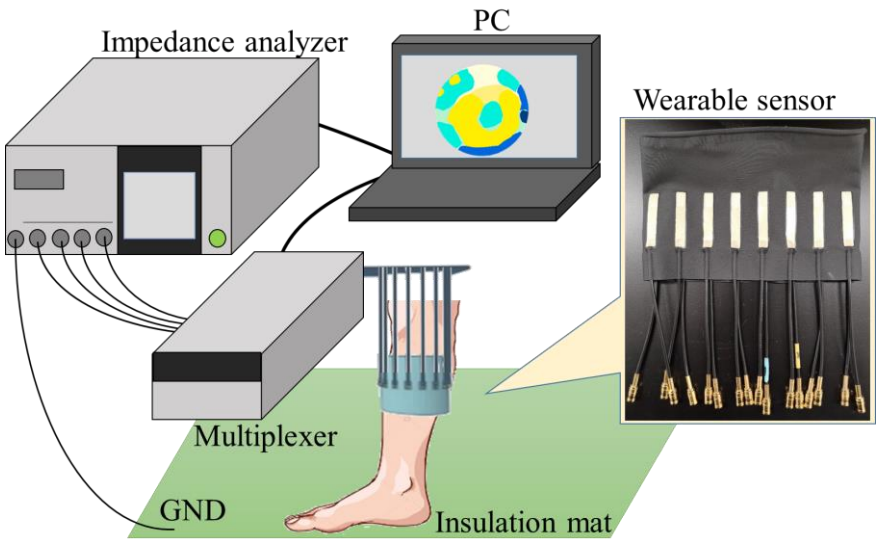

Figure 0.2 Experimental setup.

extracellular fluid volume in the right leg to acquire the varying water contents, which pertain specifically to the conductivity change.

Chester *et al.* reported a change in lower leg volume over time while standing [25]. Therefore, in our experiments, 3 healthy male subjects (Age = 22–33 years old, BMI = 23.2–26.0) stood for 75 minutes without any minor movement except when applying the measurement devices, followed by a 15-minute exercise to enhance the effect of the hydrostatic pressure of the vein as shown in **Figure 3.3**. EIT measurements and MFBIA were taken consecutively after every 30 minutes.

These experiments were carried out repeatedly for 5 days to attain the reliability of the experimental data. As MFBIA data is prone to be influenced by physiological information, the subject was strictly controlled regarding life activity such as wake-up time and breakfast menu throughout the experiment days.

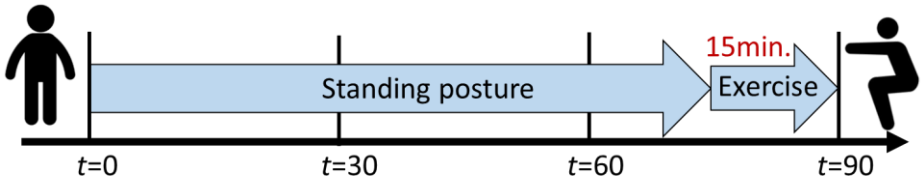

Figure 0.3 Schematic diagram of the experimental schedule. After the 3rd measurement (*t* = 75 min), the subject did exercise to promote varying water contents compared to the original physiological state at the beginning of the experiment.

3.3. Experimental Results

3.3.1. Reconstructed conductivity distribution

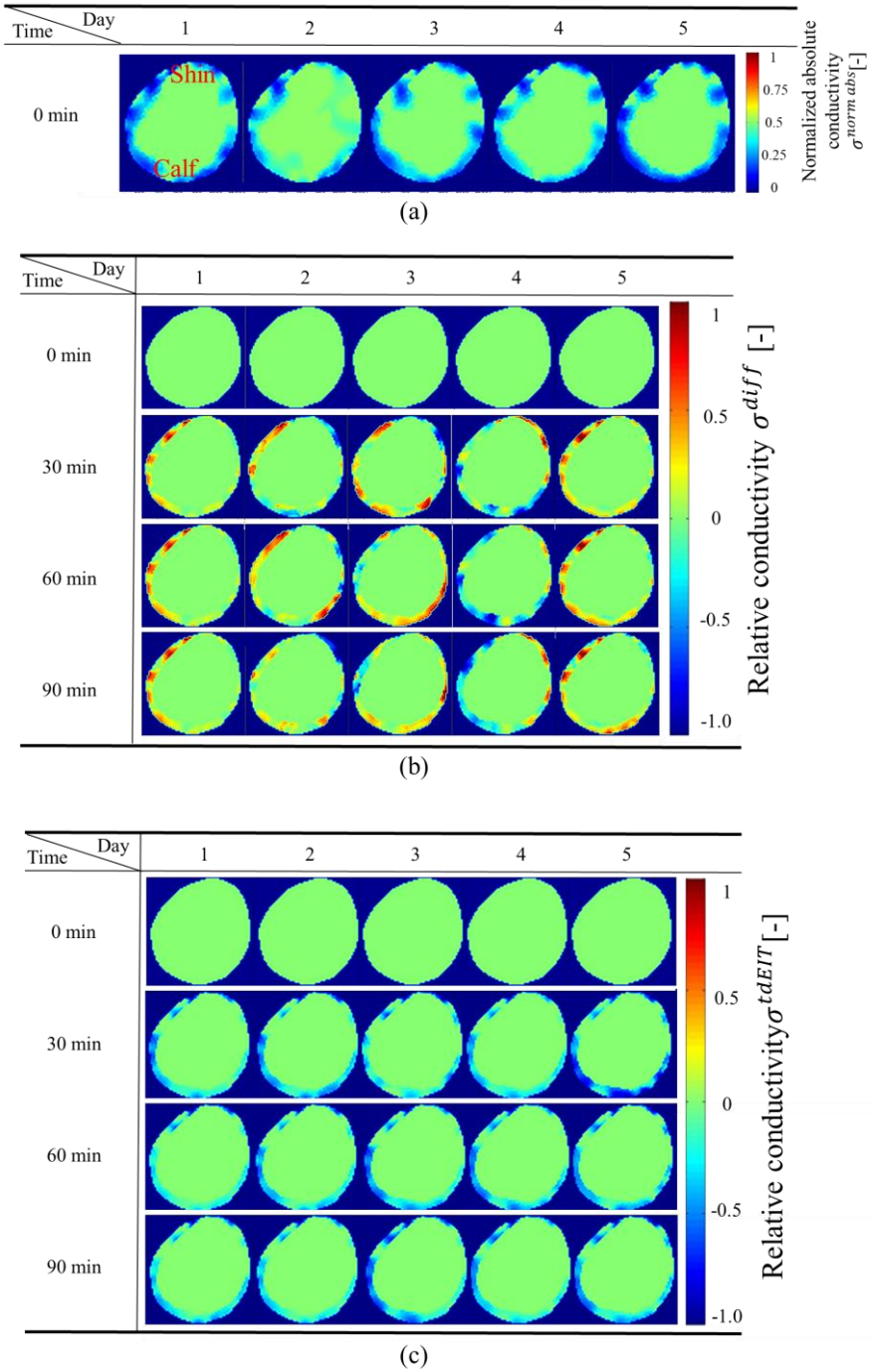

Figure 0.4 (a) Normalized absolute conductivity distribution of the right lower leg (viewed from the top) reconstructed by absolute EIT at 1st measurement; These are used as inhomogeneous reference data in (b). Time series of reconstructed relative conductivity distribution using the image-based reference EIT (b) and conventional time difference EIT (c) at 2nd, 3rd, and 4th measurement, respectively.

Figure 3.4(a) shows the normalized conductivity distribution reconstructed by absolute EIT on each day of one individual at the first measurement, which demonstrably shows the expected results. **Figure 3.4(b)** and **(c)** shows the time series of the reconstructed difference conductivity distribution on each day at t = 30 mins, 60 mins, and 90 mins with the proposed method and the conventional time difference EIT, respectively. **Figure 3.4 (a)** reveals the predicted subcutaneous layer based on the proposed fat-weighted threshold method. It has a satisfactory quality about the morphological relationship with an MRI image. The reconstructed SAT layer can be identified well throughout the experiment days. Although some noise can still be observed in **Figure 3.4 (b)**, in which the proposed method was used, conductivity at the SAT layer is increased as time passes, which indicates water increase in the layer. On the other hand, there is almost no change in **Figure 3.4 (c)**, in which the conventional time difference EIT was used; therefore, time variation cannot be observed. No change can be seen in the muscle and bone area in both methods, and the impedance artifacts in the periphery arise from the influence of the measurement and the modeling errors. Similar results were acquired over the course of experiment days.

3.3.2. Temporal variation of normalized spatial-mean conductivity

Figure 3.5 shows the temporal variation of normalized spatial-mean conductivity in the predicted SAT layer (white part in **Figure 3.1**) and segmental extracellular water volume in the right leg from EIT and MFBIA data, where the average of 5 days was taken at each time point. The effect of long-term standing and exercise can be seen clearly. The correlation

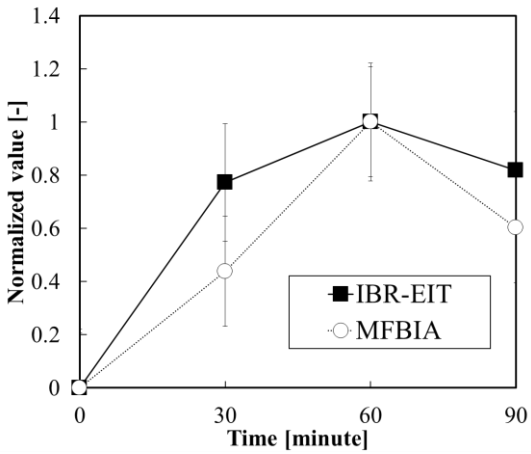

Figure 0.5 The normalized temporal variation of normalized spatial-mean conductivity in the predicted SAT layer (white part in Fig.1) and segmental extracellular water volume in the right leg from image-based reference EIT (IBR-EIT) and MFBIA data, respectively.

coefficient of EIT and MFBIA is achieved to R^2=0.927.

3.4. Discussion

3.4.1. Image interpretations

Ab solute EIT successfully reconstructed the images of the SAT layer; therefore, the fat-weighted threshold has a good potential to assess the interstitial fluid in the subcutaneous adipose tissue. Even though there is much background noise in the center of the images before the threshold process, this proposed method was able to reduce it sufficiently. On the other hand, as the thresholding result is calculated based on the average and the standard deviation, it may be affected when the signal-to-noise ratio (SNR) of the measurement voltage becomes lower [26]. Moreover, this thresholding can be performed based on the element selection of the FEM mesh; hence, it highly depends on the modelling.

We realize that the MRI data used in **Figure 3.1** is not always available for routinely monitoring using EIT. We used one MRI data as a piece of prior known information in order to consider the inaccuracy of the reconstruction algorithm and the boundary geometry effect on the reconstructed image. Considering this known information, we can obtain the average and standard deviation of SAT $<\boldsymbol{\sigma}^{fat}>+std(\boldsymbol{\sigma}^{fat})$, muscle, and bone through a mesh number obtained from MRI. The average of the predicted conductivity of the SAT $<\boldsymbol{\sigma}^{fat}>+std(\boldsymbol{\sigma}^{fat})$, which is a fat-weighted threshold value, is used to filter the conductivity distribution of experimental data as shown in Equation (3.4). Because the SAT position is always near the skin edge, obtaining the average and standard deviation of SAT $<\boldsymbol{\sigma}^{fat}>+std(\boldsymbol{\sigma}^{fat})$ can use a sample from some portion of mesh near the wall and has lower conductivity as compared with muscle region. The most reliable approach, in order to obtain a sample from some portion of the mesh, which is close to the boundary and has low conductivity, is to define the mesh condition for the forward problem, as shown in **Figure 3.1**. In this mesh condition, the tibia is disregarded because its image error tends to be constant during the different time points; thus, it can be neglected considering the fluid analysis. The mesh of the SAT could be changed into a very thin layer in order to accommodate a very thin subject.

In this chapter, image-based reference EIT (IBR-EIT) was applied to see the variation over reconstructed conductivity distribution, where the reference was obtained using the absolute EIT at the 1st measurement to focus on the relative value as time goes by. Even

though the images changed and the conductivity increased in most cases, stability is still a problem.

One of the reasons is the mathematical error in Equation (3.6). It is not enough just to subtract the value and should be compensated by introducing the penalty term or the weighted function [27]. The other reason for the lack of stability is measurement error. The subject wore the wearable sensor in the same position throughout the experiment days. It is known that even tiny changes, such as moisture on the skin, significantly change the conductivity. Thus, these problems should be calibrated mathematically and empirically.

Conventional time difference EIT was also implemented to compare the results, where the reference was taken from the simulation data. One of the reasons why the conductivity change was too small to see the difference in the conventional time difference EIT arises from a huge span of the impedance magnitudes. The ideal case was considered in the simulation, where the electrodes were properly attached to the skin, and the currents flowed through only on the two-dimensional surface. In addition, the contact impedance was set to a relatively small value. In the practical case, these conditions should be considered well, e.g., the electric currents are not generally confined to a two-dimensional plane [28], and the contact impedance is relatively large, especially in medical applications [29]. This same mistake about the current goes for the difference in the impedance magnitude of EIT and MFBIA. The former has an impedance different by four orders of magnitude from the latter. However, it does not necessarily mean those two data sets cannot be compared as the change of the extracellular matrix due to the physiological swelling generally affects the lower leg.

3.4.2. Impedance variation over time

Although EIT data and MFBIA data had a good correlation in **Figure 3.5**, EIT images failed to sufficiently elucidate the difference over time. Concerning high resistivity in the human body, especially the skin, the injected current might penetrate an undesirable pathway. **Figure 3.6** shows the magnitude variation of impedance at 0 min and 60 min on Day 1. Impedance decreased due to the rise in the extracellular water volume. In the quasi-adjacent stimulation, the magnitude should be the biggest at the $7+12\times(l-1)$ th [16], when the current is injected into the sensor through electrode pair 1-2 while the boundary voltage was measured at electrode pair 9-10 in the first round. Nevertheless, measured impedance data mostly experience the periodic peak at the $12\times l$ th (l=1~16) measurement pattern. Considering the morphological information, this is ascribed to the presence of the tibia, which

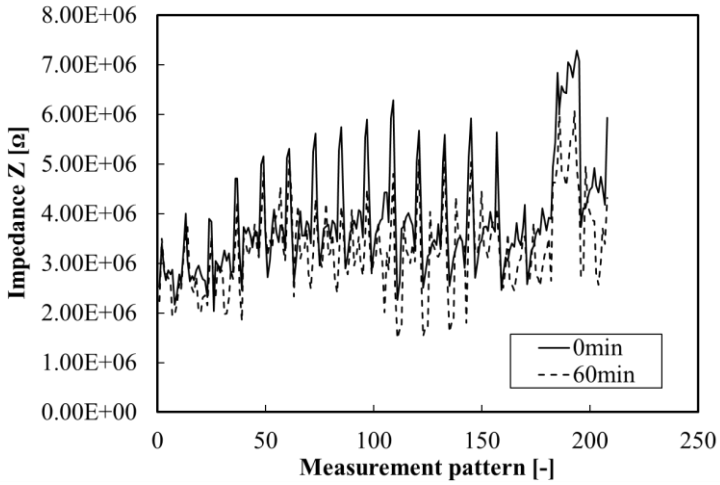

Figure 0.6 The magnitude of impedance at 0 min and 60 min on Day 1.

is located near the skin. As bone is a high-resistive material as well as fat, it might affect the current pathway, i.e., the accuracy of measurement data might be low when the stimulating electrodes are close to the tibia.

3.5.Summary

In this chapter, we investigated the feasibility of our EIT system to obtain a reconstructed image, which has a good correlation with an MRI image and the MFBIA data. We carried out a physiological experiment using a wearable 16 electrodes sensor and acquired the image using fat weighted threshold and image-based reference EIT (IBR-EIT). The absolute EIT images with the proposed threshold technique were able to visualize the subcutaneous adipose tissue (SAT) layer, which is morphologically similar to an MRI image of the right lower leg. Besides, the time series of EIT images have a high agreement with the MFBIA data regarding varying water content of the subcutaneous fat tissues in the lower leg due to the effect of the physiological swelling over five experiment days; these achieved a correlation coefficient R^2=0.927 to the MFBIA data. Although there were some errors in the images, the image-based reference EIT can focus on the distortion in the domain; furthermore, it effectively removed the unexpected background noise. It is concluded that the proposed method will be a great help to improve the treatment of lymphedema to preclude its chronic phase by applying EIT after breast cancer surgery.

References

[1] Tu AW, Humphries KH, Lear SA. Longitudinal changes in visceral and subcutaneous adipose tissue and metabolic syndrome: Results from the Multicultural Community Health Assessment Trial (M-CHAT). Diabetes Metab Syndr Clin Res Rev. Elsevier Ltd; 2017;11:S957–61.

[2] Rockson S. Bioimpedance analysis in the assessment of lymphoedema diagnosis and management. J Lymphoedema. 2007;2:44–8.

[3] Yacoob Aldosky HY, Yildiz A, Hussein HA. Regional body fat distribution assessment by bioelectrical impedance analysis and its correlation with anthropometric indices. Phys Med. Elsevier B.V.; 2018;5:15–9.

[4] Lee DH, Park KS, Ahn S, Ku EJ, Jung KY, Kim YJ, et al. Comparison of abdominal visceral adipose tissue area measured by computed tomography with that estimated by bioelectrical impedance analysis method in Korean subjects. Nutrients. MDPI AG; 2015;7:10513–24.

[5] Lukaski HC. Evolution of bioimpedance: A circuitous journey from estimation of physiological function to assessment of body composition and a return to clinical research. Eur J Clin Nutr. Nature Publishing Group; 2013;67:S2–9.

[6] Ackmann JJ, Seitz M a. Methods of complex impedance measurements in biologic tissue. Crit Rev Biomed Eng. 1984;11:281–311.

[7] Khalil SF, Mohktar MS, Ibrahim F. The theory and fundamentals of bioimpedance analysis in clinical status monitoring and diagnosis of diseases. Sensors (Basel) [Internet]. Multidisciplinary Digital Publishing Institute (MDPI); 2014;14:10895–928.

[8] Unno N, Nishiyama M, Suzuki M, Yamamoto N, Inuzuka K, Sagara D, et al. Quantitative Lymph Imaging for Assessment of Lymph Function using Indocyanine Green Fluorescence Lymphography. Eur J Vasc Endovasc Surg. 2008;36:230–6.

[9] Cornier MA, Després JP, Davis N, Grossniklaus DA, Klein S, Lamarche B, et al. Assessing adiposity: A scientific statement from the american heart association. Circulation. 2011;124:1996–2019.

[10] Rutkove SB, Aaron R, Shiffman CA. Localized bioimpedance analysis in the evaluation of neuromuscular disease. Muscle and Nerve. 2002;25:390–7.

[11] Dehghan M, Merchant AT. Is bioelectrical impedance accurate for use in large epidemiological studies? Nutr J [Internet]. 2008; 7:26.

[12] Scharfetter H, Monif M, László Z, Lambauer T, Hutten H, Hinghofer-Szalkay H. Effect of postural changes on the reliability of volume estimations from bioimpedance spectroscopy data. Kidney Int [Internet]. 1997;51:1078–87.

[13] Holder DS. Electrical Impedance Tomography: Methods, History and Applications. CRC Press. 2004;456.

[14] Adler A, Lionheart WRB. Uses and abuses of EIDORS: an extensible software base for EIT. Physiol Meas [Internet]. IOP Publishing; 2006; 27:S25–42.

[15] Yao J, Takei M. Application of Process Tomography to Multiphase Flow Measurement in Industrial and Biomedical Fields: A Review. IEEE Sens J [Internet]. 2017;17:8196–

205.

[16] Andreuccetti D, Fossi R, Petrucci C. An Internet resource for the calculation of the dielectric properties of body tissues in the frequency range 10 Hz - 100 GHz [Internet]. IFAC-CNR. 2017.

[17] Holder DS. Electrical Impedance Tomography: Methods, History and Applications. Holder DS, editor. CRC Press. Bristol, UK: IOP Publishing; 2005.

[18] Brown BH. Electrical impedance tomography (EIT): a review. J Med Eng Technol. 2009;27:97–108.

[19] Islam MR, Kiber MA. Electrical Impedance Tomography imaging using Gauss-Newton algorithm. 2014 Int Conf Informatics, Electron Vision, ICIEV 2014. IEEE Computer Society; 2014.

[20] Sarode V, Patkar S, N Cheeran A. Comparison of 2-D Algorithms in ElT based Image Reconstruction. Int J Comput Appl. Foundation of Computer Science; 2013;69:6–11.

[21] Baidillah MR, Iman A-AS, Sun Y, Takei M. Electrical Impedance Spectro-Tomography Based on Dielectric Relaxation Model. IEEE Sens J. 2017;17:8251–8262.

[22] Jin L, Kim KJ, Song EH, Ahn YJ, Jeong YJ, Oh TI, et al. Highly precise nanofiber web-based dry electrodes for vital signal monitoring. RSC Adv. Royal Society of Chemistry; 2016;6:40045–57.

[23] Ward LC, Bunce IH, Cornish BH, Mirolo BR, Thomas BJ, Jones LC. Multi-frequency bioelectrical impedance augments the diagnosis and management of lymphoedema in post-mastectomy patients. Eur J Clin Invest. 1992;22:751–4.

[24] Cornish BH, Bunce IH, Ward LC, Jones LC, Thomas BJ. Bioelectrical impedance for monitoring the efficacy of lymphoedema treatment programmes. Breast Cancer Res Treat. 1996;38:169–76.

[25] Chester MR, Rys MJ, Konz SA. Leg swelling, comfort and fatigue when sitting, standing, and sit/standing. Int J Ind Ergon. 2002;29:289–96.

[26] Yang Y, Jia J. An image reconstruction algorithm for electrical impedance tomography using adaptive group sparsity constraint. IEEE Trans Instrum Meas. Institute of Electrical and Electronics Engineers Inc.; 2017;66:2295–305.

[27] Jun SC, Kuen J, Lee J, Woo EJ, Holder DS, Seo JK. Frequency-difference EIT (fdEIT) using weighted difference and equivalent homogeneous admittivity: validation by simulation and tank experiment. Physiol Meas. 2009;30:1087–99.

[28] Rabbani KS, H.Kabir AMB. Studies on the effect of the third dimension on a two-dimensional electrical impedance tomography system. Clin Phys Physiol Meas. 1991;12:393–402.

[29] Rosell J, Colominas J, Riu P, Pallas-Areny R, Webster JG. Skin Impedance From 1 Hz to 1 MHz. IEEE Trans Biomed Eng. 1988;35:649–52.

Chapter 4 Investigation of the relationship between frequency-dependence and absolute conductivity value in the reconstructed image through the miniature EIT sensor

4. Investigation of the relationship between frequency-dependence and absolute conductivity value in the reconstructed image through the miniature EIT sensor

4.1. Research Motivation

Three-dimensional (3D) cell viability assays are increasingly needed to face the demand generated by the transition from traditional two-dimensional (2D) cell culture towards 3D cell culture systems that better mimic the behavior of cells growing in the natural environment [1], [2]. Polymeric biomaterial scaffolds are commonly used for 3D cell culture to provide structural support for cell adhesion and subsequent tissue development. In recent years, several 3D cell culture methods have been developed, such as scaffolds and hydrogels [3], [4]. These methods aim to achieve a more physiologically relevant environment to allow cell proliferation and differentiation.

Confocal and fluorescence microscopy is typically used to image fluorescently labeled cells in 3D. However, the penetration depth is limited to <50 μm in dense and highly scattering tissues [5].

Light sheet fluorescence microscopy (LSFM) and two-photon excitation can image at greater depth (100s of μm), especially in combination with optical clearing [2]. However, they are not well suited to provide longitudinal measurements and suffer from the scattering generated by polymeric scaffolds. Optical coherence tomography (OCT) can be an alternative application to scan at greater depth without labeling the samples. It was recently shown that cell viability could be noninvasively and label-free inferred from the optical signal for 3D tissue engineering scaffolds and spheroids [6]. Still, OCT is limited in scanning depth in highly scattering cell-rich samples to a few 100s of μm.

Impedance-based cellular assays are an emerging alternative to overcome the limitations of scanning depth and scattered cell-rich environments, as non-invasive electrical current can travel several cms in tissues [7]. The passive electrical properties of biological cells are mostly associated with the interfacial polarisation at the double-lipid bilayer membrane, which acts as a capacitor that separates two ionic media, i.e., the cell cytoplasm and the surrounding medium [8]. Therefore, the dielectric properties inside and outside the cell membrane can be characterized by injecting a small non-invasive alternating current (AC) current through high conductive microelectrodes at low and high frequencies. These features make it worthwhile

to monitor cell proliferation [9], differentiation [10], and drug response [11].

When a sensor with multiple electrodes is used, the dielectric properties can be imaged by applying electrical impedance tomography (EIT) reconstruction methods [12]. Recent improvements in microelectrode technology enabled EIT to monitor the conductivity distribution $\boldsymbol{\sigma}$ at the cell scale. The essential parameters of EIT for tissue engineering in the literature are summarized in **Table 4.1**. Linderholm et al [13] developed the first EIT sensor for tissue engineering using an array of interdigitated electrodes to monitor the migration and time-varying resistivity of adhesive human epithelial stem cells. It has also been reported that the distribution of yeast cells sedimented at the bottom of the microchannel filled with purified water was visualized [14]. In our previous work, the Agile Tomography Group at the University of Edinburgh developed a miniature EIT sensor [15]. A 24-well-size circular chamber was embedded on a printed circuit board and seamlessly integrated with the data acquisition system, facilitating high sensitivity real-time monitoring of 3D cell samples. Cancer cell line samples in 3D hydrogels were imaged using this miniature EIT sensor [16].

Table 4.1.
EIT for tissue engineering in literature.

Cell type	Experimentation and electrode structure	References
Epithelial stem cells *YF 29*	• Time-difference EIT to monitor the cell migration over a period of several days • using rectangular electrodes embedded on a cell culture chamber	Linderholm et al. 2006 [13]
Yeast cells *Saccharomyces cerevisiae*	• Absolute EIT to image the cell sedimentation in purified water • using linear electrodes embedded on a multilayered diamond-shape sensor	Liu et al. 2016 [14]
Breast cancer cells *MCF-7*	• Time-difference EIT to monitor cell viability of a single sample of high-density cell spheroids under drug insultation over a period of several minutes • using circular electrodes embedded on a 24-well-size circular sensor	Yin et al. 2018 [15]
Breast cancer cells *MCF-7*	• Time-difference EIT to monitor cell viability of a single sample of high-density cell spheroids with hydrogels under drug insultation over a period of several minutes • using rectangular electrodes embedded on a 24-well-size circular sensor	Wu et al. 2018 [17]

In addition, conductivity changes $\Delta\sigma$ with time-reference data associated with cell mortality induced by cell lysis reagents matched cellular metabolic viability assay [17]. Despite these recent advances, there is still a need to measure the 3D cell viability of multiple samples simultaneously to provide biologically relevant data with sample repeats and controls. In this paper, we demonstrated simultaneous imaging and measurements without time-reference data,

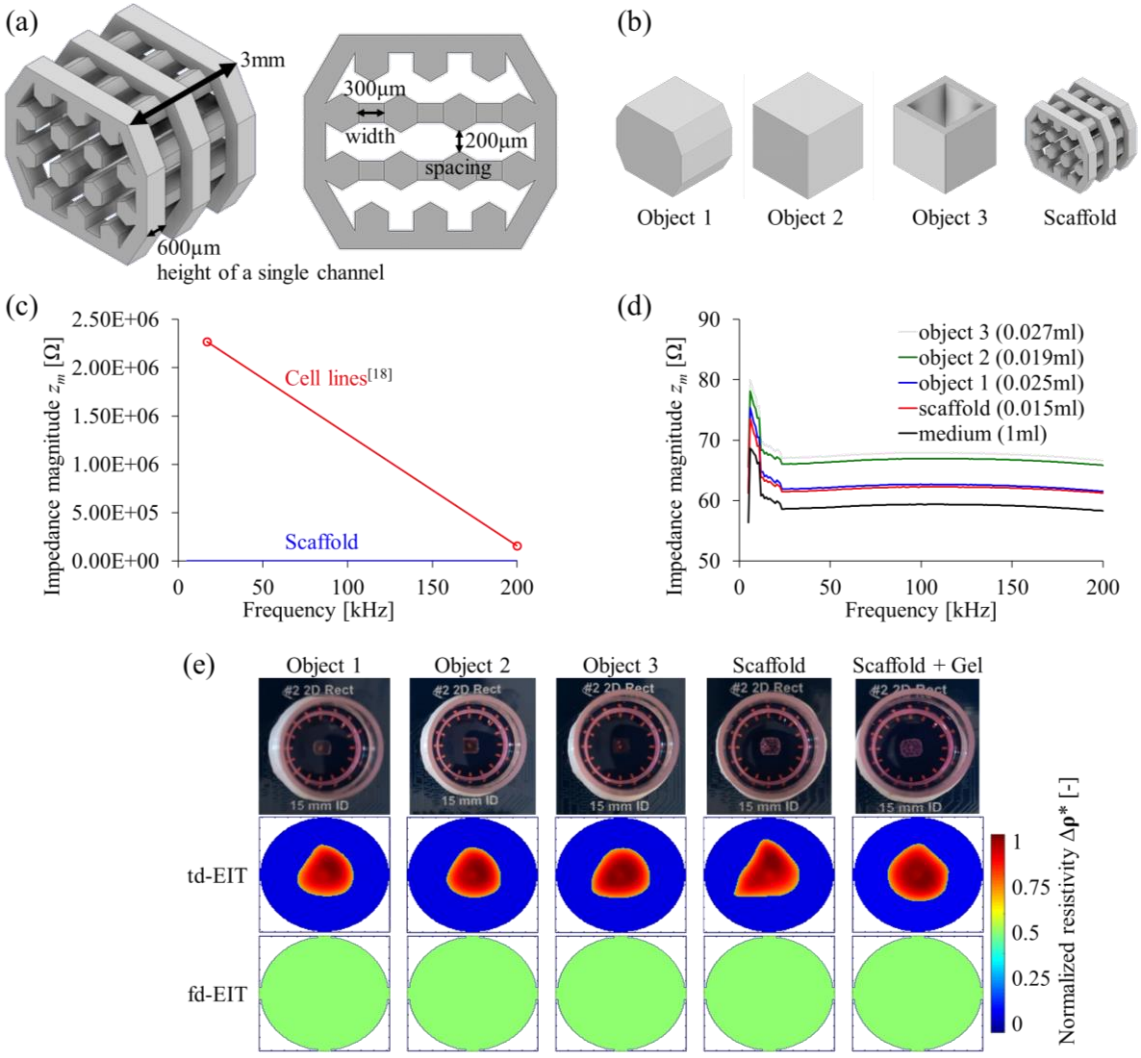

Figure 4.1. (a) A 3D scaffold fabricated layer by layer using a 3D printer with biocompatible materials, in which the design of the juxtaposed hexagonal posts enhances surface tension γ [17]. Total height: 3mm, width: 300µm, and spacing: 200µm. (b) 3D printed objects and scaffolds made out of the same resin. (c) Impedance spectra of the scaffold and cell lines measured by impedance analyzer. (d) Impedance spectra of 3D printed objects and control group, in which lower frequency peaks are attributed to contact impedance. (e) Normalized resistivity changes Δρ* of the scaffold, three other objects, and no object, which represent the conductivity changes of the control group and the presence of 3D-printed objects situated in the center of an RPMI-filled miniature sensor †Impedance spectra of cell lines in (c) is adapted from the work of A. Han, L. Yang, A. B. Frazier [19].

using a single EIT sensor, of cell viability for up to four 3D tissue engineering cultures of Human epithelial ovarian adenocarcinoma cell lines A2780 embedded in collagen gels. To this end, we introduced a 3D printed scaffold permissive to EIT measurement to hold and culture the 3D cell-gel system.

4.2. Materials and Methods

4.2.1. 3D scaffold design

We aimed to 3D print a biocompatible scaffold that could hold cells in solution, scaffolds, or gels without interfering with the EIT measurement. Our strategy was to create a geometric design that could effectively hold a certain amount of liquid or gel inside the cavity by surface tension γ to enhance cell-cell and cell–medium interactions, similarly to 2D solution confinement based on adjacent posts [18]. Juxtaposed hexagonal posts with a width and spacing of 300µm and 200µm, respectively, were chosen, as shown in **Figure 4.1 (a)**. Considering the minimum resolution of the 3D printer (Form2, Formlabs) and tolerable γ for maintaining the liquid, the height of the single channel was set to 600µm. There are three channels, and each is evenly connected by posts resulting in a sample with a total height of 3mm. The scaffold was 3D printed with a biocompatible resin (Dental SG Resin: Formlabs, Massachusetts, USA), onto which cells can adhere. In some cases, the scaffolds were filled with a collagen gel, as described below.

4.2.2. Electrical properties of scaffold

The frequency dependency of the scaffold was measured with a miniature EIT sensor filled with cell culture media [15]. We used the adjacent four-wire method, in which the injected electrode pair and the measurement electrode pair are independent [12]. In addition to the design described above, we printed three other scaffold designs made from the same resin, as shown in **Figure 4.1(b),** to investigate the frequency response of the scaffold material. All 3D-printed objects were designed with 3D-computer-aided design (CAD) software (Autodesk Inventor Professional 2019). Object 1 is the same octagonal design and scale as the scaffold, but the inside is filled with resin. Object 2 and object 3 are both cubes, 3mm on each side, with and without a cube-shaped cavity, respectively. In addition, a scaffold filled with a collagen gel (see Section 4.2.5) was also investigated. An impedance analyzer (E4990A, Keysight) was used to inject a sinusoidal current I0 (1mA, 5-200kHz) and record

the impedance magnitude z_m. First, in **Figure 4.1(c)**, the z_m of each 3D-printed object and the control group was significantly smaller than that of the cancer cell lines reported [19]. Therefore, the resin material has a very small contribution to the measurements compared to the cellular materials. In **Figure 4.1(d)**, z_m is directly proportional to the volume except for the relationship between object 1 and object 2. This relation explains current pathway does not change significantly whether the object is hollow or not. We observed fluctuations attributed to contact impedance at a lower frequency range (<10 kHz) [20]. While at a higher frequency range (10 kHz-200 kHz), we observed a slight change of z_m for all objects and media compared to cancer cell lines. Therefore, the scaffold's material can be assumed to be frequency independent in our frequency range of interest. **Figure 4.1(e)** shows the corresponding reconstructed images $\Delta\boldsymbol{\sigma}$, including a scaffold filled with a collagen gel. In the reconstructed values, a quarter of the lowest signal from cells in the experiment described later was set as a lower threshold. First, we can see the pictures of the samples inside the miniature EIT sensor (first row) and the corresponding conductivity change $\Delta\boldsymbol{\sigma}$ reconstructed using time-difference EIT (*td*EIT). As shown in the figures, *td*EIT failed to cancel the presence of the scaffolds in the reconstruction process. In contrast, when *fd*EIT reconstruction method is applied, a homogenous distribution is observed, as only negligible values are plotted compared to the cell dielectric properties. The image of the scaffold with gels is also shown, which validates that *fd*EIT is more robust than *td*EIT to eliminate the effect of gels, considering the substantial gap in z_m between the gel and cell with an intact insulating cell membrane. Taken together, these data show that we can design a 3D printed scaffold to support 3D cell culture that is effectively transparent to EIT.

4.2.3. Frequency-difference EIT

In EIT, the conductivity changes $\Delta\boldsymbol{\sigma}$ are estimated from impedance differences $\Delta\mathbf{Z}$, which are acquired through the current injection pair and impedance measurement pair, as depicted in **Figure 4.2** [12]. In *fd*EIT, they are presented as:

$$\Delta\mathbf{Z} = \frac{\mathbf{Z}_{obj} - \mathbf{Z}_{ref}}{\mathbf{Z}_{ref}} \tag{4.1}$$

where the impedances at an object frequency $\mathbf{Z}_{obj}$ and a reference frequency $\mathbf{Z}_{ref}$ are taken in a manner of element-wise divide. We have chosen *fd*EIT over *td*EIT for a reason stated in the previous section. Since *fd*EIT is resilient to change in the background throughout the experiment, it facilitates real-time monitoring [21]. Due to the ill-posedness of the EIT

inverse problem, Jacobian matrix **J** is introduced, derived from the electric field E of homogeneous conductivity distribution of each pixel at each measurement drive pattern [22]. Therefore, the mathematical formulation of EIT is expressed below [12].

$$\Delta \mathbf{Z} = \mathbf{J}\Delta\boldsymbol{\sigma} \tag{4.2}$$

Then, Equation (4.2) is solved to estimate $\Delta\boldsymbol{\sigma}$ by minimizing the problem [12]

$$\Delta\boldsymbol{\sigma} = \arg\min_{\Delta\boldsymbol{\sigma}} \| \Delta\mathbf{Z} - \mathbf{J}\Delta\boldsymbol{\sigma} \|^2 \tag{4.3}$$

In order to compensate for the error that comes from the high ill-posedness, the regularization term $\mathbf{R}(\Delta\boldsymbol{\sigma})$ is often applied to Equation (4.3) [12].

$$\Delta\boldsymbol{\sigma} = \arg\min_{\Delta\boldsymbol{\sigma}} \left(\| \Delta\mathbf{Z} - \mathbf{J}\Delta\boldsymbol{\sigma} \|^2 + \mathbf{R}(\Delta\boldsymbol{\sigma}) \right) \tag{4.4}$$

This equation can be interpreted as a constrained optimization problem [23]

$$\min_{\Delta\boldsymbol{\sigma},d} \left(\| d \|_{\mathrm{TV}} + \mathbf{H}(\Delta\boldsymbol{\sigma}) \right) \text{ such that } d = \boldsymbol{\Phi}(\Delta\boldsymbol{\sigma}) \tag{4.5}$$

where

$$\mathbf{H}(\Delta\boldsymbol{\sigma}) = \frac{1}{2} \| \Delta\mathbf{Z} - \mathbf{J}\Delta\boldsymbol{\sigma} \|^2 \text{ and } \| \boldsymbol{\Phi}(\Delta\boldsymbol{\sigma}) \|_{\mathrm{TV}} = \mathbf{R}(\Delta\boldsymbol{\sigma}) \tag{4.6}$$

Here $\|\cdot\|_{\mathrm{TV}}$ represents the TV norm. Both $\mathbf{H}(\Delta\boldsymbol{\sigma})$ and $\boldsymbol{\Phi}(\Delta\boldsymbol{\sigma})$ are the convex problems to solve the following equation by first converting them into an unconstrained problem [24]

$$\min_{\Delta\boldsymbol{\sigma},d} \left(\| d \|_{\mathrm{TV}} + \mathbf{H}(\Delta\boldsymbol{\sigma}) + \frac{1}{2} \| d - \boldsymbol{\Phi}(\Delta\boldsymbol{\sigma}) \|^2 \right) \tag{4.7}$$

Thereafter, Equation (4.7) can be adapted to new unconstrained optimization problems and Bregman iteration updates [25].

$$(\Delta\boldsymbol{\sigma}^{k+1}, d^{k+1}) = \min_{\Delta\boldsymbol{\sigma},d} \left(\| d \|_{\mathrm{TV}} + \mathbf{H}(\Delta\boldsymbol{\sigma}) + \frac{1}{2} \| d - \boldsymbol{\Phi}(\Delta\boldsymbol{\sigma}) - b^k \|^2 \right) \tag{4.8}$$

$$b^{k+1} = b^k + (\boldsymbol{\Phi}(\Delta\boldsymbol{\sigma}^{k+1}) - d^{k+1}) \tag{4.9}$$

where k is the iteration number and b is the measurement term (i.e., b^k=$\Delta\mathbf{Z}$ in the case of k=0). Consequently, $\Delta\boldsymbol{\sigma}$ is iteratively optimized through Equations (4.8) and (4.9) as an unconstrained problem. The discretized pixels within the sensing domain Ω, consisting of 128 × 128 elements, were finally grouped to display $\Delta\boldsymbol{\sigma}$. We applied the structural constraint to $\Delta\boldsymbol{\sigma}$, taking advantage of prior positioning information. The local maxima, considered the center of the conductivity perturbations, was first calculated from the original distribution $\Delta\boldsymbol{\sigma}$. Based upon it, the outermost boundary of the group for each inclusion was specified as Region of Interest (ROI) so that the pixels within a reasonable circular region can be included.

The diameter of the ROI circle, R_{max}, is selected empirically according to the size of the miniature EIT sensor. Here, R_{max} is set as 35 pixels in Ω. Finally, inside the boundary, a quarter of the local maxima was set as the lower threshold to enhance the recoverability.

$$\Delta\sigma^* = \begin{cases} \Delta\sigma \text{ if } \Delta\sigma > loc\max(\sigma)/4 \text{ (for all } i) \\ 0 \text{ otherwise} \end{cases} \quad (4.10)$$

in which $\Delta\sigma_i$ has to satisfy the condition that it is an element of each group. All the elements, i=1,…, N, in the final image $\Delta\sigma_i$* were normalized by their maximum value from 0 to 1 for better image interpretation.

4.2.4. Finite element simulation

Numerical simulations by COMSOL Multiphysics with an AC/DC module in the frequency domain study were performed to model the miniature EIT sensor. 16 electrodes are equally spaced on the circumference of the sensor and the ground electrode is situated in the center. The frequency selection is based on the β-dispersion mechanism and sensor configuration. We set the conductivity values **σ** of the cells to increase linearly and have the same value as the culture medium in case the most conductive cells are excited by higher frequency. The cells are located vertically and horizontally symmetry, as shown in **Figure 4.2**. The impedance magnitude z_m of the electrical double layer (EDL) at the interface between the electrode and the sample, known as contact impedance, strongly influences the boundary measurement if the contacting surface area is as small as the miniature EIT sensor used in this study (<0.5 mm2) [26]. Thus, the contact effect is considered by changing the material property on the electrode-medium interface. In order to reduce the computational cost,

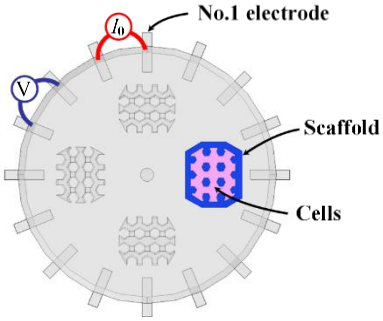

Figure 4.2. EIT measurement configuration using adjacent drive pattern, in which current I_0 is injected sequentially in adjacent electrode pairs and the voltages V are measured in the remaining electrode pairs. A pink object illustrates cells, which fill in the scaffold, a blue object. Scaffold does not influence *fd*EIT image; thus, it is removed in the simulation to reduce the computational cost

scaffolds, the blue area in **Figure 4.2**, were neglected because they are regarded as static and are equivalent to the background in *fd*EIT. Therefore, the cells, represented by the pink area, have a unique shape as we hypothesized the scaffolds are perfectly filled with cells. Consequently, the mesh consists of 551,744 voxels in the cylindrical sensing domain.

4.2.5. Cell culture

For details of cell culture and cell lines, see the pioneering work by A. Hallas-Potts, J. C. Dawson, and C. S. Herrington [27]. Human epithelial ovarian adenocarcinoma cell lines A2780 were kindly supplied by Charlie Gourley from the University of Edinburgh. The cell lines were authenticated using STR profiling (Public Health England). They were routinely cultured in RPMI Medium 1640 (1 ×) supplemented with 10% fetal calf serum (FCS), 1X non-essential amino acids (Sigma Aldrich, Irvine, UK), 100 µL/mL (v/v) penicillin-streptomycin, 1 mL sodium pyruvate (Sigma Aldrich) and 1 µL/mL bovine insulin (Sigma Aldrich). The cell lines were incubated at 37 °C with 5% CO2 in the medium, which was changed every 48h. They had been acclimatized to this medium for at least 3 months prior to experimentation. The experiment was conducted with cell lines no more than 10 passages apart to ensure biological repeats and limit the mutational effect of passaging, using 0.05% trypsin-EDTA (1×). 50% concentration collagen gel was prepared from rat tails as outlined in previous work [28]. The collagen mix was prepared, and all ingredients were kept on ice to ensure the collagen did not set; 125 µL Acetic acid (GIBCO, Life Technologies) and 30 µL MEM (10 ×) (Sigma Aldrich) was added to 125 µL rat tail collagen. Then 0.25 M NaOH (in-house) was added dropwise whilst gently mixing until the collagen mix turned orange but not pink (approximately 30 µL NaOH). Once the cell lines attained enough confluency, those are subsequently resuspended in 15 µL collagen mix gel and quickly seeded in the scaffold. The samples were lastly incubated at 37 °C, 5% CO2 for 10 min to allow the mixture to set. After visualizing the samples with microscopy, the whole area occupied by cells and the sum of cell counts in those images were calculated using the Renyi entropy threshold [29] to evaluate quantitatively.

4.3. Results

4.3.1. Simulation Results

In this study, the impedance measurements were simulated at low (10 kHz) and high frequency (100 kHz) to capture the β-dispersion associated with the cell membrane. We simulated two cases shown in **Figure 4.3**, in which the background conductivity σ_{bg} was fixed as σ_{bg}=1.6 S/m for both cases. First, we simulated four cell-seeded scaffolds with increasing concentration, as shown at the top of **Figure 4.3(a)**. Then, we simulated four cell-seeded scaffolds, with one having a lower cell concentration than the others, as shown in **Figure 4.3(d)**. In the first case, the sample at ROI 1 is the most resistive, and σ increased anti-clockwise towards ROI 2, ROI 3, and ROI 4, in which each sample (i=1, 2, 3, and 4) has the following conductivities σ at low and high frequencies: $\sigma_{1\text{-low}}$=1.2 S/m, $\sigma_{2\text{-low}}$=0.8 S/m, $\sigma_{3\text{-low}}$=0.4 S/m, and $\sigma_{4\text{-low}}$=1e-4 S/m at 10 kHz to $\sigma_{1\text{-high}}$=1.6 S/m, $\sigma_{2\text{-high}}$=1.2 S/m, $\sigma_{3\text{-high}}$=0.8 S/m, and $\sigma_{4\text{-high}}$=0.4 S/m at 100 kHz. This relationship reflects that a higher number of live cells lead to a decrease in σ (increase in resistivity ρ) since cell membranes act as resistive material at these frequencies. Then, in the second case, σ at low and high frequencies of three samples (red in **Figure 4.3(d)**) were set at $\sigma_{1\text{-low}}$, $\sigma_{2\text{-low}}$, $\sigma_{4\text{-low}}$=1.2 S/m at 10 kHz and $\sigma_{1\text{-high}}$, $\sigma_{2\text{-high}}$, $\sigma_{4\text{-high}}$=1.6 S/m at 100 kHz. Meanwhile, σ for the fourth sample (blue in **Figure 4.3(d)**) was set to $\sigma_{3\text{-low}}$=1e^{-4} S/m at 10 kHz to $\sigma_{3\text{-high}}$=0.4 S/m at 100 kHz. The relative permittivity ε_r was identically specified as 80 as it causes only trivial perturbations in the measurement at this

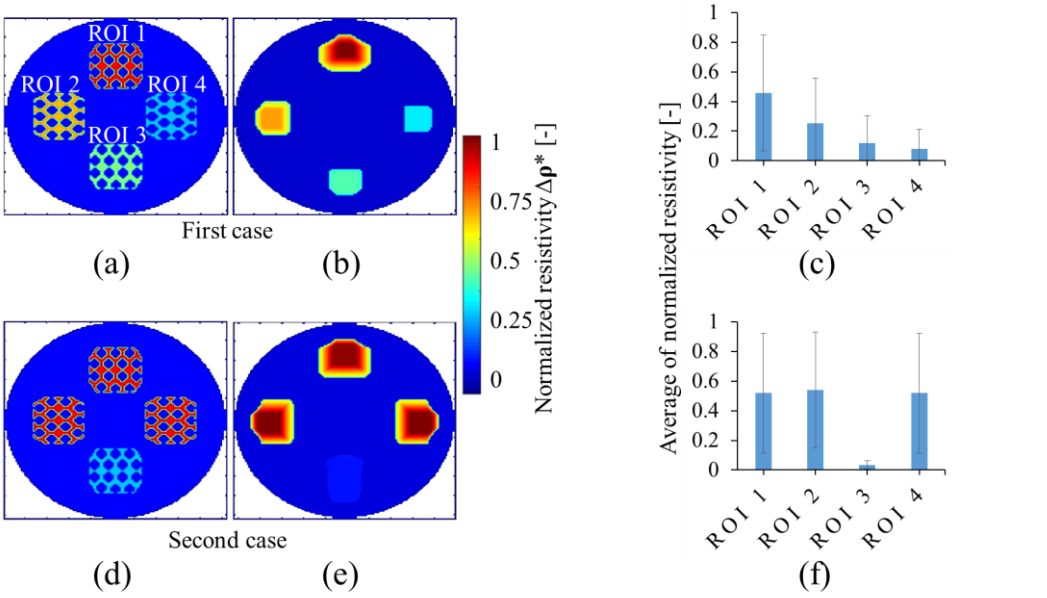

Figure 4.3. Simulation of two conductivity cases; (a) all the cells have various conductivities σ, which decrease anti-clockwise direction, and (d) only one group of cells has different conductivity σ. (b), (e) The normalized resistivity changes Δρ* reconstructed at 10 kHz and 100 kHz in each case. (c), (f) The quantitative results are expressed as mean ± s.d. for a representative of Δρ* at each ROI.

frequency range. Considering the reciprocity theory in the adjacent drive pattern, the degrees of freedom of the measurement is M=16×(16-3)/2=104 (the dimension of the impedance differences $\Delta\mathbf{Z}$).

4.3.2. Investigation of *fd*EIT

The normalized resistivity changes $\Delta\boldsymbol{\rho}^*=1/\Delta\boldsymbol{\sigma}^*$ of the first case are given in **Figure 4.3(b)**, showing that their cell concentration can be elucidated and reconstructed in the correct order, i.e., the resistance dropped off anti-clockwise. The mean values and standard deviations of $\Delta\boldsymbol{\rho}^*$ at each ROI are also given in **Figure 4.3(c)**, showing a nonlinear decreased trend. In terms of morphology, a close representation of the original distribution (cell filling the scaffold with a distinct pattern) was not retrieved due to the inherent low spatial resolution of EIT. Nevertheless, our simulation results demonstrate that the miniature EIT sensor can simultaneously measure multiple (n=4) samples of various $\Delta\boldsymbol{\rho}^*$ associated with the presence of cells at various concentrations.

In this study, we chose *fd*EIT to enable real-time monitoring and the elimination of the scaffold effect. It is worth noting that samples were successfully imaged with various magnitudes of conductivity σ, even though there is an identical step of σ in frequency (increments of 0.4 S/m from 10 kHz to 100 kHz), which seemingly unable *fd*EIT to present the contrast. This phenomenon is further explained in the discussion section.

Figure 4.3(e) shows $\Delta\boldsymbol{\rho}^*$ of the second case. A clear difference between the higher and lower resistance groups can be seen in $\Delta\boldsymbol{\rho}^*$. The mean values and standard deviations of $\Delta\boldsymbol{\rho}^*$ at each ROI are represented in **Figure 4.3(f)**. No significant differences between samples 1, 2, and 4 were set to the same σ in the simulation. These small discrepancies in $\Delta\boldsymbol{\rho}^*$ can be explained by current and potential distribution affected by the presence of multiple samples in the sensors. The element's value of $\Delta\boldsymbol{\rho}^*$ associated with sample 3 was significantly lower than in other groups. Taken together, these results showed that we can measure multiple repeats in the EIT sensor and that $\Delta\boldsymbol{\rho}^*$ associated with cell number is not significantly affected by the presence of other samples.

4.3.3. Experiment

We prepared four types of samples with various cell densities inside the scaffolds, i.e., 0.5, 1.0, 1.5, and 2.0 $\times 10^6$ /mL. The scaffolds were seeded with cells embedded in

collagen gels, as previously described. Before conducting the EIT experiment, fluorescence microscopy merge images were taken using an EVOS FL digital inverted microscope equipped with a 4X Plan LWD PH lens (0.13NA). Cells were stained with DAPI and Hoechst 33342 (Thermo Fisher Scientific). DAPI and Hoechst 33342 primarily stain the nucleus of formaldehyde fixed and live cells, respectively, their excitation wavelengths are in the UV range (~365nm), and they emit visible blue light. Both stains provide a robust high-contrast signal with which to locate cells grown (mainly stained in blue) in non-standard conformations, i.e., the scaffolds (mainly stained in red). We observed in **Figure 4** that cells were largely confined within the scaffolds. The cells were located not only inside the gel space but also attached to the posts of the scaffold, as shown in **Figure 4.4(a)**. The total area that cells occupied in the image (0.21*0.16 cm^2)

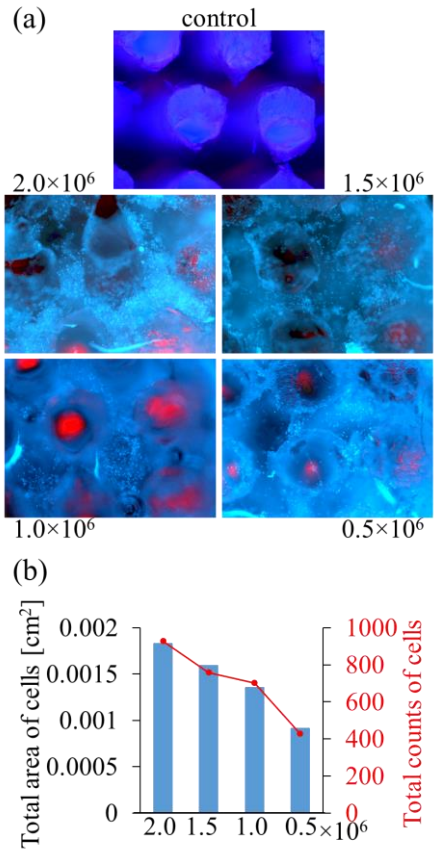

Figure 4.4. Microscope images with various cell densities. Fluorescence microscopy merge images were taken using Inverted Fluorescent Microscope (Thermo Scientific) equipped with 4X Plan LWD PH lens (0.13NA). Cells were stained with DAPI and Hoechst 33342 (Thermo Fisher Scientific), which provide a robust high-contrast signal with which to locate cells grown (mainly stained in blue) in non-standard conformations, i.e., the scaffolds (mainly stained in red). (b) Total area and total counts of cells were calculated using the Renyi entropy threshold.[29]

and the total counts of cells were calculated using the Renyi entropy threshold [29]. The results were consistent with the cell seeding concentration in **Figure 4.4(b)**, and the cells were alive for 48h within our scaffold.

Next, five cases are explored, as shown in **Figure 4.5**. The scaffolds with cells were carefully placed in the miniature EIT sensor, as shown in **Figure 4.5(a)**. Similarly to the simulation settings, the impedance magnitude z_m for the reference and the object at 10 kHz and 100 kHz were acquired for *fd*-EIT image reconstruction, respectively, for the recovery of the normalized resistivity changes $\Delta\boldsymbol{\rho}^*$. It is clearly seen that resistance decreased anti-clockwise, corresponding to the decrease in cell density, as shown in **Figure 4.5(b)**. In spite of morphological disparity with ground truth, $\Delta\boldsymbol{\rho}^*$ in **Figure 4.5(b)** are similar to those of the ground truth. The mean values and standard deviations of $\Delta\boldsymbol{\rho}^*$ at each ROI are represented in **Figure 4.5(d)**, enabling us to differentiate all the cell groups. As a result, *fd*EIT was highly robust in distinguishing the cell density variations in the 3D scaffolds and reconstructed the $\Delta\boldsymbol{\rho}$ as an indicator of cell viability

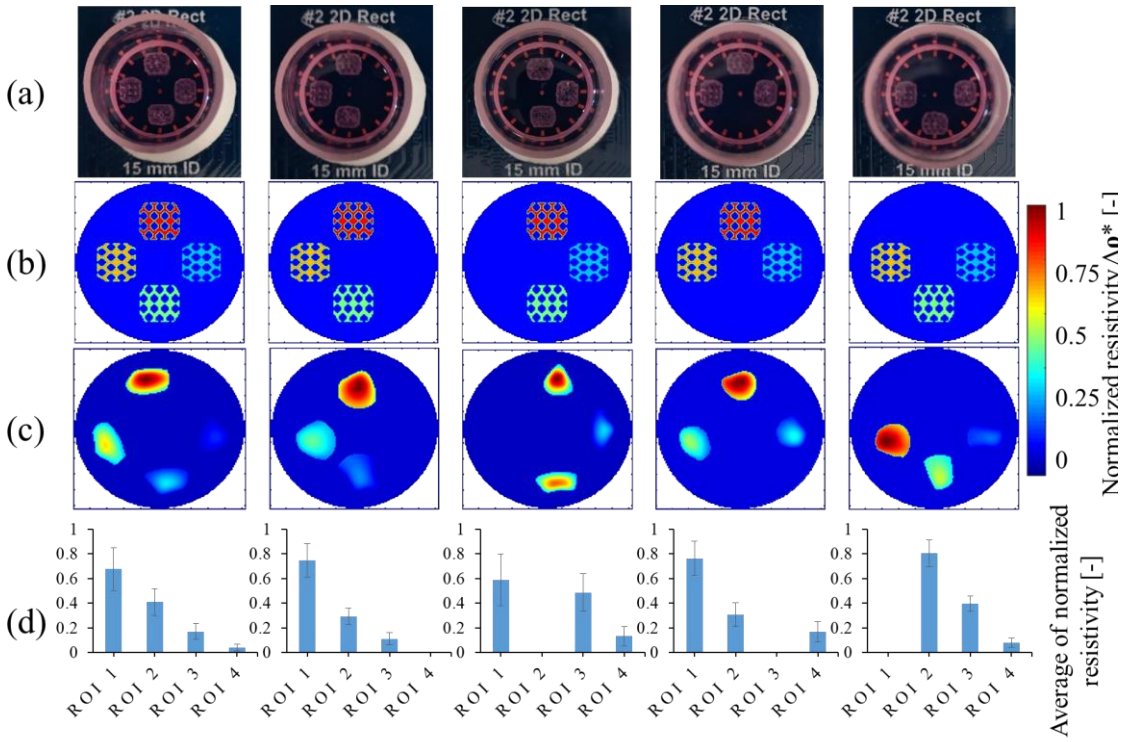

Figure 4.5. The normalized resistivity changes Δρ* reconstructed at 10 kHz and 100 kHz in each case. (a) Sensor image with scaffolds. (b) Ground truth. (c) The reconstructed results of Δρ*. (d) The quantitative results are expressed as mean ± s.d. for a representative of Δρ* at each ROI.

4.4. Discussion

In this chapter, 3D printed scaffolds compatible with EIT were designed and characterized in order to demonstrate *in silico* and *in vitro* their potential for performing parallel measurements of 3D cell culture concentration and growth in a single sensor. The ability to perform measurement repeats and controls in the same sensor will pave the way towards the use of EIT in tissue engineering and drug screening applications.

Our strategy was to optimize the scaffold design so cells could be cultured in suspension by adhering to scaffold trends and forming 3D tissues or within gels. In a similar concept to cell culture multiwell plates, our design enabled to image multiple samples, thus allowing experimental repeats and control in the same EIT sensor. The challenge was to minimize the impact of the scaffold on the cell conductivity measurement by allowing the current to flow while still holding the cell's solution. In addition, we chose a material that was biocompatible, compatible with 3D printing, and with dielectric properties constant over the frequency range of interest (the β-dispersion).

In previous studies, we demonstrated that EIT could be applied to tissue engineering applications and their typical scale (~mm) by reducing the size of the EIT sensors and adapting the regularisation techniques [15], [21], [30]. In particular, we previously showed *in silico* and *in vitro* its potential for drug screening by measuring the cell viability of cell spheroid and its transient change when exposed to the toxic compound [17]. In addition, we demonstrated the superiority of frequency-difference EIT (*fd*-EIT) over time-difference EIT (*td*-EIT) to measure samples over an extended period [16]; and an equivalent circuit analysis was developed to compensate for the leakage current through coupling capacitances to the ground [31].

Here, we demonstrate that we can use 3D scaffolds permissive to EIT that can support 3D cell culture to image and measure the cell viability of multiple samples; hence, performing in a similar way to the transparent plastic culture well for optical imaging. Our 3D printed scaffold design and the resin dielectric properties should allow researchers in the future to design more complex structures in which multiple 3D cell cultures, such as spheroids or organoids, could be held and measured label-free and noninvasively throughout growth and differentiation in a single EIT sensor.

Based on Equation 4.1, if *fd*-EIT can be only sensible to frequency difference, it seems impossible to differentiate multiple objects when the steps of conductivity increase between

low and high frequency are the same. As briefly described in the previous work [32], *fd*-EIT retrieve two characteristics; 1) the frequency dependence of objects and 2) the conductivity value itself. The latter principle suggests that *fd*EIT presents a contrasting image even if conductivities do not change with frequency, which can be explained further by analyzing the simulation described in **Figure 4.3**. We explored how the presence of multiple resistances affects the current density j and electric potential φ by configuring the well-known formula $\sigma=j/\varphi$. Here, $\Delta\sigma$ is influenced by Δj and $\Delta\varphi$ as a function of frequency dependency in *fd*-EIT. We quantitatively analyzed the contrasts in j and φ, Δj and $\Delta\varphi$, of **Figure 4.3**, which is shown in **Figure 4.6**, with four stimulation patterns (1, 5, 9, and 13) at four independent positions (x_1, x_2, x_3, and x_4). We show the equipotential lines of only the first case in **Figure 4.6(a)**, where fine gradient lines can be observed around stimulus electrodes that become coarser with the distance from stimulus electrodes. Again, the steps of conductivity increase over frequencies are identical; thus, one may think the contrast cannot be observed. However, the

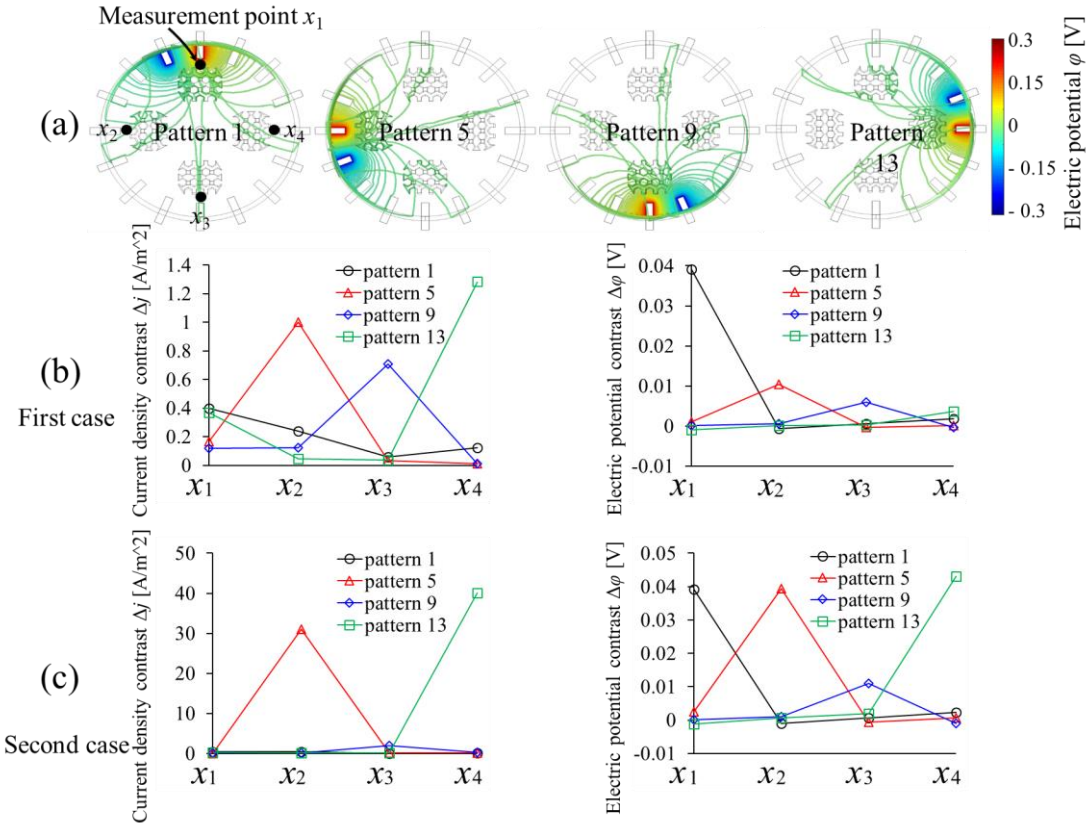

Figure 4.6. (a) Equipotential lines of the first simulation case with four stimulation patterns (1, 5, 9, and 13). Simulation results of current density contrast Δj and electric potential contrast $\Delta\varphi$ with four stimulation patterns at four independent positions, x_1, x_2, x_3, x_4 of the first case (b) and the second case (c) as described in Figure 4.3(a) and (d), respectively.

fluctuations can be seen for both Δj and $\Delta\varphi$ in **Figure 4.6(b)** and **(c)**. In both settings, $\Delta\varphi$ has a more significant weight than that of Δj based on their magnitude considering the normalization characteristic, Δj influencing $\Delta\boldsymbol{\rho}^*$ more significantly. On the other hand, the slight difference of $\Delta\boldsymbol{\rho}^*$, in which corresponding steps were set as identical in simulation setups, in **Figure 4.3(c)**, matches the relation of Δj. These irregularities of Δj enable *fd*-EIT to elucidate multiple objects even in the case where the steps of conductivity increments are identical among the objects. Furthermore, their relationships with frequency dependence and absolute conductivity value can be explained through multiple samples.

4.5.Summary

There is a growing need for real-time, non-invasive quantitative techniques capable of effectively monitoring the growth and behavior of 3D cell culture. In this paper, we demonstrated the feasibility of *fd*EIT for differentiating 3D cell samples (n>2). To this end, we have carefully designed a biocompatible scaffold that confines cell samples in space to allow parallel measurement of multiple samples in a single EIT sensor. Our design minimizes current pathway alteration with electrical properties similar to the culture medium, especially regarding frequency dependency. We fabricated the scaffold by 3D printing, ensuring it could hold liquid with surface tension area and keep the cells alive for 48h.

We retrieved the cell concentration of up to four scaffolds non-destructively in real time. Furthermore, quantitative analysis in the field of current density and potential distribution was conducted to explain the feasibility of cell differentiation using *fd*EIT. This study paves the way towards EIT imaging and measurements that could help to evaluate quantitatively and noninvasively tissue engineering samples, such as engineered tissues, spheroids, and organoids, in the production line.

References

[1] K. Bardsley, A. J. Deegan, and A. J. El Haj, “Current State-of-the-Art 3D Tissue Models and Their Compatibility with Live Cell Imaging,” *Adv. Exp. Med. Biol.*, vol. 1035, no. October, pp. 3–18, 2017, doi: 10.1007/978-3-319-67358-5.

[2] F. Pampaloni, E. G. Reynaud, and E. H. K. Stelzer, “Air-liquid interface Growth medium Apoptosis/anoikis Aggregation Polarization Differentiation,” *Nat. Rev.*

Mol. Cell Biol., vol. 8, no. october, pp. 839–845, 2007, [Online]. Available: www.nature.com/reviews/molcellbio.

[3] S. F. Badylak, D. O. Freytes, and T. W. Gilbert, "Extracellular matrix as a biological scaffold material: Structure and function," *Acta Biomater.*, vol. 5, no. 1, pp. 1–13, 2009, doi: 10.1016/j.actbio.2008.09.013.

[4] H. S. Song, O. S. Kwon, J. H. Kim, J. Conde, and N. Artzi, "3D hydrogel scaffold doped with 2D graphene materials for biosensors and bioelectronics," *Biosens. Bioelectron.*, vol. 89, pp. 187–200, 2017, doi: 10.1016/j.bios.2016.03.045.

[5] K. Carlsson and N. Åslund, "Confocal imaging for 3-D digital microscopy," *Appl. Opt.*, vol. 26, no. 16, p. 3232, 1987, doi: 10.1364/ao.26.003232.

[6] N. J. Martucci *et al.*, "Nondestructive Optical Toxicity Assays of 3D Liver Spheroids with Optical Coherence Tomography," *Adv. Biosyst.*, vol. 2, no. 3, pp. 1–9, 2018, doi: 10.1002/adbi.201700212.

[7] W. Gamal, H. Wu, I. Underwood, J. Jia, S. Smith, and P. O. Bagnaninchi, "Impedance-based cellular assays for regenerative medicine," *Philos. Trans. R. Soc. B Biol. Sci.*, vol. 373, no. 1750, 2018, doi: 10.1098/rstb.2017.0226.

[8] K. Asami, "Characterization of heterogeneous systems by dielectric spectroscopy," *Prog. Polym. Sci.*, vol. 27, no. 8, pp. 1617–1659, 2002, doi: 10.1016/S0079-6700(02)00015-1.

[9] R. Szulcek, H. J. Bogaard, and G. P. van Nieuw Amerongen, "Electric cell-substrate impedance sensing for the quantification of endothelial proliferation, barrier function, and motility," *J. Vis. Exp.*, no. 85, pp. 1–12, 2014, doi: 10.3791/51300.

[10] P. O. Bagnaninchi and N. Drummond, "Real-time label-free monitoring of adipose-derived stem cell differentiation with electric cell-substrate impedance sensing," *Proc. Natl. Acad. Sci. U. S. A.*, vol. 108, no. 16, pp. 6462–6467, 2011, doi: 10.1073/pnas.1018260108.

[11] C. Xiao and J. H. T. Luong, "On-line monitoring of cell growth and cytotoxicity using electric cell-substrate impedance sensing (ECIS)," *Biotechnol. Prog.*, vol. 19, no. 3, pp. 1000–1005, 2003, doi: 10.1021/bp025733x.

[12] D. S. Holder, *Electrical impedance tomography: methods, history and applications*. Bristol, UK: IOP Publishing, 2005.

[13] P. Linderholm, T. Braschler, J. Vannod, Y. Barrandon, M. Brouard, and P. Renaud, "Two-dimensional impedance imaging of cell migration and epithelial stratification," *Lab Chip*, vol. 6, no. 9, pp. 1155–1162, 2006, doi: 10.1039/b603856e.

[14] X. Liu, Y. Cui, J. Yao, H. Obara, T. Zhao, and M. Takei, “Development of electrical impedance tomography system for cell sedimentation detection in electrode-multilayered microchannel,” *2016 Int. Symp. Micro-NanoMechatronics Hum. Sci. MHS 2016*, no. 5, pp. 5–10, 2017, doi: 10.1109/MHS.2016.7824243.

[15] X. Yin, H. Wu, J. Jia, and Y. Yang, “A micro EIT sensor for real-time and non-destructive 3-d cultivated cell imaging,” *IEEE Sens. J.*, vol. 18, no. 13, pp. 5402–5412, 2018, doi: 10.1109/JSEN.2018.2834509.

[16] H. Wu, W. Zhou, Y. Yang, J. Jia, and P. Bagnaninchi, “Exploring the potential of electrical impedance tomography for tissue engineering applications,” *Materials (Basel).*, vol. 11, no. 6, pp. 1–11, 2018, doi: 10.3390/ma11060930.

[17] H. Wu, Y. Yang, P. O. Bagnaninchi, and J. Jia, “Electrical impedance tomography for real-time and label-free cellular viability assays of 3D tumour spheroids,” *Analyst*, vol. 143, no. 17, pp. 4189–4198, 2018, doi: 10.1039/c8an00729b.

[18] C. P. Huang *et al.*, “Engineering microscale cellular niches for three-dimensional multicellular co-cultures,” *Lab Chip*, vol. 9, no. 12, pp. 1740–1748, 2009, doi: 10.1039/b818401a.

[19] A. Han, L. Yang, and A. B. Frazier, “Quantification of the heterogeneity in breast cancer cell lines using whole-cell impedance spectroscopy,” *Clin. Cancer Res.*, vol. 13, no. 1, pp. 139–143, 2007, doi: 10.1158/1078-0432.CCR-06-1346.

[20] B. W. Veal, P. M. Baldo, A. P. Paulikas, and J. A. Eastman, “Understanding Artifacts in Impedance Spectroscopy,” *J. Electrochem. Soc.*, vol. 162, no. 1, pp. H47–H57, 2015, doi: 10.1149/2.0791501jes.

[21] Y. Yang and J. Jia, “A multi-frequency electrical impedance tomography system for real-time 2D and 3D imaging,” *Rev. Sci. Instrum.*, vol. 88, no. 8, 2017, doi: 10.1063/1.4999359.

[22] J. Lehr, “A Vector Derivation Useful in Impedance Plethysmographic Field Calculations,” *IEEE Trans. Biomed. Eng.*, vol. BME-19, no. March, pp. 156–157, 1972, doi: 10.1111/j.1468-1331.2009.02820.x.

[23] L. I. Rudin, S. Osher, and E. Fatemi, “Nonlinear total variation based noise removal algorithms,” *Phys. D Nonlinear Phenom.*, vol. 60, no. 1–4, pp. 259–268, 1992, doi: 10.1016/0167-2789(92)90242-F.

[24] E. Y. Sidky and X. Pan, “Image reconstruction in circular cone-beam computed tomography by constrained, total-variation minimization,” *Phys. Med. Biol.*, vol. 53, no. 17, pp. 4777–4807, 2008, doi: 10.1088/0031-9155/53/17/021.

[25] T. Goldstein and S. Osher, “The split Bregman method for L1-regularized problems,” *SIAM J. Imaging Sci.*, vol. 2, no. 2, pp. 323–343, 2009, doi: 10.1137/080725891.

[26] W. B. Russel, D. A. Saville, and W. R. Schowalter., *Colloidal Dispersions*. Cambridge, England, 1991.

[27] A. Hallas-Potts, J. C. Dawson, and C. S. Herrington, "Ovarian cancer cell lines derived from non-serous carcinomas migrate and invade more aggressively than those derived from high-grade serous carcinomas," *Sci. Rep.*, vol. 9, no. 1, pp. 1–10, 2019, doi: 10.1038/s41598-019-41941-4.

[28] P. Timpson *et al.*, "Organotypic collagen I assay: A malleable platform to assess cell behaviour nin a 3-dimensional context," *J. Vis. Exp.*, no. 56, pp. 1–4, 2011, doi: 10.3791/3089.

[29] A. Renyi, "ON MEASURES OF ENTROPY AND INFORMATION," in *Proceedings of 4th Berkeley Symposium on Mathematics, Statistics and Probability*, 1961, vol. 1, pp. 547–561.

[30] N. Jamil, S. Smith, Y. Yang, J. Jia, P. Bagnaninchi, and E. Gonzalez-Fernandez, "Design and fabrication of microelectrodes for electrical impedance tomography of cell spheroids," *IECBES 2016 - IEEE-EMBS Conf. Biomed. Eng. Sci.*, pp. 426–431, 2016, doi: 10.1109/IECBES.2016.7843486.

[31] H. Wu, Y. Yang, P. O. Bagnaninchi, and J. Jia, "Calibrated Frequency-Difference Electrical Impedance Tomography for 3D Tissue Culture Monitoring," *IEEE Sens. J.*, vol. 19, no. 18, pp. 7813–7821, 2019, doi: 10.1109/JSEN.2019.2919182.

[32] J. K. Seo, J. Lee, S. W. Kim, H. Zribi, and E. J. Woo, "Frequency-difference electrical impedance tomography (fdEIT): Algorithm development and feasibility study," *Physiol. Meas.*, vol. 29, no. 8, pp. 929–944, 2008, doi: 10.1088/0967-3334/29/8/006.

Chapter 5

Multifrequency Electrical Impedance Tomography with Ratiometric Preprocessing for Imaging Human Body Compartments

5. Multifrequency Electrical Impedance Tomography with Ratiometric Preprocessing for Imaging Human Body Compartments

5.1. Research Motivation

Electrical impedance tomography (EIT) was developed as a point-of-care imaging of the conductivity distribution in human body compartments by current injection and voltage measurement on the body surface [1]. EIT focuses on a larger field view of the structure and provides real-time and long-term imaging but has less accuracy than other point-of-care imaging modalities such as ultrasound [2]. In the point-of-care imaging of body compartments, a structural image of the calf is required for evaluating the health conditions in clinical practice. The point-of-care imaging of calf compartments is essential for evaluating a) the thickness and inhomogeneity of subcutaneous adipose tissue (SAT) related to edema [3] and b) the bone strength related to osteoporosis [4].

In EIT, the raw impedance z_m is often preprocessed to distinguish the source of z_m which comes from an anomaly, background, or external noise. Generally, EIT is categorized into root transformation (RT) [5], data decomposition (DD) [6], time-difference (TD), and frequency-difference (FD) methods by preprocessing viewpoints. RT method modifies the amplitude range of z_m by rooting; however, RT method is impractical for calf compartments imaging due to the mutable dependency on the optimal root index, which must be known prior to the image reconstruction. DD method decomposes z_m by means of the positive and negative regions of its sensitivity matrix **S**; nonetheless, DD method does not improve highly the image quality as compared with the non-preprocessing method because of the simply normalized **S**. TD method normalizes the perturbation between z_m and the reference impedance z^{ref} over time to extract anomalies from the background and the external noise. According to a review paper [7], TD, RT and DD methods are not practical without any *a priori* information.

The advantages and drawbacks of classical frequency-dependence EITs are summarized in **Table 5.1**.

Among the preprocessing, frequency-difference EIT (*fd*-EIT) is reliable [8] because *fd*-EIT does not require any *a priori* information on z^{ref} from individual persons after physiological events. Various frequency spectra in biological tissues are the source of *fd*-EIT

TABLE 5.1
ADVANTAGES AND DRAWBACKS AMONG CLASSICAL FREQUENCY DEPENDENCE EITS.

Classical EIT	Description	Advantage	Drawback
frequency-difference EIT (*fd*-EIT) [9]	Normalized perturbation between **Z** at one frequency and a reference frequencies is reconstructed.	High distinguishability	High conductivity contrast μ, Low robustness to frequency-dependency
frequency-difference adjacent EIT (*fda*-EIT) [10]	Normalized perturbation between **Z** at adjacent frequencies is reconstructed.	Low μ, High robustness to frequency-dependency	Low distinguishability, Low robustness to heterogeneous background
weighted *fd*-EIT (*wfd*-EIT) [11]	Frequency-dependence of homogeneous background conductivity is corrected.	High robustness to frequency-dependency, High distinguishability	High μ, The constraint of having to be homogeneous background
multiple *wfd*-EIT (*mwfd*-EIT) [12]	Frequency-dependence of heterogeneous background conductivity is corrected.	High robustness to frequency-dependence heterogeneous background	Low distinguishability
mf-EIT using spectral constraints [13]	The volume fraction distribution of the known component tissues is reconstructed in a nonlinear manner.	Frequency independency of the reconstructed parameters	Impractical *a priori* about volume fraction on each compartment

[9], where the individual conductivities σ_f on each tissue are nonlinearly related to z_m concerning the *f*-th frequency. Despite the above-mentioned advantages, *fd*-EIT suffers from image deterioration in the case of high conductivity contrast μ between anomaly $\sigma^a{}_f$ and background $\sigma^{bg}{}_f$, where μ is defined as $\mu = (\sigma^a{}_f - \sigma^{bg}{}_f) / \sigma^{bg}{}_f$. For instance, assuming the human body is composed of SAT and bone as $\sigma^a{}_f$ and muscle as $\sigma^{bg}{}_f$, μ is approximately 95% based on their conductivity values [10]. Even though *fd*-EIT is usually able to reconstruct a structural image under the only low $\mu < \pm 20\%$ condition which does not cover the human body high μ, the image quality in the case of high μ over ±20% is deteriorated because of the linear approximation of the inverse problem in the nonlinear forward model [11], [12]. On the other hand, frequency-difference adjacent EIT (*fda*-EIT) is alternatively used in order to decrease μ, in which the perturbation between z_m at the *f*-th and the adjacent (*f*+1)-th frequencies is normalized [13]. In that way, the inverse problem is likely to be solved in $\mu <$ ±20%. Unfortunately, the decreased μ usually leads to low distinguishability, which means that Hadamard's third condition, called "instability", is violated to worsen the ill-posed nature

of the inverse problem [1]. Therefore, *fda*-EIT may produce a blurred image due to the low distinguishability as well as the artifact from the frequency dependency on the heterogeneous background. A weighted *fd*-EIT (*wfd*-EIT) only compensates for the frequency-dependency on the homogeneous background and suffers from the heterogeneous background [14] as well as high μ. A multiple *wfd*-EIT (*mwfd*-EIT) compensates for high μ in the heterogeneous background by subtracting multiple baselines concerning several frequencies; however, the image quality of *mwfd*-EIT becomes insufficient due to the inherent low distinguishability in multifrequency EIT (*mf*-EIT) [15]. Unfortunately, an alternative *mf*-EIT using spectral constraints [16] highly relies on impractical *a priori* information about volume fraction on each compartment. Overall, the assumption of classical EIT is invalid; namely, either they cannot achieve the condition $\mu < \pm 20\%$ while maintaining high distinguishability or suffer from the heterogeneous background without any *a priori* information.

In order to make the breakthrough of drawbacks among classical frequency-dependence EITs, we propose *mf*-EIT with a ratiometric preprocessing (ratiometric EIT) for boosting robustness under high μ condition. The framework of "ratiometric" methods uses the ratio of two measurement signals and is commonly used in optical and electrical sensing to interpret better the phenomenon of anomaly [17], [18]. Recently, ratiometric impedance was reported to reduce the variation of measurement noise and amplify the differences between subjects in biometrics [19]. Since the distinguishability in EIT is characterized by 4 parameters: noise, conductivity, size of anomaly, and frequency-dependency [20], the above-mentioned advantages for the ratiometric method motivate us to apply it in EIT as a preprocessing. However, the ratiometric impedance is not able to be directly applied in EIT without modifying $\mathbf{S}$; thus, ratiometric impedance is averaged to make it applicable to EIT. Consequently, under high μ condition, the individual conductivities with widely varying scales that determine impedance are considered to be balanced, resulting in a minimized μ. Given the above ideas, ratiometric EIT is developed in order to minimize μ and increase the distinguishability because inherently μ is high in the human body and the distinguishability is low in EIT. This study aims to achieve four objectives which are 1) to propose ratiometric EIT which minimizes conductivity contrast μ while maintaining high distinguishability in the heterogeneous background without any *a priori* information, 2) to evaluate the robustness of the proposed method under the variant conditions of μ, 3) to evaluate the reconstruction performance in the experiment with eight subjects' calves by comparing with ultrasound

images of SAT and bone tibia, and 4) to discuss the distinguishability of ratiometric EIT. The key abbreviations and symbols used in this study are listed in **Table 5.2**.

TABLE 5.2
KEY ABBREVIATIONS AND SYMBOLS

μ	Conductivity contrast
z	Impedance
σ	Conductivity
m	Measurement number ($1 \leq \xi \leq M$)
n	Spatial resolution ($1 \leq n \leq N$)
ξ	Selected measurement number as a denominator ($1 \leq \xi \leq M$)
f	Frequency number ($1 \leq f \leq F$)
t	Time number
$e_{f,t}$	Spectral-temporal error
$\mathbf{S}$	Sensitivity matrix
opt	Symbol of optimal value
*	Symbol of ratiometric value
$<\cdot>$	Symbol of average value

5.2. Method

5.2.1. Frequency-difference adjacent EIT (*fda*-EIT)

In classical frequency-difference EIT (*fd*-EIT), the normalized perturbation between raw impedances $\mathbf{Z}$ at one frequency and a reference frequency is used to reconstruct conductivity image $\boldsymbol{\sigma}$. *fd*-EIT image may be deteriorated in the case of high conductivity contrast ($\mu >$ ±20%) due to the decreased accuracy of the linear approximation of the inverse problem in the nonlinear forward model [11], [12]. This linear assumption yields an acceptable *fd*-EIT image only in the cases where μ is less than 20% or where perturbations greater than this exist in a homogeneous background. To address this issue, frequency-difference adjacent EIT (*fda*-EIT) is alternatively used [13], in which the normalized perturbation between raw impedance $\mathbf{Z}$ at the f-th and the adjacent (f+1)-th frequencies is used to reconstruct the classical conductivity image $\boldsymbol{\sigma} \in \mathbb{R}^N$

$$\boldsymbol{\sigma} = \Lambda\left(\frac{\mathbf{Z}_{f+1} - \mathbf{Z}_f}{\mathbf{Z}_f}\right) \in \mathbb{R}^N \tag{5.1}$$

where N is the spatial resolution ($1 \leq n \leq N$) and Λ is the inverse operator to reconstruct $\boldsymbol{\sigma}$. Here the division is performed element-wise. The countermeasure against high μ condition in *fda*-EIT may not be sufficient yet, and furthermore, the distinguishability usually deteriorates as μ becomes lower. *fda*-EIT is used as a classical method against the proposed method described in the next section.

5.2.2. Ratiometric preprocessing and newly derived ratiometric EIT

The framework of "ratiometric" methods uses the ratio of two measurement signals and is widely applied in fluorescence methods [17], [18], and more recently in biometrics [19] because of its advantage of representing the phenomenon of anomaly better. Ratiometric impedance reduces measurement variability due to noise and amplifies inter-subject differences due to individual conductivity and anomaly size [19]. Thus, the framework is also beneficial to EIT as a preprocessing based on impedance measurement because distinguishability, characterized by noise, conductivity, anomaly size, and frequency-dependency [20], is considered to improve. However, it is not straightforwardly applied to the sensitivity-based EIT because the ideal image reconstruction is based on the impedance difference from the homogeneous condition. In other words, the sensitivity matrix $\mathbf{S}$ needs to be modified considering ratiometric impedance that varies greatly with each denominator. Hence, ratiometric impedance is averaged to enable its use. Taking the average of ratiometric impedance also has the advantage to high μ condition; the widely different scales of individual conductivities that determine impedance are considered to be balanced, which results in a minimized μ. This phenomenon is investigated in the numerical simulation and experiments.

Figure 5.1 shows the structure of newly derived ratiometric EIT which is composed of four steps to reconstruct the conductivity image. In Step 1, the ratiometric impedances [19] $^*\mathbf{Z} \in \mathbb{R}^{M \times F \times M}$ is generated from raw impedances $\mathbf{Z} \in \mathbb{R}^{M \times F}$, which is written by

$$\begin{aligned} \mathbf{Z} &= [\mathbf{Z}_1, ..., \mathbf{Z}_f, ..., \mathbf{Z}_F] \in \mathbb{R}^{M \times F} \\ \mathbf{Z}_f &= [z_{1,f}, ..., z_{m,f}, ..., z_{M,f}]^T \in \mathbb{R}^M \end{aligned} \tag{5.2}$$

$$\begin{aligned} ^*\mathbf{Z} &= [^*\mathbf{Z}_1, ..., ^*\mathbf{Z}_\xi, ..., ^*\mathbf{Z}_M] \in \mathbb{R}^{M \times F \times M} \\ ^*\mathbf{Z}_\xi &= [^*\mathbf{Z}_{1,\xi}, ..., ^*\mathbf{Z}_{f,\xi}, ..., ^*\mathbf{Z}_{F,\xi}] \in \mathbb{R}^{M \times F} \end{aligned} \tag{5.3}$$

$$
\begin{aligned}
{}^{*}\mathbf{Z}_{f,\xi} &= \left[{}^{*}z_{1,f,\xi}, \ldots, {}^{*}z_{m,f,\xi}, \ldots, {}^{*}z_{M,f,\xi} \right]^{T} \\
&= \left[\frac{z_{1,f}}{z_{\xi,f}}, \ldots, \frac{z_{m,f}}{z_{\xi,f}}, \ldots, \frac{z_{M,f}}{z_{\xi,f}} \right]^{T} \in \mathbb{R}^{M}
\end{aligned}
$$

where m ($1 \le m \le M$) is the m-th measurement number, f ($1 \le f \le F$) is the f-th frequency number, ξ ($1 \le \xi \le M$) is the selected measurement number as a denominator, * is the symbol of ratiometric value, and T is the transpose matrix.

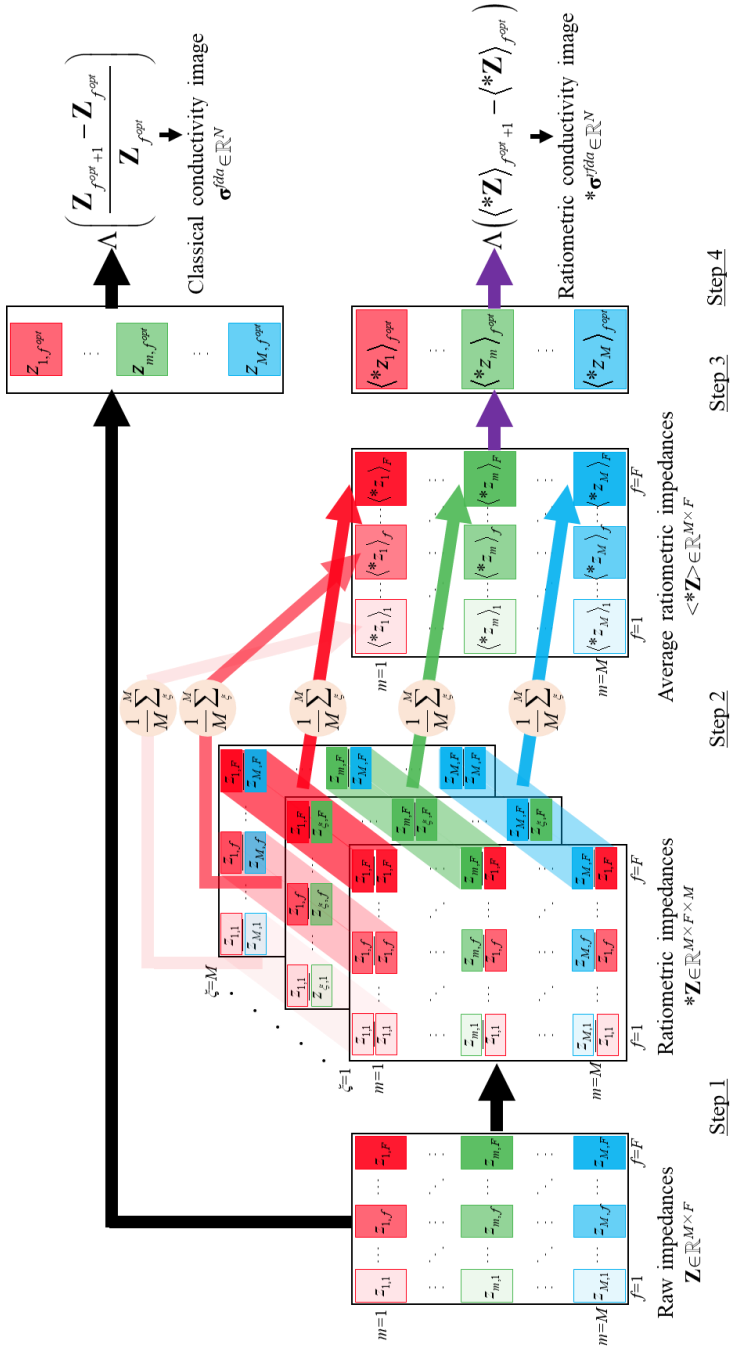

Figure 5.1. Structure of newly derived ratiometric EIT which is composed of four steps to reconstruct conductivity image σ.

In Step 2, the average ratiometric impedances $\langle *\mathbf{Z} \rangle \in \mathbb{R}^{M \times F}$ is generated from $*\mathbf{Z}$, which is written by

$$\begin{aligned} \langle *\mathbf{Z} \rangle &= \left[\langle *\mathbf{Z} \rangle_1, \ldots, \langle *\mathbf{Z} \rangle_f, \ldots, \langle *\mathbf{Z} \rangle_F \right] \in \mathbb{R}^{M \times F} \\ \langle *\mathbf{Z} \rangle_f &= \left[\langle *z_1 \rangle_f, \ldots, \langle *z_m \rangle_f, \ldots, \langle *z_M \rangle_f \right]^T \\ &= \left[\frac{1}{M} \sum_{\xi}^{M} \frac{z_{1,f}}{z_{\xi,f}}, \ldots, \frac{1}{M} \sum_{\xi}^{M} \frac{z_{m,f}}{z_{\xi,f}}, \ldots, \frac{1}{M} \sum_{\xi}^{M} \frac{z_{M,f}}{z_{\xi,f}} \right]^T \in \mathbb{R}^M \end{aligned} \tag{5.4}$$

In Step 3, the optimal frequency number f^{opt} and the optimal time number t^{opt} for the image reconstruction is selected based on the spectral-temporal error $e_{f,t}$ at the f-th frequency and the t-th time as follows

$$e_{f,t} = \sqrt{\frac{1}{M} \sum_{m}^{M} \left(\Delta *z_{m,f,t} - \Delta \hat{z}_{m,f,t} \right)^2} \tag{5.5}$$

where $\Delta *z_{m,f,t} = \langle *z_m \rangle_{f+1,t} - \langle *z_m \rangle_{f,t}$ is the perturbation of the m-th average ratiometric impedance $\langle *z_m \rangle_{f,t}$ at the f-th frequency and the t-th time, $\Delta \hat{z}_{m,f,t} = \mathbf{S}_m * \boldsymbol{\sigma}_{f,t}$ is the corresponding perturbation based on the forward problem, $\mathbf{S}_m \in \mathbb{R}^N$ is the m-th column vector of sensitivity matrix $\mathbf{S} \in \mathbb{R}^{M \times N}$, and $*\boldsymbol{\sigma}_{f,t} \in \mathbb{R}^N$ is the ratiometric conductivity image. The f^{opt} and t^{opt} is then selected as the one that minimizes $e_{f,t}$ as shown in **Figure 5.2**, which varies depending on the subject.

In Step 4, $\langle *\mathbf{Z} \rangle$ is processed in a derived ratiometric EIT, which is ratiometric frequency-difference adjacent EIT (*rfda*-EIT), in order to reconstruct the ratiometric conductivity image $*\boldsymbol{\sigma} \in \mathbb{R}^N$

$$\begin{aligned} *\boldsymbol{\sigma} &= \left[*\sigma_1, \ldots, *\sigma_n, \ldots, *\sigma_N \right]^T \\ &= \Lambda \left(\langle *\mathbf{Z} \rangle_{f^{opt}+1, t^{opt}} - \langle *\mathbf{Z} \rangle_{f^{opt}, t^{opt}} \right) \in \mathbb{R}^N \end{aligned} \tag{5.6}$$

The proposed method minimizes μ between anomaly and background while maintaining high distinguishability without any *a priori* information. After Step 1, $*\mathbf{Z}$ has more valid

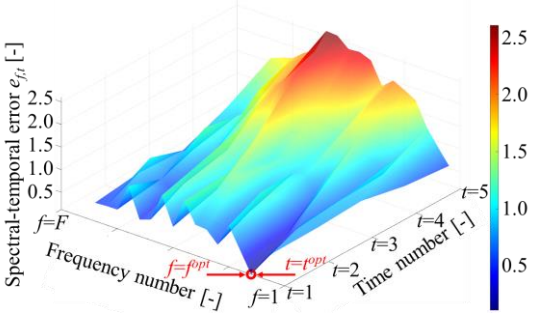

Figure 5.2. Spectral-temporal error $e_{f,t}$ for selection of optimal frequency number f^{opt} and optimal time number t^{opt} in the case where total time number is 5.

information unique to the individual physiological traits by reducing the skin-related parameters (e.g., skin temperature, inherent physiology) compared to **Z** [19]. Despite the advantage, μ is still variant due to the nonlinearity and probably high on particular $^*\mathbf{Z}$ depending on each selected measurement number ξ as a denominator. Therefore, in Step 2, the spatial variances of μ are mitigated by averaging with respect to M, which generates $<^*\mathbf{Z}>$. It is experimentally found that the error due to the contact impedance variances is mitigated as a secondary effect in Step 2. In Step 3, the optimal frequency number f^{opt} and the optimal time number t^{opt} for the image reconstruction is selected based on the accuracy of the linear approximation of the inverse problem in the nonlinear forward model. In Step 4, the perturbation at the t^{opt}-th time between $<^*\mathbf{Z}>$ at the (f^{opt}+1)-th and f^{opt}-th frequencies is reconstructed in *rfda*-EIT.

5.2.3. Image reconstruction

The inverse operator Λ in the case of *rfda*-EIT is written by

$$\begin{aligned} {}^*\boldsymbol{\sigma} &= \Lambda\left(\langle {}^*\mathbf{Z}\rangle_{f^{opt}+1} - \langle {}^*\mathbf{Z}\rangle_{f^{opt}}\right) \\ &= \frac{1}{2}\arg\min_{{}^*\boldsymbol{\sigma}}\left[\left\|\left(\langle {}^*\mathbf{Z}\rangle_{f^{opt}+1} - \langle {}^*\mathbf{Z}\rangle_{f^{opt}}\right) - \mathbf{S}{}^*\boldsymbol{\sigma}\right\|^2 + \lambda\left\|\mathbf{L}{}^*\boldsymbol{\sigma}\right\|^2\right] \end{aligned} \tag{5.7}$$

where $\mathbf{S}=[\mathbf{S}1,\ldots,\mathbf{S}m,\ldots,\mathbf{S}M]^T\in\mathbb{R}^{M\times N}$ is the sensitivity matrix under the homogeneous condition [21], $\mathbf{S}m=[S1,\ldots,Sn,\ldots,SN]\in\mathbb{R}^N$ is a column vector of $\mathbf{S}$, λ is the hyperparameter, and $\mathbf{L}\in\mathbb{R}^{N\times N}$ is the regularization matrix. Equation (5.7) is solved by the one-step Gauss-Newton algorithm because it is the most often used solver for the biomedical EIT due to its robustness to noise and low computational cost [22]. It is computed with the Tikhonov regularization [23]

$$\boldsymbol{\sigma}^{it+1} = \boldsymbol{\sigma}^{it} + [\mathbf{S}^T\mathbf{S} + \lambda\cdot\mathrm{diag}(\mathbf{L}^T\mathbf{L})]^{-1}\mathbf{S}^T[(\langle {}^*\mathbf{Z}\rangle_f - \langle {}^*\mathbf{Z}\rangle_1) - \mathbf{S}\boldsymbol{\sigma}^{it}] \tag{5.8}$$

where $\boldsymbol{\sigma}^{it}$ is the conductivity image at the it-th iteration step and diag(·) is the diagonal matrix.

5.3. Numerical simulation

5.3.1. Definition of conductivity contrast μ

Figure 5.3 shows an example of human calf compartments and corresponding conductivity values which have a diversified spectrum over frequency. The calf compartments comprise seven compartments, as shown in **Figure 5.3(a)**; SAT (Ω^{SAT}), muscle (Ω^{mu}), bone cortical (Ω^{bc}), bone marrow (Ω^{bm}). Each compartment has a various relationship with frequency, as shown in **Figure 5.3(b)** (adapted from [10]), which provides structural information about changes in physiological conditions via frequency-difference EIT (*fd*-EIT)

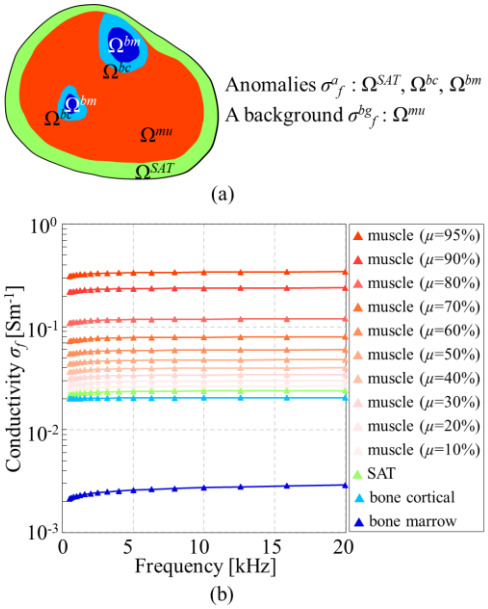

Figure 5.3. (a) Typical compartments of human right calf on axial-plane. (b) Conductivity values under variant conditions of conductivity contrasts μ (= 95%-10%) at a frequency range between 500Hz-20kHz. †Raw values in (b) are adapted from [10].

[9]. The conductivity value σ_f on each compartment Ω parameterizes the raw impedance $z_{m,f}$ variously depending on Ω by the nonlinear transformation $\sigma_f \rightarrow z_{m,f}$ on the boundary $\partial\Omega$. In this study, σ_f in Ω^{SAT}, Ω^{bc}, and Ω^{bm} are considered as anomalies $\sigma^a_f \approx \chi^a_f(\Omega^{SAT}, \Omega^{bc}, \Omega^{bm})$; in contrast, σ_f in Ω^{mu} is regarded as a background $\sigma^{bg}_f \approx \chi^{bg}_f(\Omega^{mu})$. Here χ^a_f and χ^{bg}_f denote the characteristic function to specify σ_f in the FEM mesh of the anomalies and background, respectively, in order to define the conductivity contrast μ

$$\mu = \frac{\sigma^a_f - \sigma^{bg}_f}{\sigma^{bg}_f} \times 100\ [\%] \tag{5.9}$$

based on their relationship: $\sigma^{SAT}, \sigma^{bc}, \sigma^{bm} << \sigma^{mu}$. μ is approximately 95% in the case of raw values. Skin conductivity σ^{sk} is assumed to be disregarded in the simplified equivalent circuit model since skin-related parameters (e.g., skin temperature, inherent physiology) can be minimized by ratiometric preprocessing [19].

5.3.2. Numerical simulation condition

The sensitivity matrix **S** in Equation (5.8) is computed under the homogeneous condition [21], i.e., $\boldsymbol{\sigma}^{it=0}$=1.0[Sm^{-1}]. The hyperparameter λ and iteration number N^{it} are set to λ=0.01 and N^{it}=5 for both methods, respectively. Only $\boldsymbol{\sigma}$ at the optimal time number t^{opt}=1 is considered in the numerical simulation under a noise-free environment. The $\boldsymbol{\sigma}$ is clustered based on the

fuzzy *k*-means algorithm [24] in order to evaluate each reconstruction performance by four metrics which are 1) the area ratio error ARE^{SAT} of SAT, 2) the position error PE^{tibia} of bone tibia, 3) the position error PE^{fibula} of bone fibula, and 4) the correlation coefficient *CC*

$$ARE^{SAT} = \left| \frac{AR^{SAT} - AR_{true}^{SAT}}{AR_{true}^{SAT}} \right| \times 100\ [\%] \tag{5.10}$$

$$PE^{tibia} = \left| \frac{r^{tibia} - r_{true}^{tibia}}{r_{true}^{tibia}} \right| \times 100\ [\%] \tag{5.11}$$

$$PE^{fibula} = \left| \frac{r^{fibula} - r_{true}^{fibula}}{r_{true}^{fibula}} \right| \times 100\ [\%] \tag{5.12}$$

$$CC = \frac{\sum_{n=1}^{N} (\sigma_n - \bar{\sigma})(\sigma_n^{true} - \overline{\sigma^{true}})}{\sqrt{\sum_{n=1}^{N} (\sigma_n - \bar{\sigma})^2 (\sigma_n^{true} - \overline{\sigma^{true}})^2}} \tag{5.13}$$

where $AR^{SAT} = A^{SAT}/A_0$, A^{SAT} is the area of SAT, A_0 is the total area of images, r^{tibia} and r^{fibula} is the distance between the origin O and the center of gravity of bone tibia and bone fibula, respectively, n is spatial resolution ($1 \le n \le N$), σ_n is the reconstructed conductivity, and $\bar{\sigma}$ is the spatial mean conductivity, respectively. The subscripts and superscripts *true* indicate the true value of each metric. In ideal conditions where the ratio between $\boldsymbol{\sigma}$ and the true conductivity image $\boldsymbol{\sigma}^{true}$ is equal to phantom conditions, the value of ARE^{SAT}, PE^{tibia}, ARE^{fibula} are 0% and *CC* is 1.

The raw impedances $\mathbf{Z}$ is calculated with a current I_0 = 1mA by MATLAB R2020a (Mathworks, Natick, MA) and EIDORS [25]. Fig. 4 shows the FEM mesh of the calf phantom under the homogeneous condition generated by NETGEN [26]. The data acquisition system of the quasi-adjacent pattern [27] is composed of four ports: H_C (high-current), H_P (high-potential), L_C (low-current), and L_P (low-potential), in which H_C-H_P and L_C-L_P pairs are adjacents, respectively. For instance, in the case of a particular measurement number (m = 107), H_C, H_P, L_C, and L_P correspond to electrodes e_{13}, e_{12}, e_8, and e_9, respectively, as shown in **Figure 5.4.**

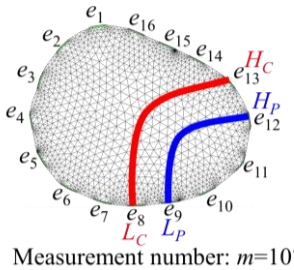

Figure 5.4. FEM mesh of calf phantom under homogeneous condition in quasi-adjacent pattern with illustrative stimulus current flow (red line) and measurement current flow if measurement electrodes are used as stimulus (blue line) in the case of a particular measurement number (m=107).

The human calf compartments in **Figure 5.3(a)** are discretized in order to configure the calf phantom, in which the muscle conductivity σ^{mu} is changed in order to simulate the variant conditions of conductivity contrasts μ (= 95%-10%). This variant condition covers μ=95%, which is typical for the human body [10], and μ=20%, which is reported to guarantee the accuracy of linear approximation in the inverse problem [11], [12]. **Figure 5.3(b)** shows the conductivity values used in the numerical simulation at a frequency range between 500Hz-20kHz [10], which is the same as the experimental condition.

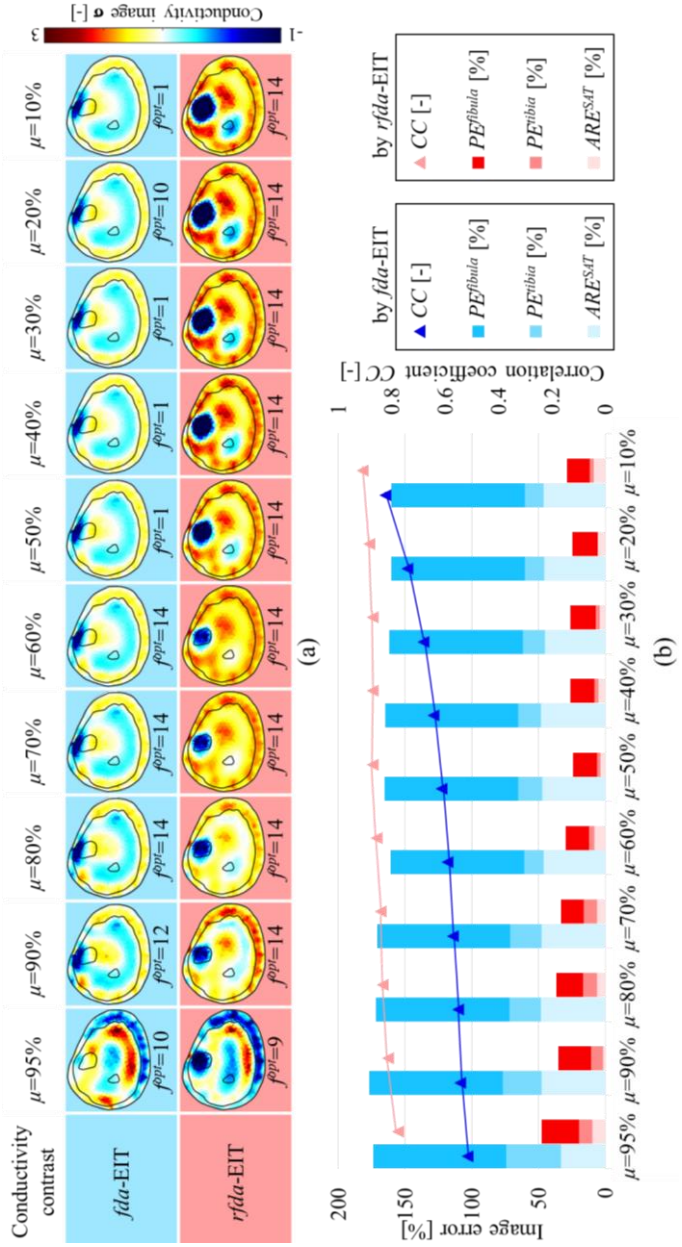

Figure 5.5. Conductivity image σ of numerical simulation by classical EIT (*fda*-EIT) and ratiometric EIT (*rfda*-EIT) under the variant conditions of conductivity contrasts μ (= 95%-10%) (a). Area ratio error ARE^{SAT} of SAT, position error PE^{tibia} of bone tibia, PE^{fibula} of bone fibula, and correlation coefficient *CC* of each algorithm (b).

5.3.3. Results of numerical simulation

Figure 5.5(a) shows the conductivity image **σ** reconstructed at the optimal frequency number f^{opt} by classical EIT (*fda*-EIT) and ratiometric EIT (*rfda*-EIT) under the variant conditions of μ. **Figure 5.5(b)** shows ARE^{SAT}, PE^{tibia}, PE^{fibula}, and *CC* of each algorithm. *fda*-EIT fails to detect bone tibia position correctly and overestimates SAT thickness. Even though *CC* increases with the increased μ in *fda*-EIT, *CC* is lower than that in *rfda*-EIT as a whole. On the other hand, in *rfda*-EIT, even though the compartments are better distinguished as μ decreases, ***σ** successfully showed SAT, muscle, and bone tibia in all the cases. The bone fibula is correctly detected in *rfda*-EIT, which cannot be detected by *fda*-EIT at all. The high value of *CC* and low value of ARE^{SAT}, PE^{tibia}, and PE^{fibula} in **Figure 5.5(b)** confirms that *rfda*-EIT has a high reconstruction performance capability under the variant conditions of μ.

5.4. Experiments

5.4.1. Experimental setup, method, and conditions

Figure 5.6(a) shows the EIT experimental setup composed of four units: a) a wearable sensor [28], b) an impedance analyzer (IM3570, HIOKI, Japan), c) a digital multiplexer [29] (made by Takei lab based on Arduino Due), and d) a PC including image reconstruction algorithm software.

The a) wearable sensor consists of sixteen silver yarn rectangular electrodes (5 × 10 mm) [30]. The number of electrodes was empirically chosen based on the signal-noise ratio (SNR), which depends on the trade-off between the size and number of electrodes [31]. These electrodes are shielded by thermoplastic polyurethane as a countermeasure for the high contact impedance [32] and are attached to flexible polyester clothe. The b) impedance

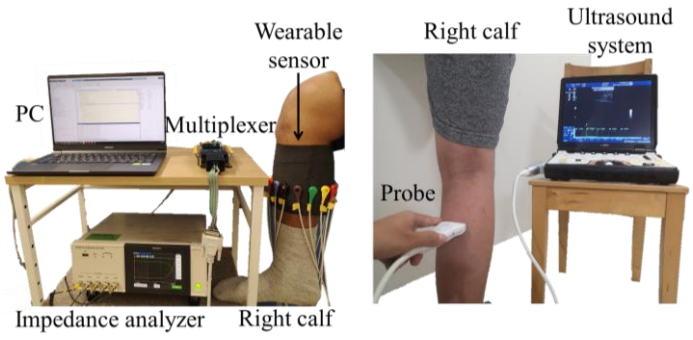

(a) **(b)**

Figure 5.6. Experimental setup of EIT measurement (a) and ultrasound measurement (b).

analyzer was connected to a digital multiplexer by four ports: *Hc*, *Hp*, *Lc*, and *Lp*. The c) digital multiplexer was connected to the wearable sensor by coaxial cables. The raw impedances **Z** from the impedance analyzer was sent to the PC by a USB cable. The d) PC computes both the forward and inverse problems by NETGEN and EIDORS supported by MATLAB R2020a.

The raw impedances **Z** is measured by the impedance analyzer with a current I_0 = 1mA and a frequency range between 500Hz-20kHz, which is selected to achieve the best SNR in our EIT system [33]. A derived ratiometric EIT, which is *rfda*-EIT, is compared to a classical EIT, which is *fda*-EIT. In order to achieve better image interpretation, the conductivity image **σ** is clustered based on fuzzy *k*-means algorithm [24] and each cluster is filtered by the Gaussian method. The **Z** was continuously measured for 30 minutes in order to attain the reliability of the experiment.

Eight healthy subjects (age: 27.5 ± 4.3 years, body mass index: 23.2 ± 4.2 kg/m^2) were volunteered in this study in accordance with the ethical guidelines of the Bioethics Committee in Faculty of Engineering, Chiba University, Japan, and all voluntary subjects gave informed consent. All of the subjects were sitting while their thighs and calves formed a 90-degree angle. This sitting position was arranged to avoid the change of water volume in the human calf due to edema caused by the gravity effect during the measurement [30].

5.4.2. Evaluation of reconstructed images

In order to investigate for the best reconstruction performance of subjects' calves compartments, correct images are obtained by an ultrasound examination [34] with a high-frequency matrix probe (LOGIQ e Premium, GE Healthcare, Japan) on the axial plane as shown in **Figure 6(b)**. Using the slight trace made by the electrodes after the EIT measurement as a landmark, ultrasound scans were acquired with special attention at each landmark while the probe was rotated horizontally 360° along the circumference of the subject's calf. The acquired scans were transformed into one image by manually connecting anatomical landmarks (e.g., veins, crossing of aponeuroses) in each pair of adjacent scans, which is considered a correct image. Reconstructed image analyses are based on area ratio error ARE^{SAT} of SAT and true positive rate TPR^{tibia} for the bone tibia detection. The ARE^{SAT} is calculated using Equation (10). The TPR^{tibia} is calculated as follows [35]

$$TPR^{tibia} = TP^{tibia} \Big/ \left(TP^{tibia} + FN^{tibia} \right) \times 100 \ [\%] \tag{5.14}$$

where TP^{tibia} and FN^{tibia} represent the true positives and false negatives, which are determined by heuristic observation compared to the correct images obtained by the ultrasound examination. Namely, if the bone tibia of each subject detected in ***σ** matches each ultrasound image, it is counted as a true positive. The heuristic observation is conducted by the same person to avoid inter-observer variability.

5.4.3. Experimental results of ratiometric spectra

Figure 5.7 shows five representative time-variable spectra of the raw impedances **Z** and the average ratiometric impedances <***Z**> in eight subjects at the measurement time t=1(=0s), t=2(=360s), t=3(=720s), t=4(=1,080s), t=5(=1,440s) in the case of particular measurement number (m=107) shown in **Figure 5.3**. In **Figure 5.7**, the difference in the time-variable spectra depending on t, which can be attributed to the slight movement of the electrodes, occurs in both **Z** and <***Z**>; however, the difference in <***Z**> is visually more emphasized by the normalization. More importantly, the time-variable spectra of **Z** are monotonously decreased over frequency and do not show any difference in tendency between subjects. In contrast, the time-variable spectra of <***Z**> are irregularly changed over frequency and show

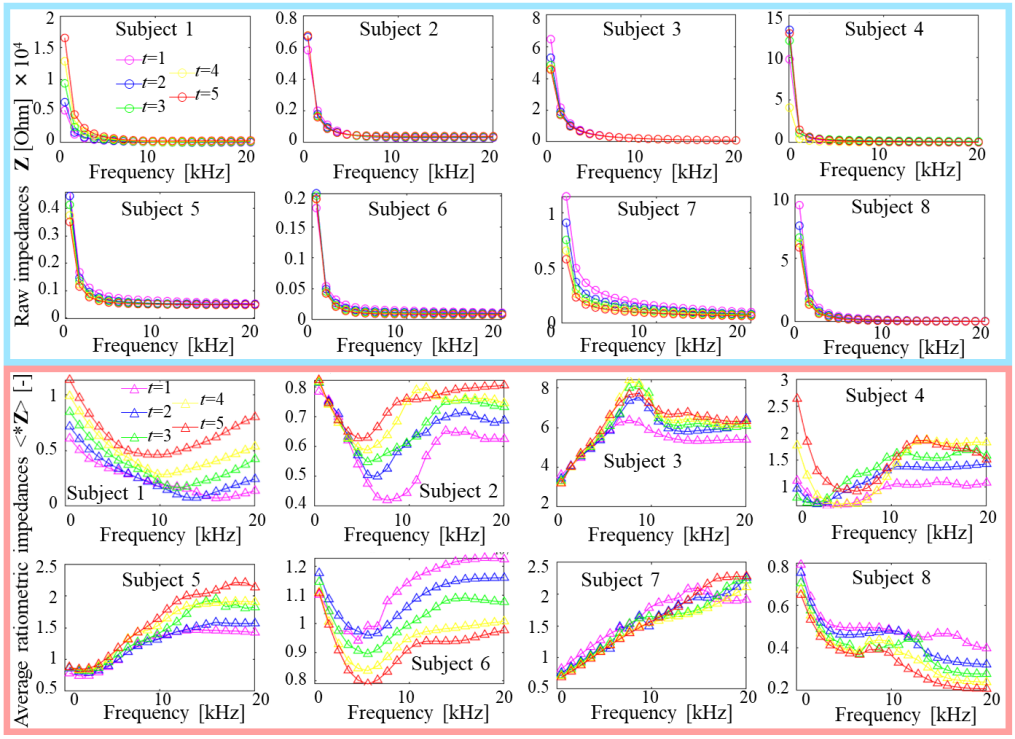

Figure 5.7. Time-variable spectra of raw impedances Z (–○–) and average ratiometric impedances <*Z> (–△–) of eight subjects at the measurement time t=1(=0s), t=2(=360s), t=3(=720s), t=4(=1,080s), t=5(=1,440s) in the case of measurement number (m=107).

diverse trends between subjects. This diversity in the time-variable spectra of <***Z**> makes the differences between subjects with various compartments more prominent than **Z**.

5.4.4. Experimental results of image reconstruction

Figure 5.8 shows the conductivity image **σ** reconstructed at the optimal frequency number f^{opt} and the optimal time number t^{opt} by classical EIT (*fda*-EIT) and ratiometric EIT (*rfda*-EIT) in eight subjects' calves. The 2nd row shows the examples of scanned ultrasound images of subjects' calves used as correct images and the 3rd and 4th rows represent comparisons of **σ** among the subjects. Dashed lines are manually drawn, indicating the outer line of the bone tibia (red) and the expected bone fibula (black), respectively. Only structurally imaged compartments are marked with dashed lines, and those for the bone tibia are counted as positive. Overall, *rfda*-EIT images the bone tibias and SAT thickness more accurately than *fda*-EIT. It is worth noting that *rfda*-EIT images the perturbations due to bone fibula's presence in most subjects, which cannot be detected by the ultrasound. **Figure 5.9** shows the area ratio error ARE^{SAT} of SAT. The ARE^{SAT} is smaller by *rfda*-EIT in all the subjects as

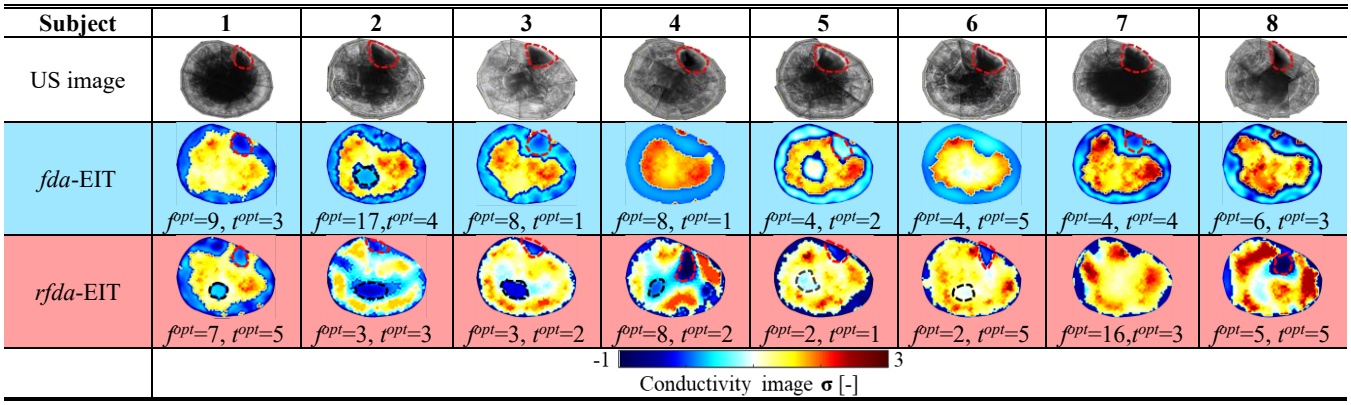

Figure 5.8. Conductivity image σ of eight subjects by classical EIT (*fda*-EIT) and ratiometric EIT (*rfda*-EIT). Dashed lines indicate the outer line of the bone tibia (red) and the expected bone fibula (black), respectively.

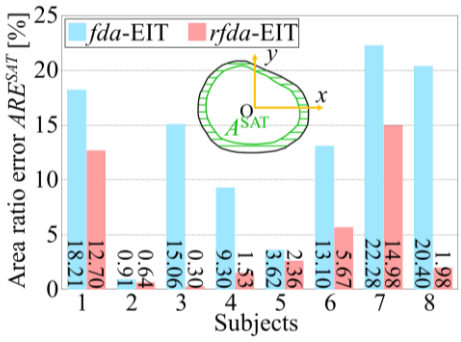

Figure 5.9. Area ratio error ARE^{SAT} in conductivity image **σ** of eight subjects by classical EIT (*fda*-EIT) and ratiometric EIT (*rfda*-EIT).

TABLE 5.3

TRUE POSITIVE RATE TPR^{tibia} FOR BONE TIBIA DETECTION IN CONDUCTIVITY IMAGE $\boldsymbol{\sigma}$ OF EIGHT SUBJECTS BY CLASSICAL EIT (*fda*-EIT) AND RATIOMETRIC EIT.

Method	True positive rate TPR^{tibia}
fda-EIT	50.0%
rfda-EIT	87.5%

compared to *fda*-EIT. The total-mean ARE^{SAT}, $\langle ARE^{SAT} \rangle$ is 5.18% and 12.70% by *rfda*-EIT and *fda*-EIT, respectively, which indicates *rfda*-EIT images SAT better than *fda*-EIT. **Table 5.3** shows TPR^{tibia} of the two methods determined by heuristic observation compared to the correct images from the ultrasound examination. The TPR^{tibia} is 87.5% and 50.0% by *rfda*-EIT and *fda*-EIT, respectively, which indicates *rfda*-EIT is more plausible than *fda*-EIT for the bone tibia detection. In summary, the $\boldsymbol{\sigma}$ by *rfda*-EIT are in good agreement with the ultrasound images with the aid of the minimized μ and improved distinguishability in $\langle *\mathbf{Z} \rangle$.

5.5. Discussions

5.5.1. Distinguishability in ratiometric preprocessing

As shown in **Figure 5.5** and **5.8**, ratiometric preprocessing increases the reconstruction performance by decreasing the conductivity contrast μ, which seems to decrease the distinguishability; therefore, the influence of the ratiometric preprocessing on the distinguishability is investigated by the finite precision measurements.

5.5.1.1. Assumptions and Conditions

Three cases are considered to discuss the distinguishability in calf compartments by the three geometric arrangements of background conductivity $\sigma^{bg}{}_f$ and anomaly conductivity $\sigma^{a}{}_f$ as shown in **Figure 5.10**, which are

1) background conductivity image ${}^0\boldsymbol{\sigma}_f$ filled only by $\sigma^{bg}{}_f = \sigma^{muscle}{}_f$ under the radius R^{muscle}=1,

2) bone anomaly conductivity image ${}^1\boldsymbol{\sigma}_f$ filled by $\sigma^{a}{}_f = \sigma^{bone}{}_f$ under the radius R^{bone} and $\sigma^{bg}{}_f = \sigma^{muscle}{}_f$ under the radius R^{muscle}=1,

3) fat anomaly conductivity image ${}^2\boldsymbol{\sigma}_f$ filled by $\sigma^{bg}{}_f = \sigma^{muscle}{}_f$ under the radius R^{muscle} and $\sigma^{a}{}_f = \sigma^{fat}{}_f$ under the radius R^{fat}=1.

The analysis of impedance difference in *td*-EIT is assumed to be applicable to *fd*-EIT given the analogy between the two methods [36]. Here ratiometric EIT (*rfda*-EIT) and

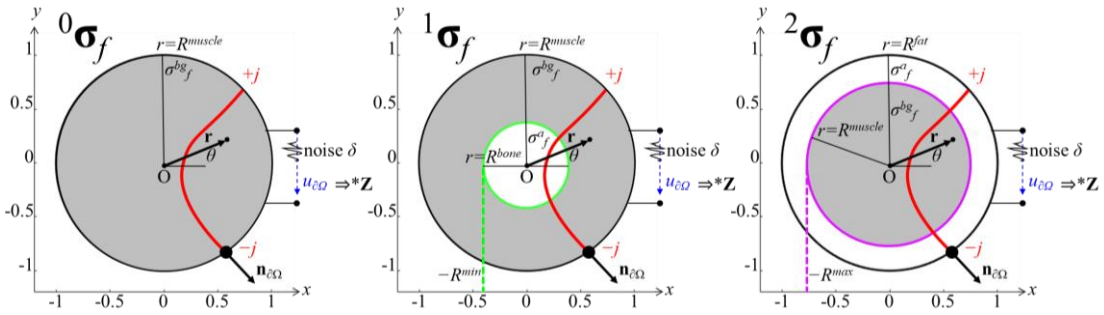

Figure 5.10. Three geometric arrangements of background conductivity σ^{bg}_f and anomaly conductivity σ^{a}_f : (a) Background conductivity image ${}^0\boldsymbol{\sigma}_f$, (b) Bone anomaly conductivity image ${}^1\boldsymbol{\sigma}_f$, and (c) fat anomaly conductivity image ${}^2\boldsymbol{\sigma}_f$.

classical EIT (*fda*-EIT) are considered. The conductivity $\sigma(\mathbf{r},f)$ for ${}^0\boldsymbol{\sigma}_f$, ${}^1\boldsymbol{\sigma}_f$, and ${}^2\boldsymbol{\sigma}_f$ are represented by ratiometric EIT as follows

$$
\begin{aligned}
{}^0\sigma(\mathbf{r},f) &= 1, \text{ for } r<1 \\
{}^1\sigma(\mathbf{r},f) &= \begin{cases} \mu_f, \text{ for } r < R^{bone} \\ 1 \ , \text{ for } R^{bone} < r < 1 \end{cases} \\
{}^2\sigma(\mathbf{r},f) &= \begin{cases} 1 \ , \text{ for } r < R^{muscle} \\ \mu_f, \text{ for } R^{muscle} < r < 1 \end{cases}
\end{aligned}
\qquad (5.15)
$$

where $\mathbf{r} = (x,y)$ is the position vector from origin O with the polar coordinates $x = r\cos\theta$ and $y = r\sin\theta$. $\sigma(\mathbf{r},f)$ are assumed to be characterized by the conductivity contrast $\mu = (\sigma^a_f - \sigma^{bg}_f)/\sigma^{bg}_f$ and the homogeneous background, respectively. On the other hand, Equation (15) is represented by classical EIT as follows

$$
\begin{aligned}
{}^0\sigma(\mathbf{r},f) &= \sigma^{bg}_f, \text{ for } r<1 \\
{}^1\sigma(\mathbf{r},f) &= \begin{cases} \sigma^{a}_f \ , \text{ for } r < R^{bone} \\ \sigma^{bg}_f, \text{ for } R^{bone} < r < 1 \end{cases} \\
{}^2\sigma(\mathbf{r},f) &= \begin{cases} \sigma^{bg}_f \ , \text{ for } r < R^{muscle} \\ \sigma^{a}_f \ , \text{ for } R^{muscle} < r < 1 \end{cases}
\end{aligned}
\qquad (5.16)
$$

Since the heterogeneous background is considered, σ^{bg}_f changes depending on the location, i.e., $\sigma^{bg}_f \neq$ const. in Equation (16). Whether ${}^1\boldsymbol{\sigma}_f$ and ${}^2\boldsymbol{\sigma}_f$ are distinguishable from ${}^0\boldsymbol{\sigma}_f$ is determined by voltages $\mathbf{V}_f$ on the boundary $\partial\Omega$ which are configured by voltage $u_{\partial\Omega}$.

5.5.1.2. Solution of Laplace equation

Two cases of impedance difference are investigated, which are

1) bone-muscle impedance difference between ${}^1\boldsymbol{\sigma}_f$ and ${}^0\boldsymbol{\sigma}_f$,

2) fat-muscle impedance difference between ${}^2\boldsymbol{\sigma}_f$ and ${}^0\boldsymbol{\sigma}_f$.

Let $\mathbf{J}$ be the current density vector which formulates $\mathbf{J}\cdot\mathbf{n}_{\partial\Omega} = j$ with the outward unit

normal vector $\mathbf{n}_{\partial\Omega}$ and the current density j on $\partial\Omega$. Considering the linear relationship between the raw impedances $\mathbf{Z}_f$ and $\mathbf{V}_f$ in Ohm's law, anomaly conductivity is distinguishable [20] by using the ratiometric impedances $^*\mathbf{Z}_{f,\xi}$ with selected measurement number ξ as a denominator

$$\begin{aligned}\left\| {}^*\mathbf{Z}_\xi({}^1\boldsymbol{\sigma}_f) - {}^*\mathbf{Z}_\xi({}^0\boldsymbol{\sigma}_f) \right\|_{1/2} &= \frac{2|\beta|(R^{bone})^2}{1+\beta(R^{bone})^2} > \delta \\ \left\| {}^*\mathbf{Z}_\xi({}^2\boldsymbol{\sigma}_f) - {}^*\mathbf{Z}_\xi({}^0\boldsymbol{\sigma}_f) \right\|_{1/2} &= 1 - \frac{1+\beta(R^{muscle})^2}{\mu_f[1-\beta(R^{muscle})^2]} > \delta\end{aligned} \tag{5.17}$$

where $\beta = (\mu-1)/(\mu+1)$ and δ is the noise on the circular measurement system. Equation (5.17) is derived based on the fact that the voltage u satisfies Laplace equation and Neumann boundary condition, which is written by

$$\nabla \cdot \sigma \nabla u = 0 \tag{5.18}$$

$$j = \sigma \nabla u \cdot \mathbf{n}_{\partial\Omega} \tag{5.19}$$

Firstly, u is obtained by solving Laplace equation (Equation (5.18)) under the assumptions of σ. Secondly, j is obtained by substituting u into Equation (5.19). Consequently, Equation (5.17) is obtained (See Appendix for the derivation of the solution).

5.5.1.3. Definition of Distinguishable Region E

Two cases of the impedance difference are considered to define distinguishable region E which are derived from Equation (5.17) with three parameters: σ^a_f, R^{bone}, and R^{muscle}. E has two solution regions, i.e., the upper region E^{up} and the lower region E^{low}, where E^{up} is above the upper threshold $\sigma^{up}_f(R^{bone})$ or $\sigma^{up}_f(R^{muscle})$ and E^{low} is below the lower threshold $\sigma^{low}_f(R^{bone})$ or $\sigma^{low}_f(R^{muscle})$

$$\begin{aligned}&E = E^{up} + E^{low} \\ &E^{up}({}^1\boldsymbol{\sigma}_f, {}^0\boldsymbol{\sigma}_f) \equiv \left\{ \sigma^a_f \geq \sigma^{up}_f(R^{bone}), \text{ and } 0 \leq R^{bone} \leq 1 \right\} \\ &E^{low}({}^1\boldsymbol{\sigma}_f, {}^0\boldsymbol{\sigma}_f) \equiv \left\{ \sigma^a_f \leq \sigma^{low}_f(R^{bone}), \text{ and } 0 \leq R^{bone} \leq 1 \right\} \\ &E^{up}({}^2\boldsymbol{\sigma}_f, {}^0\boldsymbol{\sigma}_f) \equiv \left\{ \sigma^a_f \geq \sigma^{up}_f(R^{muscle}), \text{ and } 0 \leq R^{muscle} \leq 1 \right\} \\ &E^{low}({}^2\boldsymbol{\sigma}_f, {}^0\boldsymbol{\sigma}_f) \equiv \left\{ \sigma^a_f \leq \sigma^{low}_f(R^{muscle}), \text{ and } 0 \leq R^{muscle} \leq 1 \right\}\end{aligned} \tag{5.20}$$

where

$$\sigma^{up}_f(R^{bone}) = 1 + \frac{\frac{2\delta}{2-\delta}}{\left[(R^{bone})^2 - \frac{\delta}{2-\delta}\right]}$$

$$\sigma^{low}_f(R^{bone}) = 1 - \frac{\frac{2\delta}{2+\delta}}{\left[(R^{bone})^2 + \frac{\delta}{2+\delta}\right]}$$

$$\sigma_f^{up}(R^{muscle}) = -\frac{\delta + \delta(R^{muscle})^2 + \sqrt{A}}{2[\delta - \delta(R^{muscle})^2 + (R^{muscle})^2 - 1]}$$

$$\sigma_f^{low}(R^{muscle}) = -\frac{\delta + \delta(R^{muscle})^2 - \sqrt{A}}{2[\delta - \delta(R^{muscle})^2 + (R^{muscle})^2 - 1]}$$

$$A = \delta^2(R^{muscle})^4 + 2\delta^2(R^{muscle})^2 + \delta^2 - 4\delta(R^{muscle})^4 + 8\delta(R^{muscle})^2 - 4\delta + 4(R^{muscle})^4 - 8(R^{muscle})^2 + 4$$

Here the values from **Figure 5.3** are substituted into $\sigma^{bg}{}_f$ in order to calculate $\sigma^a{}_f = \sigma^{bg}{}_f(\mu + 1)$ with the noise level $\delta = 0.3$. For better representation, E by classical EIT with $\sigma^{bg}{}_f = 1$ is also considered.

Moreover, changes of distinguishable regions ΔE^{up} and ΔE^{low} over frequency by ratiometric EIT as compared to classical EIT are considered for the two cases of the impedance difference which are calculated as follows

$$\Delta E^{up} = \frac{{}^*E^{up} - E^{up}}{E^{up}} \times 100\ [\%] \tag{5.21}$$

where ${}^*E^{up}$ and E^{up} are calculated by using ratiometric EIT and classical EIT, respectively. The integral in the limited region $0 \leq \sigma^a{}_f \leq 2$ is calculated considering the natural representations of conductivity in calf compartments. ΔE^{low} is calculated in the same way as ΔE^{up}.

5.5.1.4. Results of Distinguishable Region E

Figure 5.11(a) and **(b)** show $E({}^1\boldsymbol{\sigma}_f, {}^0\boldsymbol{\sigma}_f)$ and $E({}^2\boldsymbol{\sigma}_f, {}^0\boldsymbol{\sigma}_f)$, respectively, by ratiometric EIT (horizontal shading) and classical EIT (vertical shading). Ratiometric EIT yields a remarkable increase in $E({}^1\boldsymbol{\sigma}_f, {}^0\boldsymbol{\sigma}_f)$ by decreasing $\sigma^{up}{}_f(R^{bone})$ and the minimum radius of R^{bone}, R^{min}, at which $\sigma^{bone}{}_f$ can be distinguished from $\sigma^{muscle}{}_f$. This indicates ratiometric EIT distinguishes smaller radius and smaller conductivity anomaly located in the center compared to classical EIT. Meanwhile, ratiometric EIT also yields a remarkable increase in $E({}^2\boldsymbol{\sigma}_f, {}^0\boldsymbol{\sigma}_f)$ by decreasing $\sigma^{up}{}_f(R^{muscle})$ and increasing $\sigma^{low}{}_f(R^{muscle})$, which increases the maximum radius of R^{muscle}, R^{max}, at which $\sigma^{fat}{}_f$ can be distinguished from $\sigma^{muscle}{}_f$. This indicates that ratiometric EIT distinguishes smaller conductivity anomaly located near the boundary, which cannot be distinguished by classical EIT at all.

In **Figure 5.11(c)**, $\Delta E^{up}({}^1\boldsymbol{\sigma}_f, {}^0\boldsymbol{\sigma}_f)$ and $\Delta E^{low}({}^1\boldsymbol{\sigma}_f, {}^0\boldsymbol{\sigma}_f)$ show downward and upward trend as frequency increases, respectively, which means that the distinguishability is affected by frequency dependency based on the relationship of $\sigma^a{}_f$ and $\sigma^{bg}{}_f$. Whereas, in **Figure 5.11(d)**, only $\Delta E^{up}({}^2\boldsymbol{\sigma}_f, {}^0\boldsymbol{\sigma}_f)$ is provided because $\sigma^{low}{}_f(R^{muscle})$ has negative values by classical EIT. $\Delta E^{up}({}^2\boldsymbol{\sigma}_f, {}^0\boldsymbol{\sigma}_f)$ shows a downward trend as frequency increases. These trends indicate that the

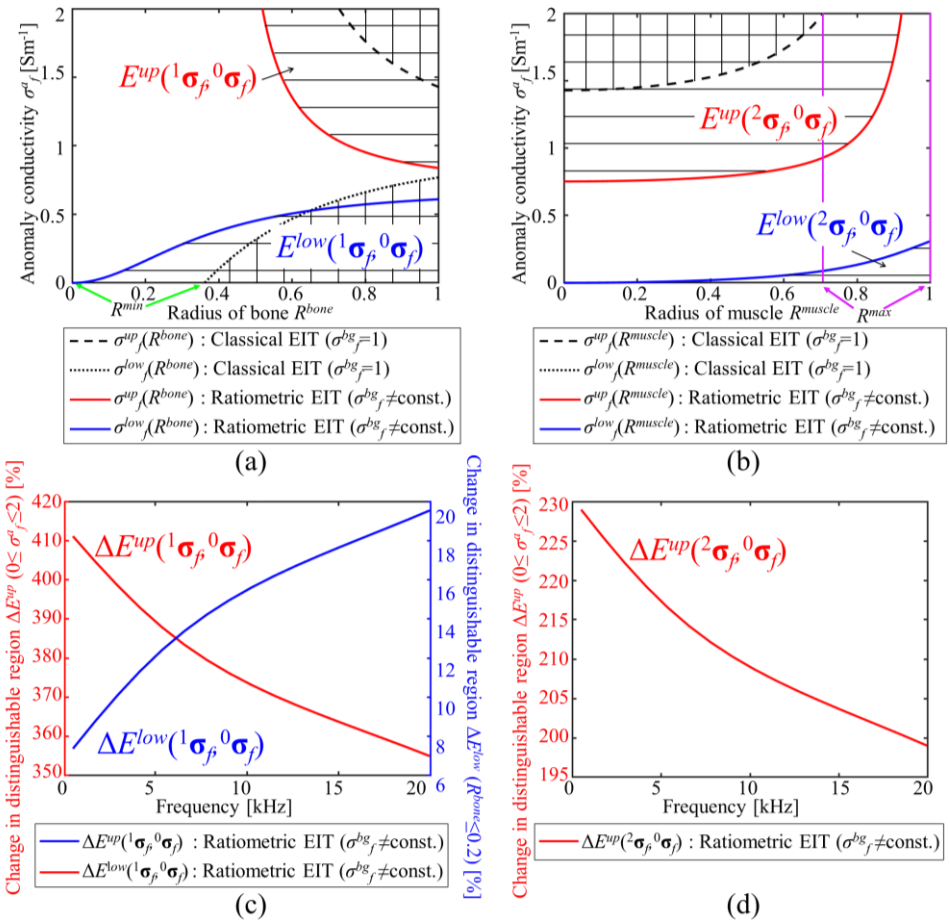

Figure 5.11. Distinguishable region (a) $E({}^1\sigma_f, {}^0\sigma_f)$ and (b) $E({}^2\sigma_f, {}^0\sigma_f)$ at frequency 500Hz with noise level δ = 0.3 by ratiometric EIT (horizontal shading) and classical EIT (vertical shading), respectively. Changes of distinguishable regions (c) $\Delta E^{up}({}^1\sigma_f, {}^0\sigma_f)$ and $\Delta E^{low}({}^1\sigma_f, {}^0\sigma_f)$ and (d) $\Delta E^{up}({}^2\sigma_f, {}^0\sigma_f)$ over frequency by ratiometric EIT as compared to classical EIT.

ratiometric conductivity image $^*\boldsymbol{\sigma}$ at higher frequency distinguish bone and fat better, whereas $^*\boldsymbol{\sigma}$ at lower frequency distinguish muscle better. In that way, ratiometric EIT increases the performance of calf compartments imaging by using multiple frequencies. Overall, the distinguishability is increased regardless of location while maintaining robustness to high μ in the heterogeneous background without any *a priori* information.

5.5.2. Conductivity contrast

EIT uses impedance perturbation to show the conductivity image $\boldsymbol{\sigma}$ of the anomaly. The numerical simulation results in the variant conditions of μ mostly agree with the results published earlier [11], [12]. It suggested that the accuracy of the linear approximation in EIT's inverse problem is seriously affected in the case of $\mu > \pm 20\%$. This condition is not usually achievable in biological applications given the wide range of conductivity values in each

compartment. Moreover, the human body is composed of a heterogeneous combination of tissues, which is generally frequency-dependence [15]. These facts are a huge problem in clinical practice since the compensative parameters cannot be incorporated as *a priori* information.

Furthermore, image reconstruction of multiple anomalies, such as human body compartments imaging, is generally challenging. The inverse problem gets even more problematic when several anomalies have various sizes because the larger anomalies are more dominant than the smaller anomalies on $\mathbf{Z}$ with widely varying scales [37]. Meanwhile, the ratiometric preprocessing extracts the influence of multiple anomalies simultaneously with the balanced scale due to the minimized μ and improved distinguishability in $^*\mathbf{Z}$. Even though other time-consuming approaches use *a priori* information, the configuration of $^*\mathbf{Z}$ is a trivial task that does not require any *a priori* information.

In summary, ratiometric EIT holds the valid internal information of each calf's compartments, as shown in **Figure 5.5** and **5.8** in order to acquire structural images by minimizing μ while maintaining high distinguishability. As a proof of concept, *rfda*-EIT showed good agreement with the ultrasound images in the experiment.

5.5.3. Singular spectrum

In order to demonstrate the influence of the improved distinguishability, singular value decomposition (SVD) is applied. The SVD-based analysis presents global measures about reconstruction performance. The SVD of a sensitivity matrix $\mathbf{S}$ is decomposed as

$$\mathbf{S} = \mathbf{Y} \sum \mathbf{V}^T \tag{5.22}$$

where $\mathbf{Y}=[\mathbf{y}_1,\ldots, \mathbf{y}_M]\in\mathbb{R}^{M\times M}$ and $\mathbf{V}=[\mathbf{v}_1,\ldots, \mathbf{v}_M]\in\mathbb{R}^{N\times N}$ are orthogonal matrices, and $\mathbf{\Sigma}\in\mathbb{R}^{M\times N}$ is the diagonal matrix in which diagonal elements are M singular values arranged in decreasing order. We investigate the singular spectrum $\mathbf{Y}^T\boldsymbol{\zeta}$ to analyze the amount of useful information contained in the following experimental impedance vectors $\boldsymbol{\zeta}$

$$\boldsymbol{\zeta} = \begin{cases} \dfrac{\mathbf{Z}_f - \mathbf{Z}_1}{\mathbf{Z}_1} & \text{in } fd\text{-EIT} \\ \dfrac{\mathbf{Z}_{f+1} - \mathbf{Z}_f}{\mathbf{Z}_f} & \text{in } fda\text{-EIT} \\ \langle {}^*\mathbf{Z} \rangle_f - \langle {}^*\mathbf{Z} \rangle_1 & \text{in } rfd\text{-EIT} \\ \langle {}^*\mathbf{Z} \rangle_{f+1} - \langle {}^*\mathbf{Z} \rangle_f & \text{in } rfda\text{-EIT} \end{cases} \tag{5.23}$$

The $\mathbf{Y}^T\boldsymbol{\zeta}$ of a set of $\boldsymbol{\zeta}$ indicates how useful that set of $\boldsymbol{\zeta}$ is for image reconstruction given noise level δ [1]. **Figure 5.12** shows logarithmic singular spectra $\log(\mathbf{Y}^T\boldsymbol{\zeta})$ from the experiments with eight subjects' calves in which the negative values in $\mathbf{Y}^T\boldsymbol{\zeta}$ are excluded when taking

logarithms, resulting in various numbers of effective measurements M_e. Moreover, in order to make a direct comparison, we took the average of $\log(\mathbf{Y}^T\boldsymbol{\zeta})$ over f. Ratiometric EIT significantly increases $\log(\mathbf{Y}^T\boldsymbol{\zeta})$ in terms of magnitudes and M_e as compared to classical EIT. This phenomenon certifies that ratiometric EIT contains more useful elements in $*\boldsymbol{\sigma}$ by

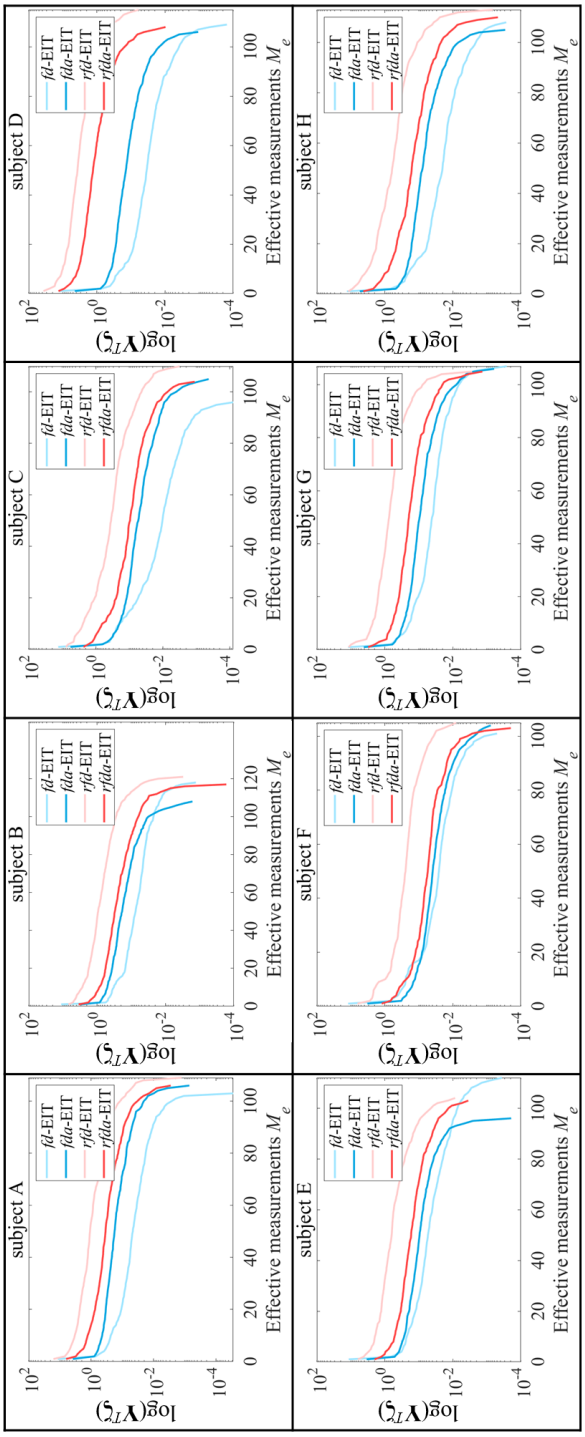

Figure 5.12. Logarithmic singular spectra $\log(\mathbf{Y}^T\boldsymbol{\zeta})$ by classical EIT (*fd*-EIT and *fda*-EIT) and ratiometric EIT (*rfd*-EIT and *rfda*-EIT).

preprocessing **Z**, which may be related to the reduced ill-posedness in terms of the continuity of solutions [1] produced by the improved distinguishability.

5.5.4. Contact impedance variances

We experimentally find that ratiometric preprocessing is also useful for impedance measurements with dry electrodes, such as the textile electrodes used in this study, where the contact impedance z^{ci} is inherently huge and complicated. The characteristic of z^{ci} significantly varies with individuals, making the impedance measurements challenging to model its magnitudes and variances beforehand. We can confirm this observation by using the *in-situ* measurement method, which simply calculates the impedance difference of two- and four-wire measurements [38]:

$$z^{ci} = \frac{\tilde{z}_{l,[l+1]} - z_{l,[l+1]} + \tilde{z}_{[l-1],l} - z_{[l-1],l} - \tilde{z}_{[l-1],[l+1]} + z_{[l-1],[l+1]}}{2I_0} \tag{5.24}$$

where $z_{l,[l+1]}$ and $\tilde{z}_{l,[l+1]}$ represent the raw impedances measured across the l and l+1-th electrodes by four- and two-wire measurements, respectively. **Figure 5.13** provides an understanding of z^{ci} affecting the impedance measurement —the response of z^{ci} changes over the subjects in the magnitude range of $10^3 < z^{ci} < 10^7$. **Figure 5.13(a)** shows the spatial variances in z^{ci} at f=500Hz, significantly changing over the electrodes. **Figure 5.13(b)** shows the frequency dependency in z^{ci} on electrode e_1, decreasing over f. A large magnitude in z^{ci} leads to an almost artifact-free image; meanwhile, the sensitivity to the domain Ω becomes significantly small; by contrast, a small magnitude generates artifacts due to the excessive amount of noise near $\partial\Omega$. The variations in z^{ci}, which are as little as a few tens of percent, cause artifacts distributed throughout the image [39]. These spatial variances in z^{ci} limit the ability of classical EIT to show more physiological features of interest. Furthermore, z^{ci} is essentially frequency-dependent because of the complicated system [40]. For instance, the classical *fd*-EIT takes the frequency-dependent behavior directly into consideration in analyzing $\boldsymbol{\sigma}$ without compensating z^{ci}, masking the internal physiological information on **Z**.

5.5.5. Simulation of contact impedance

In order to study the influence of a) the spatial variances and b) the frequency dependency in z^{ci} on the accuracy of $\boldsymbol{\sigma}$, four cases are investigated as shown in **Figure 5.14**. Here, z^{ci} is arbitrarily extracted from a Gaussian distribution N_0

$$z^{ci} \sim N_0^{(\mu_f, s_f^2)} \tag{5.25}$$

where μ_f is a given mean of z^{ci} at f, which stems from the parallel connection of the capacitance C and resistance R, and s_f is a corresponding standard deviation. **Figure 5.14(a)** shows examples of the spatial variances in z^{ci} at f=500Hz. In cases 1 and 4, z^{ci} remains free from the spatial variances. Meanwhile, in cases 2 and 3, z^{ci} are irregular over the electrodes. However, the magnitude is primarily higher in case 2 than in case 3. Subsequently, the frequency dependency of z^{ci} is investigated. **Figure 5.14(b)** shows examples of the frequency dependency in z^{ci} on electrode e_1. In cases 1 and 4, z^{ci} remains constant over f, however, the latter has a larger magnitude. In cases 2 and 3, z^{ci} decreases over f in different gradients. $\boldsymbol{\sigma}^{\Omega}$ in four cases are provided in **Figure 5.15** with the corresponding *cc*. *fd*-EIT and *fda*-EIT suffer from dome-shaped artifacts; thus, only overestimated SAT layers are detected. In case 3, where the spatial variances in z^{ci} are the biggest, *fda*-EIT reconstructs the worst, leading to an almost meaningless image. Overall, classical EIT scores lower *cc* than ratiometric EIT. Ratiometric EIT show SAT layer and the bone tibia clearly, representing almost artifact-free

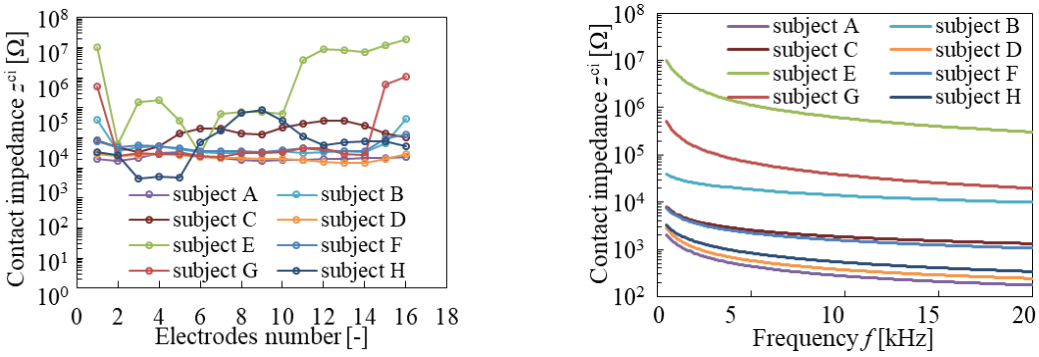

(a) **(b)**

Figure 5.13. (a) Spatial variances in contact impedance z^{ci} at f=500Hz in experiment with eight subjects. (b) Frequency dependency in z^{ci} on electrode e_1.

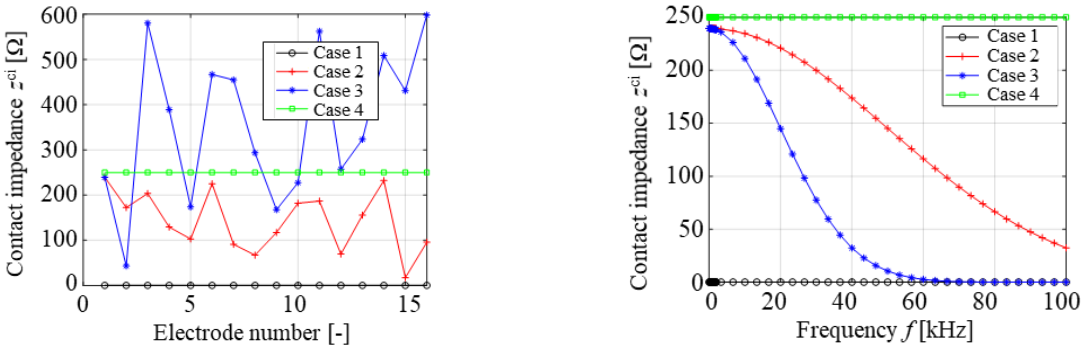

(a) **(b)**

Figure 5.14. (a) Spatial variances in contact impedance z^{ci} at f=500Hz in four cases. (b) Frequency dependency in z^{ci} on electrode e_1.

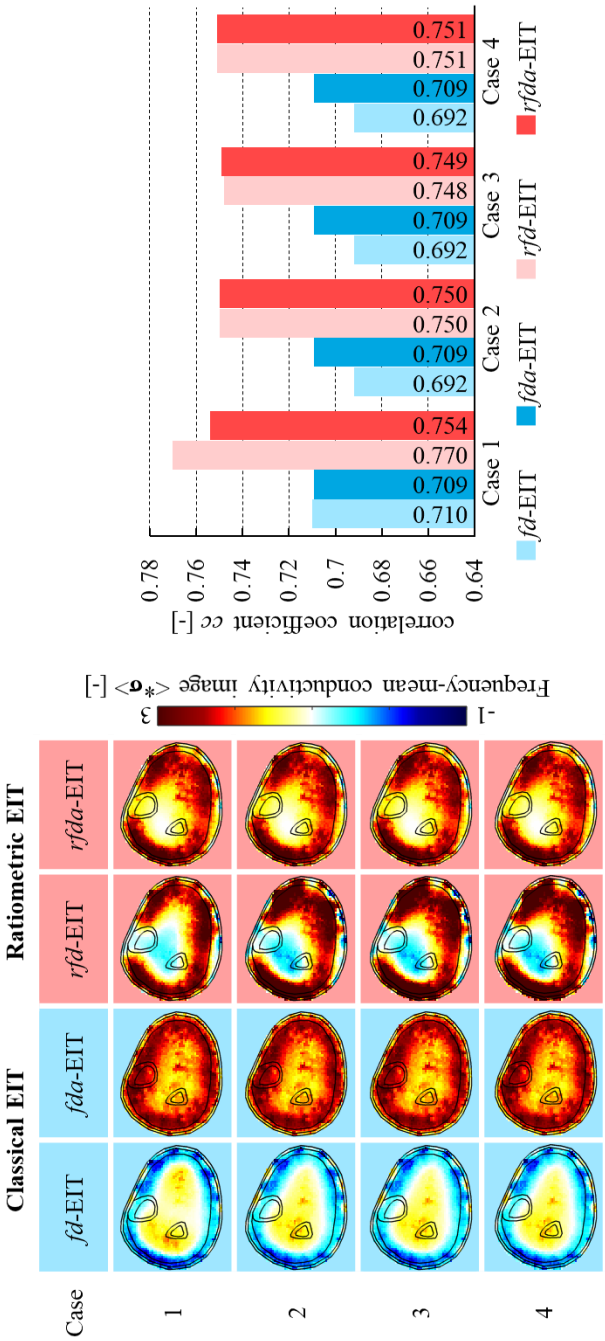

Figure 5.15. Frequency-mean conductivity images <*σ> by classical EIT (*fd*-EIT and *fda*-EIT) and ratiometric EIT (*rfd*-EIT and *rfda*-EIT) in various contact impedances z_{ci} (Case 1, 2, 3, and 4 as shown in Figure 5.14) and Correlation coefficient *cc* of each algorithm.

images even in the case of the high spatial variances in z^{ci}. *rfd*-EIT and *rfda*-EIT similarly compensate for the spatial variances in z^{ci} demonstrate characteristics except for case 1, where z^{ci} is small and constant over the electrodes, *rfd*-EIT scoring higher *cc* than *rfda*-EIT. This inequality probably stems from the SNR difference in the case of the ideal noise-free

condition. Overall, the ratiometric preprocessing contributed to mitigate the spatial variances in z^{ci}.

As a result, the assumption of classical EIT is invalid as they hypothesize the parameters are constant all over the measurements and electrodes. Therefore, ratiometric EIT is superior to classical EIT because the affected area representing the abnormal dielectric condition can be characterized by considering the frequency-dependent behavior independent of the spatial variances in z^{ci}.

5.6. Summary

A multifrequency electrical impedance tomography (*mf*-EIT) with a ratiometric preprocessing (ratiometric EIT) has been proposed for human body compartments imaging and numerically and experimentally evaluated. The objective was to image calf compartments by minimizing the conductivity contrast μ that is inherently high in the human body. Based on the results and evaluation of the reconstructed performance, it can be concluded that using the proposed ratiometric EIT has the following merits.

(1) Ratiometric EIT was capable of minimizing μ while maintaining high distinguishability in the heterogeneous background without any *a priori* information.

(2) The numerical simulation in the variant conditions of μ with newly derived ratiometric EIT successfully improved the reconstruction performance with the area ratio error of subcutaneous adipose tissue (SAT) $17.09\% < ARE^{SAT} < 28.13\%$, the position error of bone tibia $0.14\% < PE^{tibia} < 10.19\%$, the position error of bone fibula $9.51\% < PE^{fibula} < 1.74\%$, and the correlation coefficients $0.79 < CC < 0.91$.

(3) *rfda*-EIT is the best for calf compartments imaging among all the methods evaluated in the experiment by comparing to the ultrasound images, which scored the total-mean area ratio error $\langle ARE^{SAT} \rangle = 5.18\%$ of SAT and the true positive rate $TPR^{tibia} = 87.5\%$ for the bone tibia detection

(4) Ratiometric EIT successfully increased distinguishability, which was theoretically confirmed by finite precision measurements that ratiometric EIT distinguishes (a) smaller radius and smaller conductivity anomaly located in the center compared to classical EIT and (b) smaller conductivity anomalies located near the boundary, which cannot be distinguished by classical EIT.

It is concluded that implementing ratiometric EIT will help improve the treatment as a point-of-care imaging of human body compartments.

Appendix. LAPLACE EQUATION CALCULATION

Laplace equation (Equation (5.18)) is calculated in a similar way as the study of Isaacson 1986 [20]; therefore, only the critical information is provided using classical EIT. Firstly, in the case of background conductivity image ${}^0\boldsymbol{\sigma}_f$ shown in **Figure 5.10(a)**, Laplace equation is solved given the continuum condition and the finite condition. Voltage u on the boundary $\partial\Omega$ is represented by Fourier series with coefficient U_α

$$u(\mathbf{r},\theta) = \sum_{\alpha=0}^{\infty} U_\alpha e^{i\alpha\theta} \tag{5.a1}$$

if current density j on $\partial\Omega$ is assumed as a function of θ

$$j(\theta) = \sum_{\alpha=1}^{\infty} C_\alpha e^{i\alpha\theta} \tag{5.a2}$$

with

$$C_\alpha = \frac{1}{2\pi}\int_0^{2\pi} j(\theta)\, e^{-i\alpha\theta}\, d\theta$$

and with $\|\mathbf{J}\|_{1/2}=1$ where

$$\|g\|_{1/2} = \left(\int_{\partial\Omega} |g(\mathbf{r})|^2 dA\right)^{1/2}$$

for a function $g(\mathbf{r})$ and where dA is the element of the area on $\partial\Omega$. In the forward problem, the following equation is considered

$$\Lambda_\sigma\left(\sum_{\alpha=0}^{\infty} U_\alpha e^{i\alpha\theta}\right) \equiv \sigma_f^{bg} \frac{\partial u}{\partial r}(r = R^{muscle}, \theta) \tag{5.a3}$$

where Λ_σ is the Dirichlet-to-Neumann map. Given the finite condition at $r = 0$, $u(r{=}0,\theta) = 0$, the general solution is obtained

$$u(\mathbf{r},\theta) = \frac{P_0}{2} + \sum_{\alpha=1}^{\infty} r^\alpha (P_\alpha \cos\alpha\theta + Q_\alpha \sin\alpha\theta) \tag{5.a4}$$

which is then compared to Equation (5.a1) on $\partial\Omega$ to acquire $P_\alpha = U_\alpha / (R^{muscle})^\alpha$ and $Q_\alpha = iU_\alpha / (R^{muscle})^\alpha$. Thus, the right-hand side of Equation (5.a3) is calculated as follows

$$\begin{aligned}\sigma_f^{bg} \frac{\partial u}{\partial r}(r = R^{muscle}, \theta) &= \sigma_f^{bg} \sum_{\alpha=1}^{\infty} \alpha (R^{muscle})^{\alpha-1} \left[\frac{U_\alpha}{(R^{muscle})^\alpha}\cos\alpha\theta + i\frac{U_\alpha}{(R^{muscle})^\alpha}\sin\alpha\theta\right] \\ &= \sum_{\alpha=1}^{\infty} \sigma_f^{bg} \alpha (R^{muscle})^{-1} U_\alpha e^{i\alpha\theta}\end{aligned} \tag{5.a5}$$

Equation (5.a2) and (5.a5) are compared in order to yield $U_\alpha = (R^{muscle} / \alpha \cdot \sigma^{bg}_f) C_\alpha$. Then,

Equation (5.a1) is updated with $R^{muscle} = 1$ and $\sigma^{bg}_f = 1$

$$u(\mathbf{r},\theta) = \sum_{\alpha=1}^{\infty} \frac{(R^{muscle})^{\alpha}}{\sigma_f^{bg}\alpha} C_\alpha e^{i\alpha\theta} \tag{5.a6}$$

therefore

$$z_m({}^0\boldsymbol{\sigma}_f) = \sum_{\alpha=1}^{\infty} \frac{1}{\alpha} C_\alpha e^{i\alpha\theta} \tag{5.a7}$$

Secondly, in the case of bone anomaly conductivity image ${}^1\boldsymbol{\sigma}_f$ shown in **Figure 5.10(b)**, Laplace equation is solved in a similar way as ${}^0\boldsymbol{\sigma}_f$, except that the complete general solution and the matching condition are also required. Similarly to ${}^0\boldsymbol{\sigma}_f$, Equation (5.a3) is considered. The general solution in Equation (5.a4) can be used in the case of $r < R^{bone}$; however, the complete general solution is required in the case of $r > R^{bone}$

$$\begin{aligned} u(\mathbf{r},\theta) = A_0 + B_0 \ln r + \sum_{\alpha=1}^{\infty} \big[& (A_\alpha r^{\alpha} + B_\alpha r^{-\alpha}) \cos\alpha\theta \\ & + (G_\alpha r^{\alpha} + H_\alpha r^{-\alpha}) \sin\alpha\theta \big], \text{ for } R^{bone} < r < R^{muscle} \end{aligned} \tag{5.a8}$$

Equation (5.a8) is transformed with the matching conditions in the case of $r = R^{bone}$ ($u(r^-,\theta) = u(r^+,\theta)$ and $-\sigma \cdot \nabla u(r^-,\theta) = -\sigma \cdot \nabla u(r^+,\theta)$) and then compared to Equation (5.a1) on $\partial\Omega$. In the case of $\alpha = 0$, $B_0 = 0$, and $P_0 = 2A_0$ are obtained for the cosine coefficients. In the case of $\alpha > 0$, the following are obtained

$$A_\alpha = \frac{1}{2}\left(1 + \frac{\sigma_f^a}{\sigma_f^{bg}}\right) P_\alpha \,,\; B_\alpha = \frac{1}{2}\left(1 - \frac{\sigma_f^a}{\sigma_f^{bg}}\right) (R^{bone})^{2\alpha} P_\alpha$$

The sine coefficients are also obtained in a similar way. Equation (5.a1) is converted into Euler's formula as follows

$$u(\mathbf{r},\theta) = \sum_{\alpha=0}^{\infty} U_\alpha \cos\alpha\theta + iU_\alpha \sin\alpha\theta \tag{5.a9}$$

Then equation (5.a8) and (5.a9) are compared under $R^{muscle} = 1$ and $\sigma^{bg}_f = 1$ to rewrite the coefficients

$$P_\alpha = 2U_\alpha \left(1 + \frac{\sigma_f^a}{\sigma_f^{bg}}\right)^{-1} [1 - \beta_\sigma (R^{bone})^{2\alpha}]^{-1}$$

$$Q_\alpha = 2iU_\alpha \left(1 + \frac{\sigma_f^a}{\sigma_f^{bg}}\right)^{-1} [1 - \beta_\sigma (R^{bone})^{2\alpha}]^{-1}$$

where $\beta_\sigma = (\sigma^a_f - 1)/(\sigma^a_f + 1)$. Consequently, the right-hand side of Equation (5.a3) is calculated as follows

$$\sigma_f^{bg}\frac{\partial u}{\partial r}(r=R^{bone},\theta)=\sum_{\alpha=1}^{\infty}\alpha U_\alpha[\frac{1+\beta\sigma(R^{bone})^{2\alpha}}{1-\beta\sigma(R^{bone})^{2\alpha}}]\cos\alpha\theta+i\alpha U_\alpha[\frac{1+\beta\sigma(R^{bone})^{2\alpha}}{1-\beta\sigma(R^{bone})^{2\alpha}}]\sin\alpha\theta$$
$$=\sum_{\alpha=1}^{\infty}\alpha U_\alpha[\frac{1+\beta\sigma(R^{bone})^{2\alpha}}{1-\beta\sigma(R^{bone})^{2\alpha}}]e^{i\alpha\theta} \quad (5.a10)$$

which can be compared to Equation (5.a2) in order to yield

$$U_\alpha=\alpha\frac{1+\beta\sigma(R^{bone})^{2\alpha}}{1-\beta\sigma(R^{bone})^{2\alpha}}C_\alpha$$

Then, Equation (5.a1) is updated

$$u(\mathbf{r},\theta)=\sum_{\alpha=1}^{\infty}\frac{1}{\alpha}\frac{1-\beta\sigma(R^{bone})^{2\alpha}}{1+\beta\sigma(R^{bone})^{2\alpha}}\,C_\alpha\,e^{i\alpha\theta} \quad (5.a11)$$

therefore

$$z_m({}^1\boldsymbol{\sigma}_f)=\sum_{\alpha=1}^{\infty}\frac{1}{\alpha}\frac{1-\beta\sigma(R^{bone})^{2\alpha}}{1+\beta\sigma(R^{bone})^{2\alpha}}\,C_\alpha\,e^{i\alpha\theta} \quad (5.a12)$$

Finally, equations (5.a7) and (5.a12) are used in order to characterize the distinguishable region $E({}^1\boldsymbol{\sigma}_f, {}^0\boldsymbol{\sigma}_f)$ as follows

$$\left\|\mathbf{Z}({}^1\boldsymbol{\sigma}_f)-\mathbf{Z}({}^0\boldsymbol{\sigma}_f)\right\|_{1/2}>\frac{2|\beta\sigma|(R^{bone})^{2\alpha}}{1+\beta\sigma(R^{bone})^{2\alpha}} \quad (5.a13)$$

The solution with the ratiometric preprocessing is certainly obtained by replacing β_σ to $\beta = (\mu-1)/(\mu+1)$.

Thirdly, in the case of fat anomaly conductivity image ${}^2\boldsymbol{\sigma}_f$ shown in **Figure 5.10(c)**, Laplace equation is solved in a similar way as ${}^1\boldsymbol{\sigma}_f$ in order to characterize $E({}^2\boldsymbol{\sigma}_f, {}^0\boldsymbol{\sigma}_f)$ as follows

$$\left\|\mathbf{Z}({}^2\boldsymbol{\sigma}_f)-\mathbf{Z}({}^0\boldsymbol{\sigma}_f)\right\|_{1/2}>1-\frac{1+\beta(R^{muscle})^2}{\sigma_f^a[1-\beta(\mathrm{R}^{muscle})^2]} \quad (5.a14)$$

References

[1] D. S. Holder, *Electrical impedance tomography: methods, history and applications*. Bristol, UK: IOP Publishing, 2005.

[2] C. A. Andersen, S. Holden, J. Vela, M. S. Rathleff, and M. B. Jensen, "Point-of-care ultrasound in general practice: A systematic review," *Ann. Fam. Med.*, vol. 17, no. 1, pp. 61–69, 2019, doi: 10.1370/afm.2330.

[3] A. G. Warren, B. A. Janz, L. J. Borud, and S. A. Slavin, "Evaluation and management of the fat leg syndrome," *Plast. Reconstr. Surg.*, vol. 119, no. 1, pp. 9–15, 2007, doi: 10.1097/01.prs.0000244909.82805.dc.

[4] S. Vasikaran *et al.*, "Markers of bone turnover for the prediction of fracture risk and monitoring of osteoporosis treatment: A need for international reference standards,"

Osteoporos. Int., vol. 22, no. 2, pp. 391–420, 2011, doi: 10.1007/s00198-010-1501-1.

[5] C. Yu, S. Yue, J. Wang, and H. Wang, "An effective measured data preprocessing method in electrical impedance tomography," *Sci. World J.*, vol. 2014, p. 208765, 2014, doi: 10.1155/2014/208765.

[6] B. Sun, S. Yue, Z. Cui, and H. Wang, "A new linear back projection algorithm to electrical tomography based on measuring data decomposition," *Meas. Sci. Technol.*, vol. 26, no. 12, p. 125402, Oct. 2015, doi: 10.1088/0957-0233/26/12/125402.

[7] Z. Wang, S. Yue, H. Wang, and Y. Wang, "Data preprocessing methods for electrical impedance tomography: A review," *Physiological Measurement*, vol. 41, no. 9. IOP Publishing Ltd, p. 09TR02, Sep. 2020, doi: 10.1088/1361-6579/abb142.

[8] J. Yao and M. Takei, "Application of process tomography to multiphase flow measurement in industrial and biomedical fields: A review," *IEEE Sens. J.*, vol. 17, no. 24, pp. 8196–8205, 2017, doi: 10.1109/JSEN.2017.2682929.

[9] H. Griffiths and A. Ahmed, "A dual-frequency applied potential tomography technique: computer simulations," *Clin. Phys. Physiol. Meas.*, vol. 8, pp. 103–107, 1987.

[10] D. Andreuccetti, R. Fossi, and C. Petrucci, "An internet resource for the calculation of the dielectric properties of body tissues in the frequency range 10 Hz - 100 GHz," *IFAC-CNR, Florence (Italy), Based data Publ. by C Gabriel al. 1996.*, 1997.

[11] D. S. Holder and A. Khan, "Use of polyacrylamide gels in a saline-filled tank to determine the linearity of the Sheffield Mark 1 electrical impedance tomography (EIT) system in measuring impedance disturbances," *Physiol. Meas.*, vol. 15, pp. A45–A50, 1994, doi: 10.1088/0967-3334/15/2A/006.

[12] G. Hahn *et al.*, "Imaging pathologic pulmonary air and fluid accumulation by functional and absolute EIT," *Physiol. Meas.*, vol. 27, no. 5, pp. S187-198, 2006, doi: 10.1088/0967-3334/27/5/S16.

[13] B. Packham *et al.*, "Comparison of frequency difference reconstruction algorithms for the detection of acute stroke using EIT in a realistic head-shaped tank," *Physiol. Meas.*, vol. 33, no. 5, pp. 767–786, 2012, doi: 10.1088/0967-3334/33/5/767.

[14] J. K. Seo, J. Lee, S. W. Kim, H. Zribi, and E. J. Woo, "Frequency-difference electrical impedance tomography (fdEIT): Algorithm development and feasibility study," *Physiol. Meas.*, vol. 29, no. 8, pp. 929–944, 2008, doi: 10.1088/0967-3334/29/8/006.

[15] J. Jang and J. K. Seo, "Detection of admittivity anomaly on high-contrast heterogeneous backgrounds using frequency difference EIT," *Physiol. Meas.*, vol. 36, no. 6, pp. 1179–1192, 2015, doi: 10.1088/0967-3334/36/6/1179.

[16] E. Malone, G. S. Dos Santos, D. Holder, and S. Arridge, "Multifrequency electrical impedance tomography using spectral constraints," *IEEE Trans. Med. Imaging*, vol. 33, no. 2, pp. 340–350, 2014, doi: 10.1109/TMI.2013.2284966.

[17] M. F. Vitha and R. J. Clarke, "Comparison of excitation and emission ratiometric fluorescence methods for quantifying the membrane dipole potential," *Biochim. Biophys. Acta - Biomembr.*, vol. 1768, no. 1, pp. 107–114, 2007, doi: 10.1016/j.bbamem.2006.06.022.

[18] H. Xu, J. W. Aylott, R. Kopelman, T. J. Miller, and M. A. Philbert, “A real-time ratiometric method for the determination of molecular oxygen inside living cells using sol-gel-based spherical optical nanosensors with applications to rat C6 glioma,” *Anal. Chem.*, vol. 73, no. 17, pp. 4124–4133, 2001, doi: 10.1021/ac0102718.

[19] H. W. Noh, C. G. Ahn, H. J. Kong, and J. Y. Sim, “Ratiometric impedance sensing of fingers for robust identity authentication,” *Sci. Rep.*, vol. 9, no. 1, pp. 1–12, 2019, doi: 10.1038/s41598-019-49792-9.

[20] D. Isaacson, “Distinguishability of conductivities by electric current computed tomography,” *IEEE Trans. Med. Imaging*, vol. 5, no. 2, pp. 91–95, 1986, doi: 10.1109/TMI.1986.4307752.

[21] C. Kotre, “A sensitivity coefficient method for the reconstruction of electrical impedance tomograms,” *Clin. Phys. Physiol. Meas.*, vol. 10, no. 3, pp. 275–281, 1989.

[22] B. Harrach and J. K. Seo, “Exact shape-reconstruction by one-step linearization in electrical impedance tomography,” *SIAM J. Math. Anal.*, vol. 42, no. 4, pp. 1505–1518, 2010, doi: 10.1137/090773970.

[23] M. Vauhkonen, D. Vadâsz, P. A. Karjalainen, E. Somersalo, and J. P. Kaipio, “Tikhonov regularization and prior information in electrical impedance tomography,” *IEEE Trans. Med. Imaging*, vol. 17, no. 2, pp. 285–293, 1998, doi: 10.1109/42.700740.

[24] P. N. Darma and M. Takei, “High-Speed and Accurate Meat Composition Imaging by Mechanically-Flexible Electrical Impedance Tomography with k-Nearest Neighbor and Fuzzy k-Means Machine Learning Approaches,” *IEEE Access*, vol. 9, pp. 38792–38801, 2021, doi: 10.1109/ACCESS.2021.3064315.

[25] M. Vauhkonen, W. R. B. Lionheart, L. M. Heikkinen, P. J. Vauhkonen, and J. P. Kaipio, “A MATLAB package for the EIDORS project to reconstruct two-dimensional EIT images,” *Physiol. Meas.*, vol. 22, no. 1, pp. 107–111, 2001, doi: 10.1088/0967-3334/22/1/314.

[26] J. Schöberl, “An advancing front 2D/3D-mesh generator based on abstract rules,” *Comput. Vis. Sci.*, vol. 1, no. 1, pp. 41–52, 1997, doi: 10.1007/s007910050004.

[27] M. R. Baidillah, A. A. S. Iman, Y. Sun, and M. Takei, “Electrical Impedance Spectro-Tomography Based on Dielectric Relaxation Model,” *IEEE Sens. J.*, vol. 17, no. 24, pp. 8251–8262, 2017, doi: 10.1109/JSEN.2017.2710146.

[28] P. N. Darma, M. R. Baidillah, M. W. Sifuna, and M. Takei, “Real-time dynamic imaging method for flexible boundary sensor in wearable electrical impedance tomography,” *IEEE Sens. J.*, vol. 20, no. 16, pp. 9469–9479, 2020, doi: 10.1109/JSEN.2020.2987534.

[29] P. A. Sejati *et al.*, “On-Line Multi-Frequency Electrical Resistance Tomography High-Temperature Molten Oxide,” *Sensors*, vol. 22, no. 3, p. 1025, 2022.

[30] R. Ogawa, M. R. Baidillah, S. Akita, and M. Takei, “Investigation of physiological swelling on conductivity distribution in lower leg subcutaneous tissue by electrical impedance tomography,” *J. Electr. Bioimpedance*, vol. 11, no. May, pp. 19–25, 2020.

[31] E. J. Lee *et al.*, “Design of a microscopic electrical impedance tomography system for 3D continuous non-destructive monitoring of tissue culture,” *Biomed. Eng. Online*, vol. 13, no. 142, pp. 1–15, 2014, doi: 10.1186/1475-925X-13-142.

[32] L. Jin *et al.*, “Highly precise nanofiber web-based dry electrodes for vital signal monitoring,” *RSC Adv.*, vol. 6, no. 46, pp. 40045–40057, 2016, doi: 10.1039/c6ra00079g.

[33] A. McEwan, G. Cusick, and D. S. Holder, “A review of errors in multi-frequency EIT instrumentation,” *Physiol. Meas.*, vol. 28, no. 7, p. S197, 2007, doi: 10.1088/0967-3334/28/7/S15.

[34] F. Frauziols *et al.*, “Prediction of the biomechanical effects of compression therapy by finite element modeling and ultrasound elastography,” *IEEE Trans. Biomed. Eng.*, vol. 62, no. 4, pp. 1011–1019, 2015, doi: 10.1109/TBME.2014.2378553.

[35] D. G. Altman and J. M. Bland, “Diagnostic tests. 1: Sensitivity and specificity.,” *BMJ*, vol. 308, no. 69, p. 1552, 1994, doi: 10.1258/phleb.2012.012J05.

[36] P. J. Riu, J. Rosell, A. Lozano, and R. Pallà-Areny, “Multi-frequency static imaging in electrical impedance tomography: Part 1 instrumentation requirements,” *Med. Biol. Eng. Comput.*, vol. 33, no. 6, pp. 784–792, 1995, doi: 10.1007/BF02523010.

[37] M. Hintermüller, A. Laurain, and A. A. Novotny, “Second-order topological expansion for electrical impedance tomography,” *Adv. Comput. Math.*, vol. 36, no. 2, pp. 235–265, 2012, doi: 10.1007/s10444-011-9205-4.

[38] E. J. Woo, P. Hua, J. G. Webster, W. J. Tompkins, and R. Pallás-Areny, “Skin impedance measurements using simple and compound electrodes,” *Med. Biol. Eng. Comput.*, vol. 30, no. 1, pp. 97–102, 1992, doi: 10.1007/BF02446200.

[39] K. G. Boone and D. S. Holder, “Effect of skin impedance on image quality and variability in electrical impedance tomography: A model study,” *Med. Biol. Eng. Comput.*, vol. 34, no. 5, pp. 351–354, 1996, doi: 10.1007/BF02520003.

[40] F. Xiong, D. Chen, Z. Chen, C. Jin, and S. Dai, “Impedance characteristics of the skin-electrode interface of dry textile electrodes for wearable electrocardiogram,” in *G. Fortino and Z. Wang (eds.), Advances in Body Area Networks, Internet of Things*, vol. I, 2019, pp. 343–356.

Chapter 6

Local-spatiotemporal Change Monitoring in Extracellular Fluid by Time-variation-constraint Sparse Bayesian Learning Implemented into Frequency-difference Electrical Impedance Tomography (*tvc*SBL-*fd*EIT)

6. Local-spatiotemporal Change Monitoring in Extracellular Fluid by Time-variation-constraint Sparse Bayesian Learning Implemented into Frequency-difference Electrical Impedance Tomography (*tvc*SBL-*fd*EIT)

6.1. Research Motivation

A balance of volume/concentration in the extracellular fluid (ECF) is important to keep physiological wellbeing because fluctuated volume/concentration beyond normal level raises adverse health complications such as lymphedema [1], chronic kidney disease [2], and obesity [3]. Therefore, the fluctuated volume/concentration needs to be measured by diagnostic equipment to monitor disease progression [4]. Since local-spatiotemporal change (LSTC) of volume/concentration in ECF due to excessive accumulated components, e.g., sodium ion and protein, varies among patients and body parts, monitoring of LSTC is critical to preventing severe disease manifestation. Generally, imaging modalities such as magnetic resonance imaging (MRI) and X-ray computed tomography (CT) monitor "local-spatio" change of morphological structure, not "local-temporal" change [5]. In order to satisfy both "local-spatio" and "local-temporal" change of morphological structure, ultrasound imaging (UI) is typically used for the early diagnosis of adverse health complications [6]. However, UI still does not monitor components volume/concentration in ECF because UI focuses on morphological structure of the whole cross-sectional diseased tissue, e.g., subcutaneous adipose tissue (SAT). As an alternative modality, bioelectrical impedance analysis (BIA) is commonly used as a non-invasive, harmless, and simple method for monitoring impedance arising from "local-temporal" change of components volume/concentration in ECF [7]. However, BIA is not able to monitor "local-spatio" change of components volume/concentration in ECF because the measurement target is too broad on the whole section of human limbs; therefore, BIA is unreliable for monitoring the LSTC [8].

Under these circumstances, electrical impedance tomography (EIT) is getting more desirable than the above conventional monitoring modalities because EIT is able to monitor both "spatio" and "temporal" (spatiotemporal) change of components volume/concentration in ECF as well as easy operation, non-invasive, harmless, low cost, and capable of real-time monitoring [9]. Generally, EIT images conductivity distribution $\boldsymbol{\sigma}$ [10] to monitor body fluids

such as urine in bladder [11], edema in lung [12], hemorrhage and blood accumulation in head [13]. Already, we have monitored spatiotemporal change in ECF in SAT during prolonged standing and post-exercise [14] by frequency-difference EIT (*fd*EIT) based on a wearable sensor [15]. The *fd*EIT is theoretically able to monitor spatiotemporal change of components volume/concentration in ECF because $\boldsymbol{\sigma}$ of NaCl solution as the main component in ECF is frequency-independent below frequency f = 1MHz [16], whereas $\boldsymbol{\sigma}$ of protein solution as the subcomponent in ECF is frequency-dependent [17]. Nevertheless, the conventional *fd*EIT is not able to accurately monitor the LSTC because the continuity of inverse problem solution is not sufficiently guaranteed due to very small "local" effect on measured impedance $\mathbf{Z}$ [10] in the LSTC fields.

Many approaches to implement machine learning into EIT were proposed to solve the problem of inaccurate monitoring under the LSTC fields. Among the machine learning approaches, the fundamental theory of sparse Bayesian learning (SBL) was developed to monitor local change [18]. Shen *et al.* monitored "local-spatio" change in cognitive biomarkers of Alzheimer's disease patients by SBL implemented into MRI [19]. However, the 1st generation of SBL is not able to monitor "local-temporal" change because the SBL is not able to extract the inter-vector correlations. In order to solve the problem, Zhang *et al.* introduced a positive-definite matrix $\mathbf{B}$ related to the temporal correlation into the SBL as the 2nd generation of SBL to monitor the "local-temporal" change from electrocardiogram (EGG) signals [20]. In order to achieve both "local-spatio" and "local-temporal" change (LSTC), Liu *et al.* introduced the fundamental approach of SBL implemented into conventional EIT (SBL-EIT) [21] to verify the image reconstruction performance in simple ink flow around a cylinder. The conventional SBL-EIT assumes a sparse prior distribution $p(\boldsymbol{\sigma};\boldsymbol{\gamma})$ ($\boldsymbol{\gamma}$: prior variance vector) with respect to the unknown-variable $\boldsymbol{\sigma}$. By learning $\boldsymbol{\gamma}$ related to the sparsity of the likelihood $p(\mathbf{Z}|\boldsymbol{\gamma})$, the MAP (maximum a posteriori) estimation is obtained, which maximizes the posterior distribution $p(\boldsymbol{\sigma}|\mathbf{Z};\ \boldsymbol{\gamma})$ with respect to $\boldsymbol{\sigma}$. Generally, $\boldsymbol{\sigma}$ changes with several coherent "spatio" or "temporal" structures in medical monitoring applications; thus, learning the valid structures is the target of the conventional SBL-EIT framework. A typical example of EIT that uses the "temporal" structure (without machine learning) is the approach based on the Kalman filter [22] and its extensions, such as the Ensemble Kalman filter [23], which are not able to monitor the "local-spatio" change.

However, the LSTC is not accurately monitored by the conventional SBL-EIT in the unstable-background fields where the background $\boldsymbol{\sigma}$ changes more significantly than the

LSTC in the region of interest (ROI). Human subcutaneous tissue is composed mainly of SAT and muscle as the background while veins as the ROI. Since **σ** of SAT is 10 times smaller than that of muscle [24], it is challenging to monitor the LSTC near veins in SAT which is the unstable-background fields. In this context, subsequent extensions of the conventional SBL-EIT on time sequence learning [25] and *fd*EIT [26] may still suffer in the unstable-background fields. In order to overcome the drawbacks in the unstable-background fields, this study proposes "time-variation-constraint (*tvc*)" SBL implemented into *fd*EIT (*tvc*SBL-*fd*EIT) for monitoring very small frequency-dependent LSTC. The *tvc*SBL-*fd*EIT has two significant possibilities; namely, 1) the iterative image reconstruction with block sparsity extracts the temporal correlation in the unstable-background fields, and 2) the time variation constraint separates SAT from muscle based on the prior information about the time-varying frequency-dependency of **σ** in SAT and muscle.

This study aims to achieve three objectives which are 1) to propose *tvc*SBL-*fd*EIT for monitoring the LSTC in the unstable-background fields, 2) to evaluate the reconstruction performance of *tvc*SBL-*fd*EIT on 15 subjects' calves along with an experimental protocol of prolonged standing and leg elevation, and 3) to investigate frequency-dependency of **σ** in ECF, the local maximum position of frequency-difference conductivity distribution Δ**σ**, and the key parameters of the reconstruction performance.

6.2. Time-variation-constraint Sparse Bayesian Learning Implemented Into Frequency-Difference Electrical Impedance Tomography (*tvc*SBL-*fd*EIT)

6.2.1. Overview

Figure 6.1 shows the structure of time-variation-constraint sparse Bayesian learning (*tvc*SBL) implemented into frequency-difference electrical impedance tomography (*fd*EIT) which denotes "*tvc*SBL-*fd*EIT" for monitoring local-spatiotemporal change (LSTC) of conductivity distribution **σ** in the extracellular fluid (ECF) in subcutaneous adipose tissue (SAT). The *tvc*SBL-*fd*EIT has three steps which are Step 1: formulation of blocked column vector (BCV), Step 2: SAT separation by time variation constraint, and Step 3: temporal correlation extraction by hyperparameter learning. Step 1 consists of three subsets which are Step 1-1: time-frequency-dependent impedance measurement, Step 1-2: concatenation in the time direction, and Step 1-3: column-vectorization. In Step 1-1, the single measurement vector of **Z** at time t_k ($\mathbf{Z}_k$-SMV), which is both time-dependent and frequency-dependent, is

obtained. In Step 1-2, $\mathbf{Z}_k$-SMV is formulated into the multiple measurement vector of the frequency-difference impedance $\Delta\mathbf{Z}$ ($\Delta\mathbf{Z}$-MMM) concatenated in the time direction t_k. Similarly to $\Delta\mathbf{Z}$-MMM, the SMV of $\boldsymbol{\sigma}$ ($\boldsymbol{\sigma}_k$-SMV) and noise vector $\boldsymbol{\varepsilon}$ ($\boldsymbol{\varepsilon}_k$-SMV) at t_k are also formulated into the frequency-difference conductivity distribution $\Delta\boldsymbol{\sigma}$ ($\Delta\boldsymbol{\sigma}$-MMM) and the noise matrix $\boldsymbol{\varepsilon}$ ($\boldsymbol{\varepsilon}$-MMM), respectively. In Step 1-3, the three types of MMM are transformed

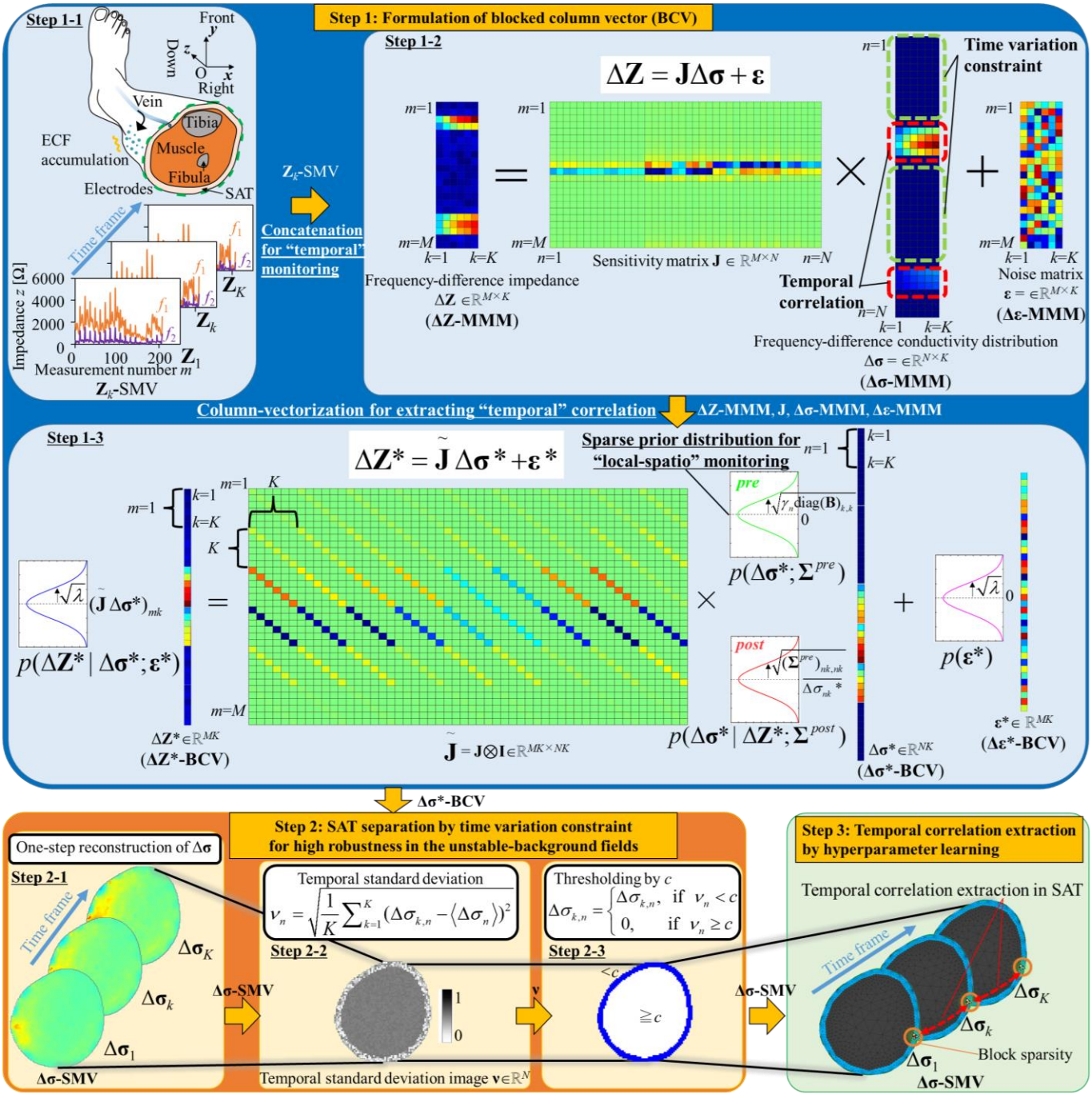

Figure 6.1. Structure of time-variation-constraint sparse Bayesian learning in frequency-difference electrical impedance tomography (*tvc*SBL-*fd*EIT).

to the three types of blocked column vector (BCV), i.e., $\Delta\mathbf{Z}^*$ ($\Delta\mathbf{Z}^*$-BCV), $\Delta\boldsymbol{\sigma}^*$ ($\Delta\boldsymbol{\sigma}^*$-BCV), and $\boldsymbol{\varepsilon}^*$ ($\boldsymbol{\varepsilon}^*$-BCV) by column-vectorization for extracting the temporal correlation. Step 2 consists of three subsets which are Step 2-1: one-step reconstruction of $\Delta\boldsymbol{\sigma}$, Step 2-2: calculation of temporal standard deviation, and Step 2-3: thresholding based on time variation constraint. In Step 2-1, the one-step image reconstruction is performed using a sensitivity matrix $\mathbf{J}$ which is common at all times. In Steps 2-2 and 2-3, SAT is separated by applying the time variation constraint on the one-step reconstructed image. In this way, the elements in SAT are separated by excluding those in muscle as background. In Step 3, the temporal correlation is extracted in the separated SAT by learning hyperparameters with blocked sparsity.

6.2.2. Step1: Formulation of Blocked Column Vector (BCV)

Figure 6.2 shows the flowchart of *tvc*SBL-*fd*EIT consisting of Steps 1 to 3. In Step 1, the frequency-difference impedance difference $\Delta\mathbf{Z}_k \in \mathbb{R}^M$ (i.e., $\mathbf{Z}_k$-SMV) at the time t_k between one measured impedance $\mathbf{Z}_{k,f2}$ at high-frequency f_2 and another measured impedance $\mathbf{Z}_{k,f1}$ at low-frequency f_1 is expressed as

$$\Delta\mathbf{Z}_k = (\mathbf{Z}_{k,\,f2} - \mathbf{Z}_{k,\,f1}) \oslash \mathbf{Z}_{k,\,f1} = \mathbf{J}\Delta\boldsymbol{\sigma}_k + \boldsymbol{\varepsilon}_k \tag{6.1}$$

where M is the total number of measurements, subscript k (k = 1, 2,..., K) is the time frame number [-] with time t_k defined as $t_k = k \times \Delta k$ [s], Δk[s] is the time step size in discretization, the symbol $\oslash$ is the element-wise division of the vector, $\mathbf{J} \in \mathbb{R}^{M\times N}$ is the sensitivity matrix, $\Delta\boldsymbol{\sigma}_k \in \mathbb{R}^N$ is the frequency-difference conductivity distribution, N is the total number of elements,

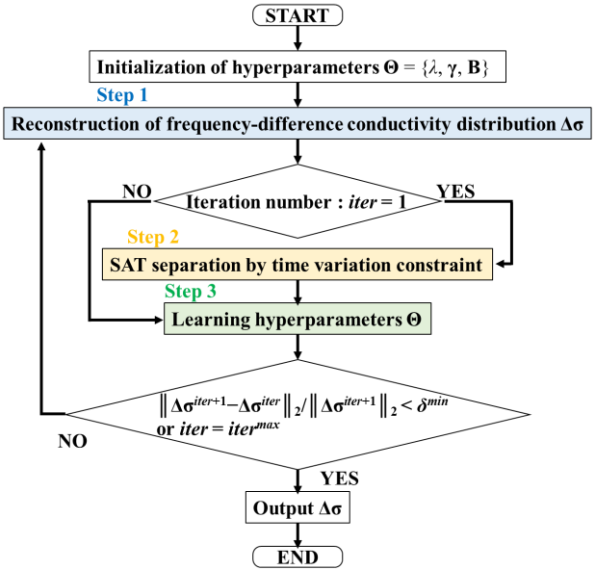

Figure 6.2. Flowchart of time-variation-constraint sparse Bayesian learning implemented into frequency-difference electrical impedance tomography (*tvc*SBL-*fd*EIT).

and $\boldsymbol{\varepsilon}_k = [\varepsilon_{k,1},\ldots, \varepsilon_{k,m}, \ldots, \varepsilon_{k,M}]^T \in \mathbb{R}^M$ is the noise vector. The *tvc*SBL-*fd*EIT extends the SMV (Equation (6.1)) into the MMM as follows

$$\Delta\mathbf{Z} = \mathbf{J}\Delta\boldsymbol{\sigma} + \boldsymbol{\varepsilon} \tag{6.2}$$

where $\Delta\mathbf{Z} = [\Delta\mathbf{Z}_1,\ldots, \Delta\mathbf{Z}_k,\ldots, \Delta\mathbf{Z}_K] \in \mathbb{R}^{M\times K}$ (i.e., $\Delta\mathbf{Z}$-MMM), $\Delta\boldsymbol{\sigma} = [\Delta\boldsymbol{\sigma}_1,\ldots, \Delta\boldsymbol{\sigma}_k,\ldots, \Delta\boldsymbol{\sigma}_K] \in \mathbb{R}^{N\times K}$ (i.e., $\Delta\boldsymbol{\sigma}$-MMM), and $\boldsymbol{\varepsilon} = [\boldsymbol{\varepsilon}_1,\ldots, \boldsymbol{\varepsilon}_k, \ldots, \boldsymbol{\varepsilon}_K] \in \mathbb{R}^{M\times K}$ (i.e., $\Delta\boldsymbol{\varepsilon}$-MMM) where superscript T indicates the transpose of a matrix. In order to extract the temporal correlation in Equation (6.2), the MMM is formulated into the BCV by column-vectorization as follows

$$\Delta\mathbf{Z}^* = \tilde{\mathbf{J}}\,\Delta\boldsymbol{\sigma}^* + \boldsymbol{\varepsilon}^* \tag{6.3}$$

where * is the symbol of column-vectorization, $\Delta\mathbf{Z}^* \in \mathbb{R}^{MK}$ (i.e., $\Delta\mathbf{Z}^*$-BCV), $\Delta\boldsymbol{\sigma}^* \in \mathbb{R}^{NK}$ (i.e., $\Delta\boldsymbol{\sigma}^*$-BCV), $\boldsymbol{\varepsilon}^* \in \mathbb{R}^{MK}$ (i.e., $\Delta\boldsymbol{\varepsilon}^*$-BCV), $\tilde{\mathbf{J}} = \mathbf{J}\otimes\mathbf{I} \in \mathbb{R}^{MK\times NK}$, $\otimes$ is the symbol of the Kronecker product of two matrices, and $\mathbf{I} \in \mathbb{R}^{K\times K}$ is the identity matrix.

In the SBL-EIT framework, the prior probability distribution $p(\Delta\boldsymbol{\sigma}^*; \boldsymbol{\Sigma}^{pre})$, the likelihood $p(\Delta\mathbf{Z}^* | \Delta\boldsymbol{\sigma}^*; \boldsymbol{\varepsilon}^*)$, and the posterior probability distribution $p(\Delta\boldsymbol{\sigma}^* | \Delta\mathbf{Z}^*; \boldsymbol{\Sigma}^{post})$ with respect to $\Delta\boldsymbol{\sigma}^*$ are defined.

Firstly, the prior probability distribution $p(\Delta\boldsymbol{\sigma}^*; \boldsymbol{\Sigma}^{pre})$ with respect to the unknown-variable $\Delta\boldsymbol{\sigma}^*$ is defined. In *tvc*SBL-*fd*EIT, the prior probability distribution $p(\Delta\boldsymbol{\sigma}^*; \boldsymbol{\Sigma}^{pre})$ is assumed as a zero-mean multivariate Gaussian distribution in which a prior covariance matrix $\boldsymbol{\Sigma}^{pre} \in \mathbb{R}^{NK\times NK}$ consists of a prior variance vector $\boldsymbol{\gamma} = [\gamma_1,\ldots, \gamma_n,\ldots, \gamma_N]^T \in \mathbb{R}^N$ related to the sparsity, and a positive definite matrix $\mathbf{B} \in \mathbb{R}^{K\times K}$ related to the temporal correlation [20]

$$p(\Delta\boldsymbol{\sigma}^*; \boldsymbol{\Sigma}^{pre}) \sim N(\mathbf{0}, \boldsymbol{\Sigma}^{pre}) \tag{6.4}$$

where covariance matrix $\boldsymbol{\Sigma}^{pre}$ is as follows

$$\boldsymbol{\Sigma}^{pre} = \begin{bmatrix} \gamma_1\mathbf{B} & & \mathbf{0} \\ & \ddots & \\ \mathbf{0} & & \gamma_N\mathbf{B} \end{bmatrix} \tag{6.5}$$

Here $\mathbf{B}$ is common for all elements N in order to prevent overfitting [27]. In this study, an additive noise model with zero-mean Gaussian distribution is applied in accordance with the common practice in EIT image reconstruction [21], [28].

Secondly, the likelihood $p(\Delta\mathbf{Z}^* | \Delta\boldsymbol{\sigma}^*; \boldsymbol{\varepsilon}^*)$ is defined. The noise probability distribution $p(\boldsymbol{\varepsilon}^*)$ is assumed as a zero-mean multivariate Gaussian distribution in which a noise covariance matrix $\lambda\mathbf{I} \in \mathbb{R}^{MK\times MK}$ is independent and identically distributed

$$p(\boldsymbol{\varepsilon}^*) \sim N(\mathbf{0}, \lambda\mathbf{I}) \tag{6.6}$$

where λ is the noise variance. From Equations (6.3) and (6.6), the likelihood $p(\Delta\mathbf{Z}^* | \Delta\boldsymbol{\sigma}^*; \boldsymbol{\varepsilon}^*)$ with respect to $\Delta\mathbf{Z}^*$ is expressed as its conditional probability distribution as follows

$$p(\Delta\mathbf{Z}^* | \Delta\boldsymbol{\sigma}^*; \boldsymbol{\varepsilon}^*) \sim N(\tilde{\mathbf{J}}\Delta\boldsymbol{\sigma}^*, \lambda\mathbf{I}) \tag{6.7}$$

Lastly, the posterior probability distribution $p(\Delta\boldsymbol{\sigma}^* | \Delta\mathbf{Z}^*; \boldsymbol{\Sigma}^{post})$ is defined. Using Bayes' theorem, i.e., the relationship between the prior probability distribution (Equation (6.4)) and the likelihood (Equation (6.7)) which is expressed as

$$p(\Delta\boldsymbol{\sigma}^* | \Delta\mathbf{Z}^*; \boldsymbol{\Sigma}^{post}) \propto p(\Delta\mathbf{Z}^* | \Delta\boldsymbol{\sigma}^*; \boldsymbol{\varepsilon}^*) p(\Delta\boldsymbol{\sigma}^*; \boldsymbol{\Sigma}^{pre}) \tag{6.8}$$

the posterior probability distribution $p(\Delta\boldsymbol{\sigma}^* | \Delta\mathbf{Z}^*; \boldsymbol{\Sigma}^{post})$ is also a multivariate Gaussian distribution as follows

$$p(\Delta\boldsymbol{\sigma}^* | \Delta\mathbf{Z}^*; \boldsymbol{\Sigma}^{post}) \sim N(\overline{\Delta\boldsymbol{\sigma}^*}, \boldsymbol{\Sigma}^{post}) \tag{6.9}$$

where $\overline{\Delta\boldsymbol{\sigma}^*} \in \mathbb{R}^{NK}$ is the mean vector and $\boldsymbol{\Sigma}^{post} \in \mathbb{R}^{NK \times NK}$ is the posterior covariance matrix which are calculated as follows

$$\overline{\Delta\boldsymbol{\sigma}^*} = \frac{1}{\lambda}\boldsymbol{\Sigma}^{post}\tilde{\mathbf{J}}^T\Delta\mathbf{Z}^* = \left[\lambda(\boldsymbol{\Sigma}^{pre})^{-1} + \tilde{\mathbf{J}}^T\tilde{\mathbf{J}}\right]^{-1}\tilde{\mathbf{J}}^T\Delta\mathbf{Z}^* \tag{6.10}$$

$$\because\ \boldsymbol{\Sigma}^{post} = \left[(\boldsymbol{\Sigma}^{pre})^{-1} + \frac{1}{\lambda}\tilde{\mathbf{J}}^T\tilde{\mathbf{J}}\right]^{-1} \tag{6.11}$$

(See Appendix for the derivation of the inference procedure).

6.2.3. Step2: SAT Separation by Time Variation Constraint

In the SBL-EIT framework, the hyperparameters λ, $\boldsymbol{\gamma}$, and $\mathbf{B}$ need to be learned using $\Delta\mathbf{Z}$ in the iterative image reconstruction with block sparsity. In Step 2-1, $\Delta\boldsymbol{\sigma}$ is reconstructed using the hyperparameters learned in one-step (iteration number: *iter* = 1) in order to separate SAT on that $\Delta\boldsymbol{\sigma}$. Thus, the iteration process is described in the next section. Since the probability of a Gaussian distribution is maximized at its expected value, the MAP estimation of $\Delta\boldsymbol{\sigma}^*$ is $\overline{\Delta\boldsymbol{\sigma}^*}$ in Equation (6.10). Moreover, using the approximation for the MMM [20], which reduces the computational cost, $\Delta\boldsymbol{\sigma}$ is obtained as follows

$$\Delta\boldsymbol{\sigma} = \boldsymbol{\gamma}\mathbf{J}^T(\lambda\mathbf{I} + \mathbf{J}\boldsymbol{\gamma}\mathbf{J}^T)^{-1}\Delta\mathbf{Z} \tag{6.12}$$

In Step 2-2, after the one-step reconstruction by Equation (6.12), the temporal standard deviation image $\mathbf{v} = [v_1, \ldots, v_n, \ldots, v_N]^T \in \mathbb{R}^N$ is calculated based on $\Delta\boldsymbol{\sigma}$. Here the temporal standard deviation v_n is defined by

$$v_n = \sqrt{\frac{1}{K}\sum_{k=1}^{K}(\Delta\sigma_{k,n} - \langle\Delta\sigma_n\rangle)^2} \tag{6.13}$$

where $\Delta\sigma_{k,n}$ and $<\Delta\sigma_n>$ are the value on the n-th mesh of $\Delta\boldsymbol{\sigma}$ at the k-th time frame and the temporal-mean value on the corresponding element, respectively.

In Step 2-3, SAT is separated by thresholding based on the time variation constraint where only elements of v_n lower than a threshold c are preserved as illustrated in **Figure 6.1**. In order to achieve high robustness even in the unstable-background fields where the background conductivity varies greatly with time and frequency, e.g., muscle as background, $\Delta\boldsymbol{\sigma}$ is processed by thresholding the corresponding element based on the time variation constraint that v_n is smaller in SAT than that in muscle.

$$\Delta\sigma_{k,n} = \begin{cases} \Delta\sigma_{k,n}, & \text{if } v_n < c \\ 0, & \text{if } v_n \geq c \end{cases} \tag{6.14}$$

The threshold c varies widely depending on the clinical conditions and should be adjusted according to the target of interest. In this study, c is heuristically determined as the 25th percentile of elements based on *a priori* information about the relationship between $\boldsymbol{\sigma}$ of SAT and other biological tissues such as muscle. Namely, the constraint is applied to the thresholding based on the assumption that the higher $\boldsymbol{\sigma}$ indicates the bigger the time variation. The $\Delta\boldsymbol{\sigma}$ obtained by Equation (6.14) is again incorporated into the iteration process.

6.2.4. Step3: Temporal Correlation Extraction by Hyperparameter Learning

In Step 3, the hyperparameter matrix $\boldsymbol{\Theta} = \{\lambda, \boldsymbol{\gamma}, \mathbf{B}\}$ is learned by minimizing the negative log-likelihood $-\log p(\Delta\mathbf{Z}^* \mid \boldsymbol{\Theta})$. In this study, instead of directly minimizing its likelihood function $L(\boldsymbol{\Theta})$, the expectation-maximization (EM) method is used to maximize the conditional expectation of $\log p(\Delta\mathbf{Z}^* \mid \boldsymbol{\Theta})$ given $\Delta\mathbf{Z}^*$, i.e., Q-function $Q(\boldsymbol{\Theta})$, [18]. Each hyperparameter of $\boldsymbol{\Theta}$ at which the partial derivative of $Q(\boldsymbol{\Theta})$ becomes zero is the updated hyperparameter in the EM method. Here the approximation for the MMM [20] is used in order to update $\boldsymbol{\gamma}$ and $\mathbf{B}$ as follows

$$\gamma_n^{iter+1} = \frac{1}{K}\Delta\boldsymbol{\sigma}_n^{iter}(\mathbf{B}^{iter})^{-1}\left(\Delta\boldsymbol{\sigma}_n^{iter}\right)^T + \left[(\boldsymbol{\gamma}^{iter})^{-1} + \frac{1}{\lambda}\mathbf{J}^T\mathbf{J}\right]^{-1} \tag{6.15}$$

$$\tilde{\mathbf{B}} = \frac{1}{N}\sum_{n=1}^{N}\frac{\Delta\boldsymbol{\sigma}_n^{iter}\left(\Delta\boldsymbol{\sigma}_n^{iter}\right)^T}{\gamma_n^{iter}} + \beta\mathbf{I} \tag{6.16}$$

$$\mathbf{B}^{iter+1} = \frac{\tilde{\mathbf{B}}}{\left\| \tilde{\mathbf{B}} \right\|_F} \tag{6.17}$$

where superscript *iter* indicates iteration number, $(\Delta\boldsymbol{\sigma}_n^{iter})^T \in \mathbb{R}^K$ is the n-th raw of $\Delta\boldsymbol{\sigma}^{iter}$, β is the regularization parameter for the temporal correlation which avoids the overfitting, and $\| \cdot \|_F$ is the Frobenius norm of a matrix. Subsequently, similarly to the update of $\boldsymbol{\gamma}$ and $\mathbf{B}$, λ is updated as follows

$$\lambda^{iter+1} = \frac{1}{MK} \left\| \Delta\mathbf{Z} - \mathbf{J}\Delta\boldsymbol{\sigma}^{iter} \right\|_F^2 + \frac{\lambda^{iter}}{M} \mathrm{Trace}\left[\mathbf{J}\boldsymbol{\gamma}\mathbf{J}^T (\lambda^{iter}\mathbf{I} + \mathbf{J}\boldsymbol{\gamma}\mathbf{J}^T)^{-1} \right] \tag{6.18}$$

where Trace[·] is the trace of a matrix. The iteration is conducted until either the error bound $\delta = \| \Delta\boldsymbol{\sigma}^{iter+1} - \Delta\boldsymbol{\sigma}^{iter} \|_2 / \| \Delta\boldsymbol{\sigma}^{iter+1} \|_2$ reaches its minimum δ^{min} or *iter* reaches the maximum iteration number $iter^{max}$.

6.3. Experimental setup, Protocol, and Conditions

6.3.1. Experimental setup and Protocol

Figure 6.3(a) shows the experimental setup of EIT and bioelectrical impedance analysis (BIA) measurements. The EIT's experimental setup consists of four units: a wearable sensor consisting of sixteen dry electrodes (5 × 10 mm) [15] attached at right calf position, a digital multiplexer (made by Takei lab based on Arduino Due) connected to the wearable sensor by coaxial cables, an impedance analyzer (IM3570, HIOKI, Japan) connected to the digital multiplexer, and a PC including image reconstruction algorithm software. Impedance $\mathbf{Z}$ measured by the impedance analyzer is sent to the PC using a USB cable. The BIA's experimental setup consists of a BIA system and BIA electrodes (two for hands and two for feet) (InBody S10, InBody Japan Inc.) which measures conventional impedance z^{BIA} [7]. It is confirmed by our preliminary tests that EIT and BIA measurements do not interfere with each other even if the electrodes are still attached unless both measurements are conducted at the same time.

Figure 6.3(b) shows the experimental protocol of the prolonged standing and leg elevation in order to induce local-spatiotemporal change (LSTC) in the extracellular fluid (ECF) in subcutaneous adipose tissue (SAT). At the beginning of the experiment, the subject lies down on a reclining bed and conducts the leg elevation of angle φ = 30 degrees in order to reduce the leg swelling affected by prior activities such as exercise and muscle fatigue [29]. During the prolonged standing, the subject stands for 40 minutes without any minor

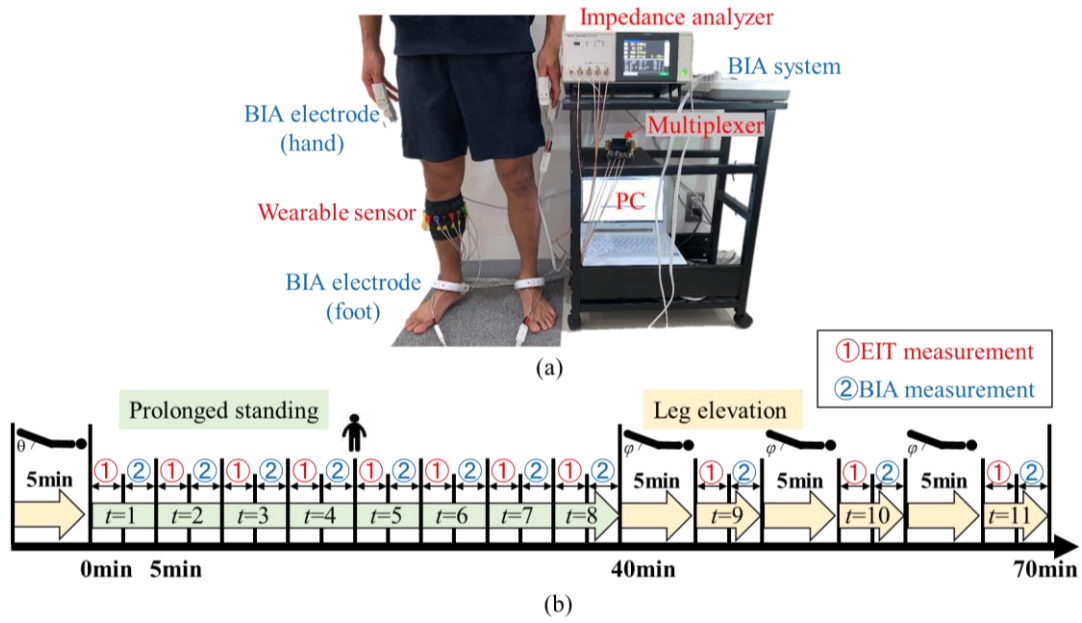

Figure 6.3. (a) Experimental setup of electrical impedance tomography (EIT) and bioelectrical impedance analysis (BIA) measurements and (b) experimental protocol of prolonged standing and leg elevation.

movement in order to induce an increase in ECF volume [14], where EIT and BIA measurements are conducted consecutively, which spend 3 and 2 minutes, respectively. The above process is repeated eight times (k = 1-8: t_k = 5/10/15/20/25/30/35/40 minutes) for each subject. During the leg elevation, the subject elevates the legs for 3 minutes using a reclining bed and then slowly stands up; subsequently, EIT and BIA measurements are conducted consecutively, which spend a total of 8 minutes in order to induce a decrease in ECF volume. The above process is repeated three times (k = 8-11: t_k = 50/60/70 minutes) for each subject.

6.3.2. Experimental methods

In this chapter, 15 healthy subjects (9 males and 6 females, age: 23.1 ± 2.3 years, body mass index: 23.1 ± 4.9 kg/m^2) were volunteered in accordance with the ethical guidelines of the Bioethics Committee in Faculty of Engineering, Chiba University, Japan, and all voluntary subjects gave informed consent. The $\mathbf{Z}$ is measured at various time frames (k = 1-11) with a current I_0=1mA at two frequencies f_1 = 1.6 kHz and f_2 = 4.7 kHz, which are selected considering the current paths that penetrate only the extracellular spaces [7]. The $\mathbf{Z}$ is then used to reconstruct frequency-difference conductivity distribution $\Delta\boldsymbol{\sigma}$ on the FEM mesh generated by NETGEN [30] which is supported by MATLAB R2020a (Mathworks, Natick, MA). In order to quantify the LSTC for evaluating leg edema, spatial-mean conductivity

$\langle \Delta\boldsymbol{\sigma} \rangle^{SAT}$ is calculated in the separated SAT. The z^{BIA} as a comparative parameter is measured by BIA at frequency f^{BIA} = 5kHz in the right leg to represent the ECF [7]. These two parameters are compared by correlation coefficient R where the significance level of the t-test is set to 0.05. Moreover, the normalized values with mean 0 and standard deviation 1 for EIT and BIA measurements, i.e., normalized spatial-mean conductivity $\widetilde{\langle \Delta\boldsymbol{\sigma} \rangle^{SAT}}$ and normalized conventional impedance $\widetilde{z^{BIA}}$ are calculated for evaluating the tendency of the LSTC. In order to obtain great saphenous vein (GSV) position, ultrasound image is acquired using a high-frequncy matrix probe (LOGIQ e Premium, GE Healthcare, Japan) with respect to the EIT electrode position.

The minimum error bound and maximum iteration number for *tvc*SBL-*fd*EIT are set to $\delta^{min} = 1 \times 10^{-2}$ and $iter^{max} = 15$, respectively, which are optimized by trial and error. The influence of these parameters are discussed below. The regularization parameter β for the temporal correlation is set to $\beta = 4$ which considers the noisy $\mathbf{Z}$ [20]. The threshold c is set to the 25th percentile of the temporal standard deviation image $\mathbf{v}$, which is heuristically selected for the robust SAT separation performance based on a priori information about the relationship between $\boldsymbol{\sigma}$ of SAT and other biological tissues such as muscle.

6.4. Experimental Results

6.4.1. Frequency-difference conductivity distribution during prolonged standing and leg elevation

Figure 6.4 shows frequency-difference conductivity distribution $\Delta\boldsymbol{\sigma}$ reconstructed by *tvc*SBL-*fd*EIT which are cropped within the angle between $\theta_0 = 120°$ and $\theta_1 = -150°$ (described in **Figure 6.5(b)**) of 15 subjects' calves during the prolonged standing and leg elevation. Human calf dimensions are based on an x-y-z Cartesian coordinate system with the z-axis along the gravity direction and the x- and y-axes orthogonal to the z-axis. The purple dashed circles indicate the local maximum positions of $\Delta\boldsymbol{\sigma}$ associated with great saphenous vein (GSV) positions. Since local-spatiotemporal change (LSTC) associated with GSV is small and difficult to distinguish in the entire image, the entire circular image is shown only in the

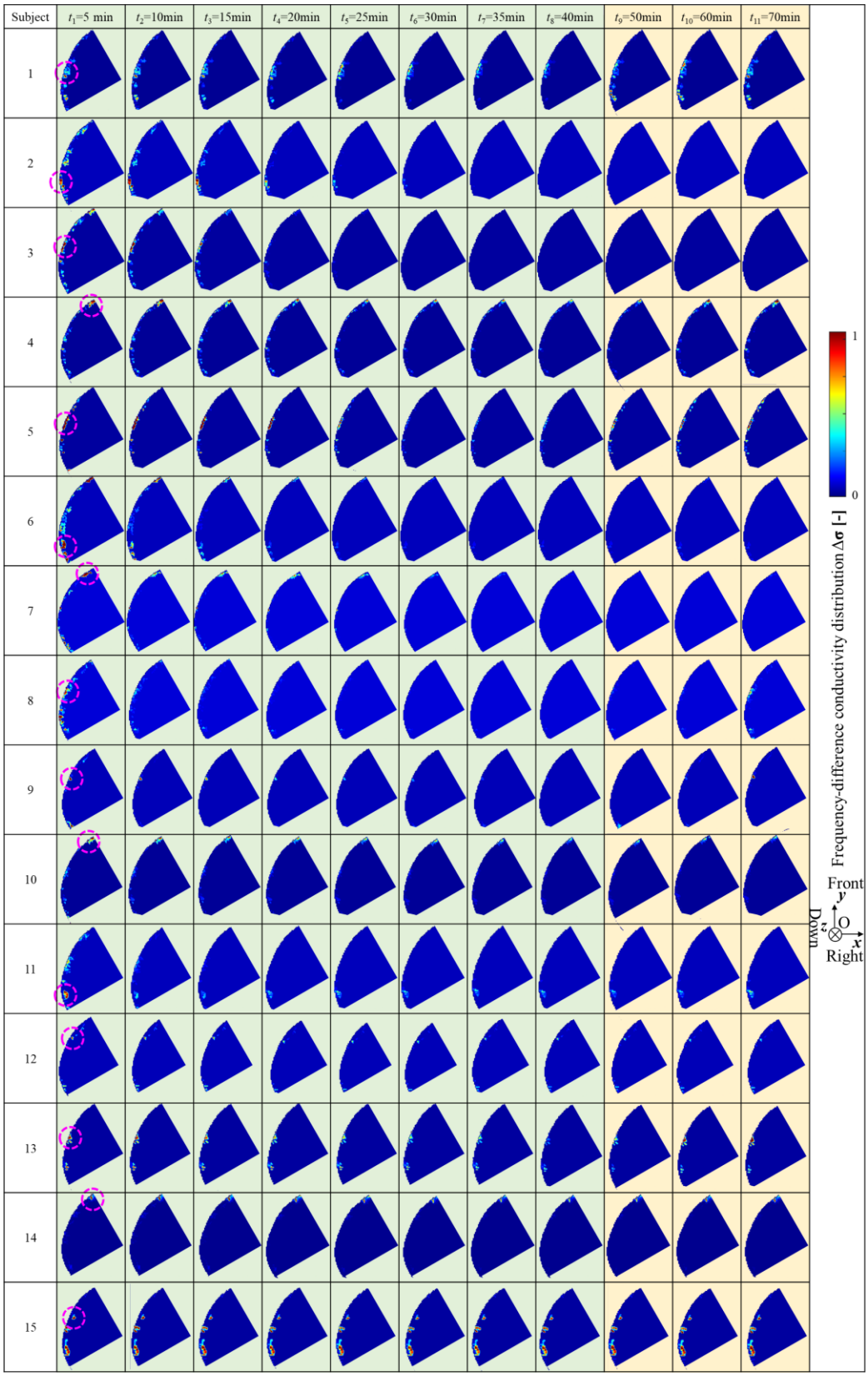

Figure 6.4. Frequency-difference conductivity distribution Δσ of 15 subjects' calves during prolonged standing and leg elevation. Purple dashed circles indicate the local maximum positions of Δσ associated with great

representative example in **Figure 6.5(b)**, and $\Delta\boldsymbol{\sigma}$ are cropped for all 15 subjects in **Figure 6.4**. The angles θ_0 and θ_1 are chosen to emphasize the $\Delta\boldsymbol{\sigma}$ near the GSV positions located on the anterointernal side of the tibia. Although there were some variations in the EIT electrode number at which the GSV was observed for each subject in the ultrasound image, it was located near EIT electrode No.(3)-(5) (data not shown). Therefore, the LSTC in the extracellular fluid (ECF) in the separated subcutaneous adipose tissue (SAT) appears to be accurately monitored by $\Delta\boldsymbol{\sigma}$; namely, the LSTC is decreased during the prolonged standing while the LSTC is increased during the leg elevation. High $\Delta\boldsymbol{\sigma}$ are also observed in locations other than near the GSV, which appears to be either ECF retained by capillaries near relatively large veins or simply reconstruction artifacts. More interestingly, the locations near the GSV show the highest $\Delta\boldsymbol{\sigma}$ in most subjects. **Figure 6.5(a)** shows the cross-section of a typical human calf, **Figure 6.5(b)** shows $\Delta\boldsymbol{\sigma}$ of subject No.12 as a representative, and **Figure 6.5(c)** shows the ultrasound image of the subject below the EIT electrode No.(4). In **Figure 6.5(b)**, the white dashed line indicates the boundary of the separated SAT. In contrast, the red dashed line in **Figure 6.5(c)** indicates the direction from the origin toward the local maximum position, whose angle $\theta^{EIT}{}_G = 150°$ is quantitatively the same as the angle $\theta^{US}{}_G = 150°$ on the red dashed line which indicates the direction from the origin toward the GSV position in the ultrasound image. From these figures, the LSTC positions in $\Delta\boldsymbol{\sigma}$ are shown in the separated SAT, not in the muscle compartments or bones, which is qualitatively similar to the cross-sectional SAT of a typical human calf and the ultrasound image, where non-zero values are preserved inhomogeneously; especially, the local maximum position of $\Delta\boldsymbol{\sigma}$ indicated as the

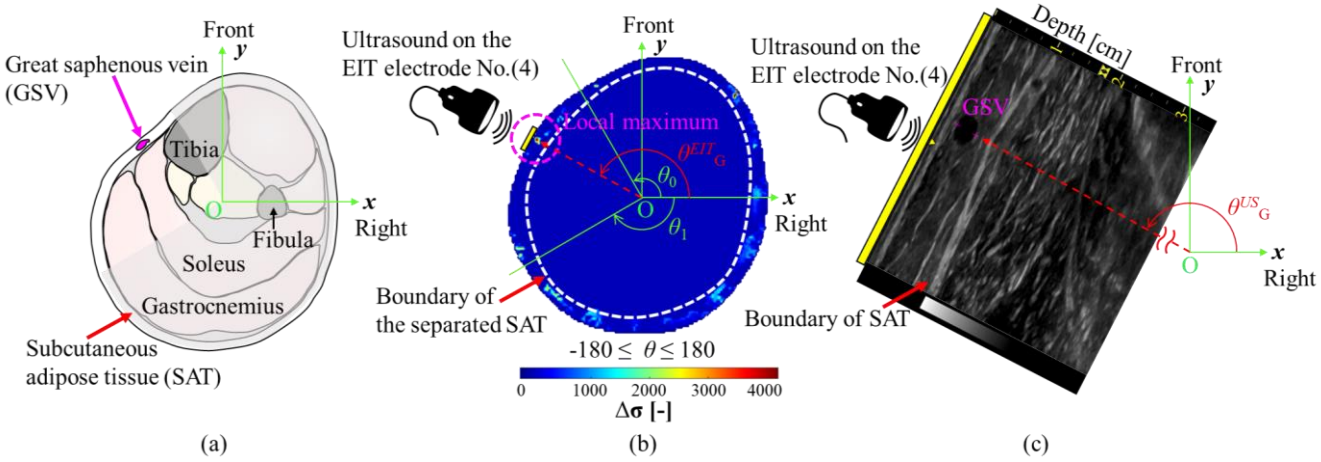

Figure 6.5. (a) Cross-section of a typical human calf, (b) frequency-difference conductivity distribution $\Delta\sigma$ of subject No.12 in the case of t_1 = 5 minutes as a representative, and (c) ultrasound image of subject No.12 below EIT electrode No.(4).

purple dashed circle is associated with the GSV position. The image interpretation is discussed in more detail in the next section.

6.4.2. Spatial-mean conductivity

Figure 6.6 shows normalized spatial-mean conductivity $\widetilde{\langle \Delta\boldsymbol{\sigma} \rangle^{SAT}}$ in the separated SAT and normalized conventional impedance $\widetilde{z^{BIA}}$ during the prolonged standing and leg elevation. $\widetilde{\langle \Delta\boldsymbol{\sigma} \rangle^{SAT}}$ and $\widetilde{z^{BIA}}$ are decreased during the prolonged standing while $\widetilde{\langle \Delta\boldsymbol{\sigma} \rangle^{SAT}}$ and $\widetilde{z^{BIA}}$ are increased during the leg elevation. Even though the standard deviation of $\widetilde{\langle \Delta\boldsymbol{\sigma} \rangle^{SAT}}$ is relatively higher than that of $\widetilde{z^{BIA}}$, $\widetilde{\langle \Delta\boldsymbol{\sigma} \rangle^{SAT}}$ represents well the tendency of ECF.

Figure 6.7 shows the correlation between spatial-mean conductivity $\langle \Delta\boldsymbol{\sigma} \rangle^{\mathrm{SAT}}$ in the separated SAT and conventional impedance $\mathrm{z}^{\mathrm{BIA}}$ of 15 subjects' calves where the correlation coefficient R between two parameters and the p-value are also provided. $\Delta\boldsymbol{\sigma}$ and z^{BIA} have a strong positive correlation, which scores $0.715 < R < 0.957$ ($p < 0.05$). Therefore, considering that the LSTC shows a similar tendency to the temporal change in z^{BIA}, and furthermore, that the LSTC is visualized, which is not possible by BIA, the advantage of *tvc*SBL-*fd*EIT is suggested. Regarding the respective value ranges, while $\mathrm{z}^{\mathrm{BIA}}$ ranges from 170 to 340[Ω], $\langle \Delta\boldsymbol{\sigma} \rangle^{SAT}$ ranges from 10 to 1400[-]. Despite the fundamental difference that BIA mainly evaluates static status based on absolute values while EIT mainly evaluates dynamic trends based on relative values, the variation in $\langle \Delta\boldsymbol{\sigma} \rangle^{SAT}$ is larger than that of z^{BIA}, with a difference of up to approximately two orders of magnitude. This appears to be due to the higher sensitivity of *tvc*SBL-*fd*EIT not only to the LSTC but also to errors depending on electrode contact and skin conditions.

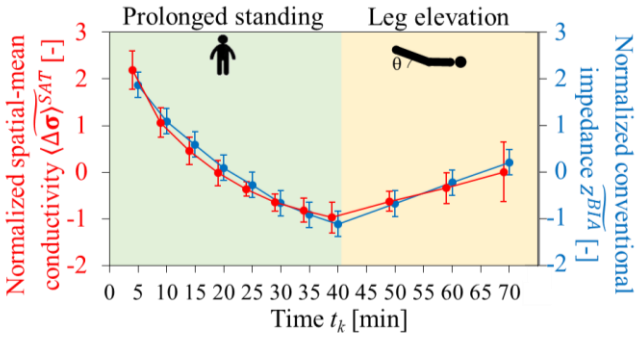

Figure 6.6. Normalized spatial-mean conductivity $\widetilde{\langle \Delta\boldsymbol{\sigma} \rangle^{SAT}}$ and normalized conventional impedance $\widetilde{\mathrm{z}^{BIA}}$ of 15 subjects' calves.

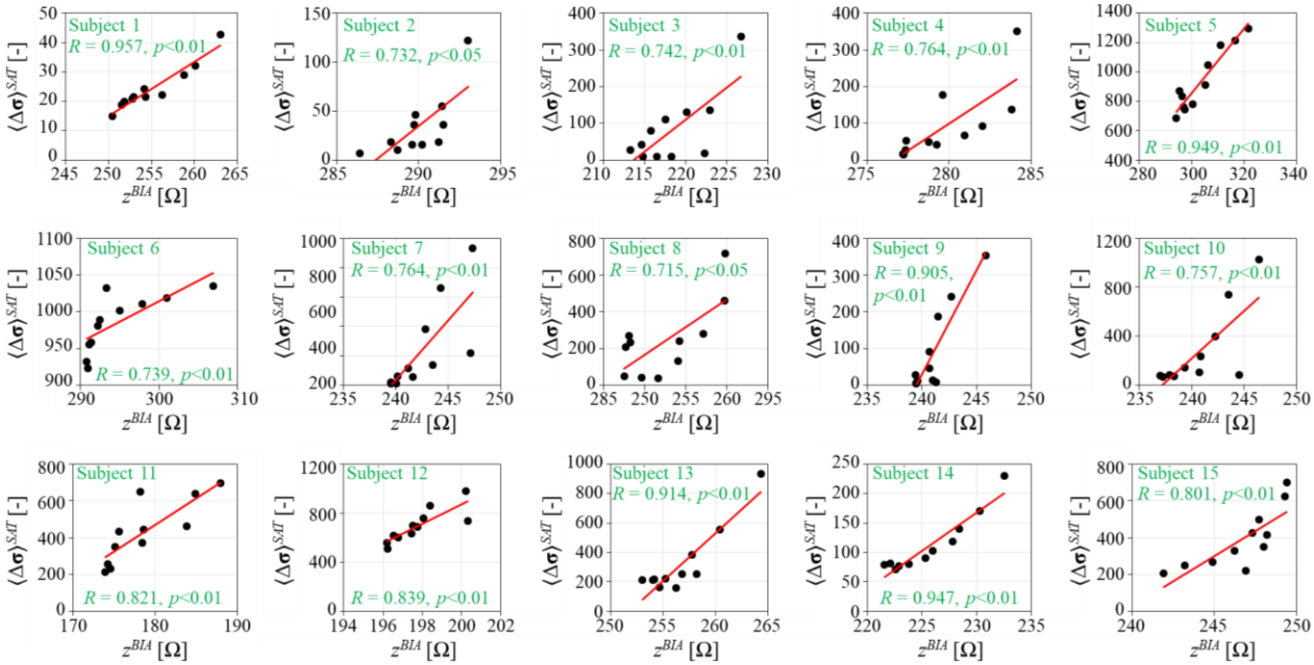

Figure 6.7. Correlation between spatial-mean conductivity $\langle\Delta\sigma\rangle^{SAT}$ and conventional impedance z^{BIA} of 15 subjects' calves.

6.5. Discussions

6.5.1. Frequency-dependency of conductivity distribution

The reason for the occurrence of the local-spatiotemporal change (LSTC) in frequency-difference conductivity distribution $\Delta\boldsymbol{\sigma}$ in the separated subcutaneous adipose tissue (SAT) is discussed. During prolonged standing, hydrostatic pressure in lower leg is increased due to the gravitational force on blood, which increases the capillary filtration into the extracellular spaces of tissues such as SAT [31]. Simultaneously, reabsorption in the extracellular fluid (ECF) is decreased [32] due to the increased osmotic pressure of extracellular spaces, which depends mainly on sodium ion concentration [33]. Therefore, the following proportional relationship in ratio values is derived [34]

$$\frac{L^{ECF}}{L^{ICF}} \propto \frac{\mathrm{Na}^{+ECF}}{\mathrm{Na}^{+ICF}} \tag{6.19}$$

where L^{ECF} and L^{ICF} are the volumes of ECF and intracellular fluid (ICF), respectively, and Na^{+ECF} and Na^{+ICF} are the sodium ion concentration in ECF and ICF, respectively. Conductivity distribution $\boldsymbol{\sigma}$ of NaCl solution, the main component in ECF, is frequency-independent in frequency $f < 1$ MHz [16] while $\boldsymbol{\sigma}$ of protein solution, the subcomponent in ECF, is frequency-dependent at the low frequency used in this study [17]. Moreover, impedance $\mathbf{Z}$ measured at a low frequency below $f = 5$kHz represents ECF [7]. Since protein

concentration is kept constant in healthy persons during prolonged standing, the normalized spatial-mean conductivity $\langle \Delta\boldsymbol{\sigma} \rangle^{SAT}$ in **Figure 6.6** is associated with the decreased frequency-dependency of $\boldsymbol{\sigma}$ in ECF caused by the increased Na^{+ECF}.

According to the above explanation, the following relationship in frequency-difference of $\boldsymbol{\sigma}$ is derived in the case of healthy persons

$$\frac{1}{\langle \Delta\boldsymbol{\sigma} \rangle^{SAT}} \propto \frac{L^{ECF}}{L^{ICF}} \propto \frac{Na^{+ECF}}{Na^{+ICF}} \tag{6.20}$$

According to Equation (6.20), the volume change in ECF ΔL^{ECF} in the right leg during the prolonged standing and leg elevation is estimated from spatial-mean conductivity $\langle \Delta\boldsymbol{\sigma} \rangle^{SAT}$ as follows

$$\Delta L_k^{ECF} = \left| \frac{\langle \Delta\boldsymbol{\sigma} \rangle_k^{SAT} - \langle \Delta\boldsymbol{\sigma} \rangle_1^{SAT}}{\langle \Delta\boldsymbol{\sigma} \rangle_1^{SAT}} \right| \times w \times \rho^{TBF} \times \rho^{ECF/TBF} \times \rho^{RL} [l] \tag{6.21}$$

where ΔL^{ECF} and $\langle \Delta\boldsymbol{\sigma} \rangle^{SAT}$ at the k-th time frame are considered, w is subject's body weight, $\rho^{TBF} = 0.6$ [7] is the ratio of total body fluid (TBF) to total body weight, $\rho^{TBF/ECF} = 0.29$ [35] is the ratio of ECF to TBF, and $\rho^{RL} = 0.1$ [36] is the ratio of right leg to the whole body. **Figure 6.8** shows ΔL^{ECF} in the right leg of 15 subjects, which is increased during the prolonged standing while ΔL^{ECF} is decreased during the leg elevation. Even though $\langle \Delta\boldsymbol{\sigma} \rangle^{SAT}$ represents only the LSTC, ΔL^{ECF} in **Figure 6.8** is seemingly reasonable based on the assumption that the tendency of $\langle \Delta\boldsymbol{\sigma} \rangle^{SAT}$ is consistent with ΔL^{ECF} in the whole right leg. However, ΔL^{ECF} is ranged from 0.0019 to 1.45 [l] which is probably overestimated for some subjects considering the range of the literature data [37]; therefore, compensative parameters for Equation (6.21) needs to be investigated by considering other physiological conditions such as relative leg lengths and fat-free mass (FFM) density [38].

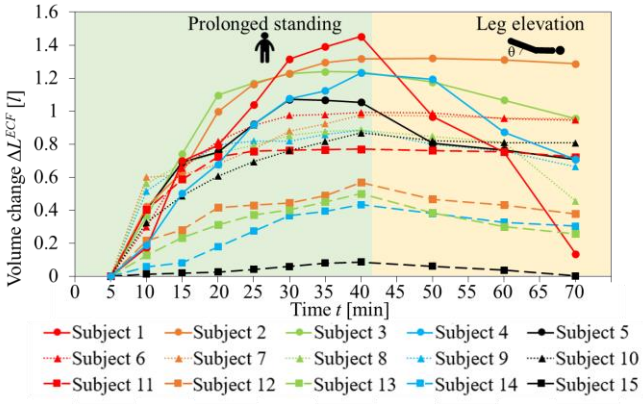

Figure 6.8. Volume change ΔL^{ECF} in right leg of 15 subjects during prolonged standing and leg elevation.

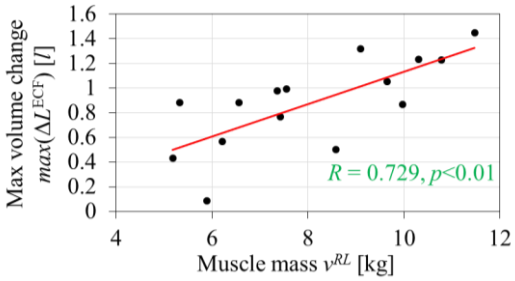

Figure 6.9. Correlation between max volume change $max(\Delta L^{ECF})$ and muscle mass in right leg v^{RL} of 15 subjects.

Subsequently, the range of ΔL^{ECF} is investigated. **Figure 6.9** shows the correlation between max volume change in ECF $max(\Delta L^{ECF})$, i.e., ΔL^{ECF} at $t_8 = 40$ minutes, and muscle mass in right leg v^{RL} measured by bioelectrical impedance analysis (BIA) of 15 subjects where the correlation coefficient R between two parameters and the p-value are also provided. $max(\Delta L^{ECF})$ and v^{RL} have a strong positive correlation, which scores $R = 0.729$ ($p < 0.01$). Since blood flow change is correlated with muscle mass, $max(\Delta L^{ECF})$ due to the increased intravascular pressure is also correlated with muscle mass. However, it must be paid attention that ΔL^{ECF} and v^{RL} are both related to body weight w; thus, other parameters need to be investigated to understand better the differences in $max(\Delta L^{ECF})$ between subjects.

6.5.2. Local maximum position of $\Delta\boldsymbol{\sigma}$

The reason why the local maximum position of $\Delta\boldsymbol{\sigma}$ (purple dashed circle in **Figure 6.4**) is associated with great saphenous vein (GSV) position is discussed. The global minima of the SBL framework are always the sparsest [20] with the aid of the prior variance vector $\boldsymbol{\gamma}$ related to the sparsity that controls individual elements of $\Delta\boldsymbol{\sigma}$. It indicates that the local minimum is also at least close to the sparsest even in a noisy and ill-posed field like EIT [10]. GSV is located between the superficial and saphenous fascia, whose depth position depends on the subcutaneous tissue thickness. Moreover, GSV plays an essential role in returning blood from subcutaneous tissue of leg to heart, which is associated with increased ECF volume/concentration during prolonged standing. Although several large local maxima are observed in **Figure 6.5**, the local maximum position of $\Delta\boldsymbol{\sigma}$ is inferred to be related to ECF diffused from capillaries near the GSV, even given the low resolution of the EIT image. Therefore, *tvc*SBL-*fd*EIT is able to extract the temporal correlation of the $\Delta\boldsymbol{\sigma}$ in the separated SAT, where non-zero values with the significant LSTC near the GSV position are monitored.

6.5.3. Evaluation of *tvc*SBL-*fd*EIT (Simple geometry)

6.5.3.1. Simulation method

As a comparison method for the two types of the SBL-EIT, which are the proposed one with SAT separation in step 2 and the conventional one without SAT separation in step 2, the conventional iterative Gauss-Newton method is considered [39]

$$\Delta\boldsymbol{\sigma}_k^{iter+1} = \Delta\boldsymbol{\sigma}_k^{iter} + (\mathbf{J}^T\mathbf{J} + \eta\cdot\mathbf{I})^{-1}\mathbf{J}^T(\Delta\mathbf{Z}_k - \mathbf{J}\Delta\boldsymbol{\sigma}_k^{iter}) \tag{6.22}$$

where $\Delta\boldsymbol{\sigma}^{iter}{}_k$ is the $\Delta\boldsymbol{\sigma}$ at time t_k in the *iter*-th iteration, $\mathbf{I}\in\mathbb{R}^{N\times N}$ is the identity matrix, and η is the regularization parameter. Since the simple condition is considered here, the impedance $\mathbf{Z}$ is normalized in a manner of time-difference EIT (*td*EIT) only in this section as follows

$$\Delta\mathbf{Z}_k = (\mathbf{Z}_k - \mathbf{Z}_0)\oslash\mathbf{Z}_0 = \mathbf{J}\Delta\boldsymbol{\sigma}_k + \boldsymbol{\varepsilon}_k \tag{6.23}$$

The measured impedance $\Delta\mathbf{Z}_k$ is calculated by the finite element method (FEM) using MATLAB R2020a (Mathworks, Natick, MA); its FEM elements are created by NETGEN [30], the element number for the forward and inverse problem is 2946 and 4560, respectively.

6.5.3.2. Simulation condition

Figure 6.10(a) shows a simple geometry of a human calf, consisting of a great saphenous vein (GSV), subcutaneous adipose tissue (SAT), and muscle. In order to simulate the two types of physiological edema progression, the conductivity value $\boldsymbol{\sigma}$ of each compartment is varied over time from t_0 to t_6 as follows. **Figure 6.10(b)** shows the lymphedema (LE) simulation condition as Condition 1, where only the $\boldsymbol{\sigma}$ of GSV is time-varying at a constant change rate a^{GSV}, while the $\boldsymbol{\sigma}$ of SAT and muscle are not time-varying. **Figure 6.10(c)** shows the venous edema (VE) simulation condition as Condition 2, where the $\boldsymbol{\sigma}$ of GSV and muscle are time-varying at a constant rate of change $a^{GSV} = a^{muscle}$ (= 0.667) and the $\boldsymbol{\sigma}$ of SAT is time-

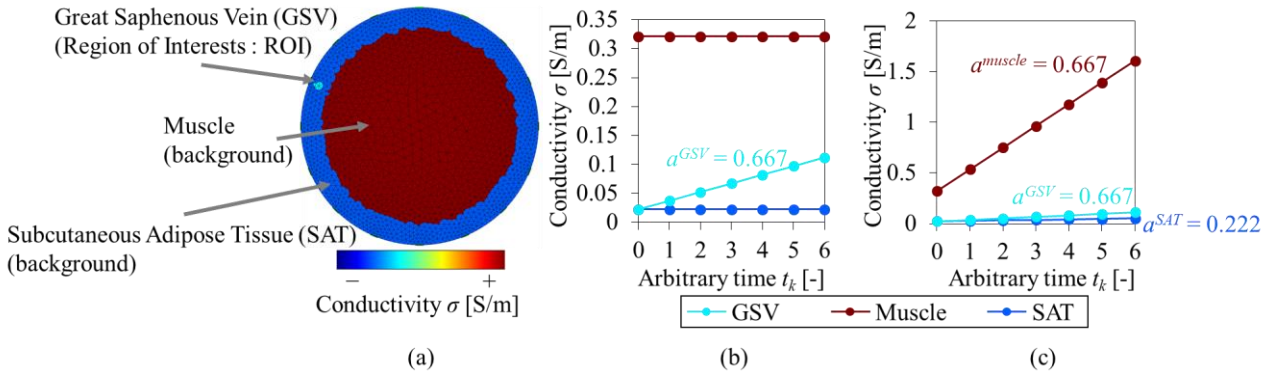

Figure 6.10 Simulation conditions. (a) Simplified simulated image of human calf on axial plane. Conductivity values under conditions simulating (b) lymphedema (LE) and (c) venous edema (VE). †Raw values in (b) and (c) are adapted from reference data [24].

varying at a rate of change a^{SAT} (= 0.222 < a^{GSV}) time of SAT and muscle in the two conditions. The **σ** at initial time t_0 (= 0.022 [S/m] at SAT, = 0.321 [S/m] at muscle) are adapted from reference data [24]. In contrast, the **σ** of GSV at t_0 (= 0.022 [S/m]) is the same as for SAT. As the progression of the **σ** during edema is generally proportional to water content, a^{GSV} was calculated as a^{GSV}= 0.667 from the change in water content in the calf during 60 min of standing in the experiment of Chester *et al.*, 2002 [37]. Furthermore, since SAT changes slower than GSV, a^{SAT} is set asa a^{SAT}= a^{GSV}/3.

The sensitivity matrix **J** is calculated under homogeneous conditions, i.e. **σ** = 1.0 [S/m]. The injected current I_0 and frequency f are set to I_0 = 1 mA and f = 1 kHz, respectively, with which the adjacent injection pattern was applied. The threshold c in Equation (6.14) is set to the median of the time standard deviation image **v**, and the initial values of λ, **γ** and **B** are λ = 0.01, **γ** = $[1,..., 1,..., 1]^T \in \mathbb{R}^N$, and **B** = **I** $\in \mathbb{R}^{K \times K}$, respectively. Gaussian noise is added to **Z** in order to obtain a signal-to-noise ratio (SNR) of 40 dB. As for the proposed *tvc*SBL-EIT (with SAT separation in step 3), the conventional SBL-EIT (without SAT separation in step 3), and the conventional Gauss-Newton method (Equation (6.21)), the maximum iteration number is set as $iter^{max}$ = 10 under the two conditions. The regularization parameter η in the Gauss-Newton method was selected using the L-curve method with $\eta = 4.17 \times 10^{-6}$ (LE simulation condition) and $\eta = 1.80 \times 10^{-5}$ (VE simulation condition.

6.5.3.3. Simulation results

Figure 6.11 shows the conductivity change Δ**σ** reconstructed by the *tvc*SBL-EIT (with SAT separation in step 2), the conventional SBL-EIT (without SAT separation in step 2), and the conventional Gauss-Newton method as well as the true image. The dotted line in **Figure 6.11(b)** indicates the position of the GSV in the original image. In condition 1 (**Figure 6.10(a)**), the Gauss-Newton method was able to image the temporal changes in Δ**σ** near the GSV. Still, the image was blurred compared to the true image. Furthermore, a ringing artifact [40] with large negative values surrounding the GSV was also identified. On the other hand, the two SBL-EIT image reconstruction algorithms were able to extract only local Δ**σ**. Since SAT and muscles as the background did not change over time, the clear image was reconstructed with or without step 2. In other words, for a simple problem such as Condition 1, it was easy to cancel the background influence and extract only the local changes as the target GSV, even if only time differences were taken, and the SAT separation in Step 2 did not particularly affect the image reconstruction performance.

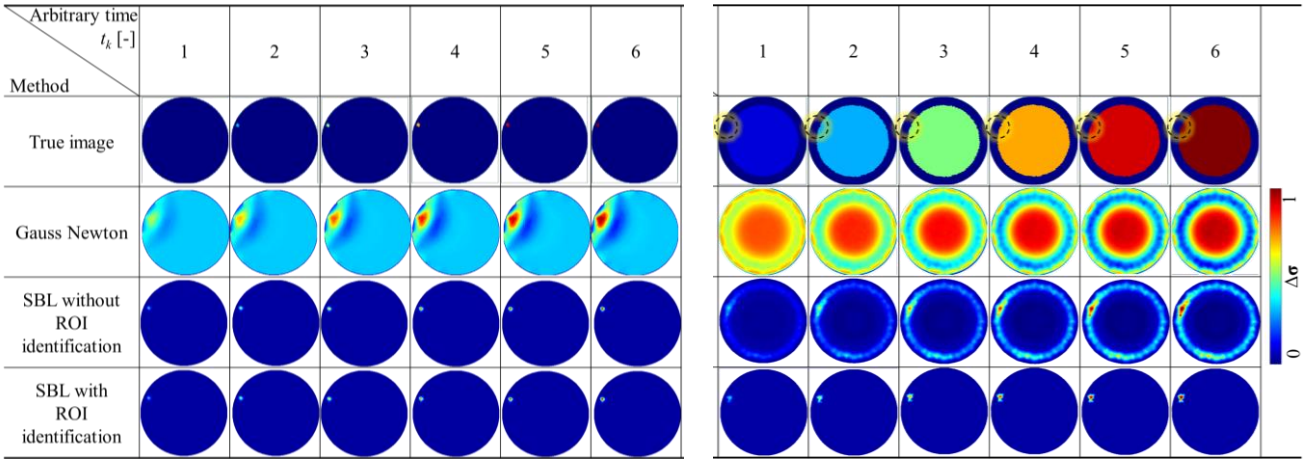

(a) (b)

Figure 6.11 Conductivity change Δσ under conditions simulating (a) lymphedema (LE) and (b) venous edema (VE) (b). Dashed lines indicate the position of GSV. Top row shows true images and the other rows show images reconstructed by various methods, whereas each column shows images corresponding to various times.

Next, in condition 2 (**Figure 6.10(b)**), the Gauss-Newton method was able to image the boundary between the SAT and the muscle but not the temporal $\Delta\boldsymbol{\sigma}$ near the GSV, which is because the time variation of the whole region causes the negative effect that the background could not be canceled by only taking a simple time difference between initial time t_0 and time t_k without time correlation or sparsity hypothesis. On the other hand, the conventional SBL-EIT without step 2 was able to image the $\Delta\boldsymbol{\sigma}$ in the SAT and, moreover, to extract the area around the GSV in the SAT where the time variation was particularly large. However, circular artifacts were produced due to the temporal changes influenced by the SAT. The *tvc*SBL-EIT with step 2 was only able to extract $\Delta\boldsymbol{\sigma}$ near the GSV. Although the entire region was time-varying, SAT separation clearly extracted only the $\Delta\boldsymbol{\sigma}$ near the GSV, where the "local-spatio" and "local-temporal" changes were particularly large in the SAT.

6.5.4. Evaluation of *tvc*SBL-*fd*EIT (Complex geometry)

6.5.4.1. Simulation method

In order to quantitatively evaluate the proposed method under the unstable-background fields with complex geometry where both the GSV as the region of interest and SAT as the background are frequency-dependent, $\Delta\boldsymbol{\sigma}$ is reconstructed by the *tvc*SBL-*fd*EIT, SBL-*fd*EIT (without SAT separation in Equation (6.14)), and the iterative Gauss-Newton algorithm which is often used in the biomedical EIT. The Gauss-Newton algorithm is computed with the Tikhonov regularization [39]

$$\Delta\boldsymbol{\sigma}_k^{iter+1} = \Delta\boldsymbol{\sigma}_k^{iter} + (\mathbf{J}^T\mathbf{J} + \eta\cdot\mathbf{I})^{-1}\mathbf{J}^T(\Delta\mathbf{Z}_k - \mathbf{J}\Delta\boldsymbol{\sigma}_k^{iter}) \quad (6.22)$$

Re-posted

where $\Delta\boldsymbol{\sigma}_k^{iter}$ is the conductivity distribution at the *iter*-th iteration step at the k-th arbitrary time ($1 \leq k \leq 3$) and η=0.01 is the regularization parameter. The measured impedance $\Delta\mathbf{Z}_k$ is calculated by FEM computations similar to section 6.3.2., where the element number of the forward and inverse problem are 3219 and 4261, respectively. The impedance **Z** is measured at two frequencies f_1 = 1.6 kHz and f_2 = 4.7 kHz, with SNR = 40 dB due to the additive Gaussian noise. **Figure 6.12(a)** shows an example of a human calf including muscle, SAT, and GSV with the same boundary as the one used in **Figure 6.5(b)**, and **Figure 6.12(b)** shows corresponding conductivity values σ to simulate the unstable-background fields. Under simple unstable-background fields, only the σ of GSV is assumed to be time-dependent, while the σ of SAT and muscle are assumed to be time-independent and, furthermore, the σ of muscle is assumed to be frequency-independent as well. Even if the muscle and SAT are time-independent, the reconstruction of the local-spatiotemporal change (LSTC) due to the effect of very small GSV is challenging under the frequency-dependent SAT. The σ of SAT and muscle are adapted from [24] at all frequencies, whereas the σ of GSV at frequency f_1 is two, three, and four times the σ of SAT at t_1-th, t_2-th, and t_3-th arbitrary time, respectively. The σ of GSV at frequency f_2 is adjusted to achieve $\Delta\sigma_k=(\sigma_{k,f2}-\sigma_{k,f1})+(k-1)\times(\sigma_{1,f2}-\sigma_{1,f1})\times(a^{GSV})^{k-1}$, with which a^{GSV}=0.905 is estimated from the experimental data during the prolonged standing in **Figure 6.6**. This reflects the decreased frequency-dependency of **σ** in ECF caused by the increased Na^{+ECF} near the GSV, i.e., σ_k increases temporally, whereas $\Delta\sigma_k$ decreases temporally. The hyperparameters in SBL algorithms are set to the regularization parameter β = 4 and the minimum error bound $\delta^{min} = 1 \times 10^{-5}$. The threshold c for *tvc*SBL-*fd*EIT is set to the 75th percentile of the temporal standard deviation image **v** with higher values being preserved, which is different from Equation (6.14). This c should again be optimized

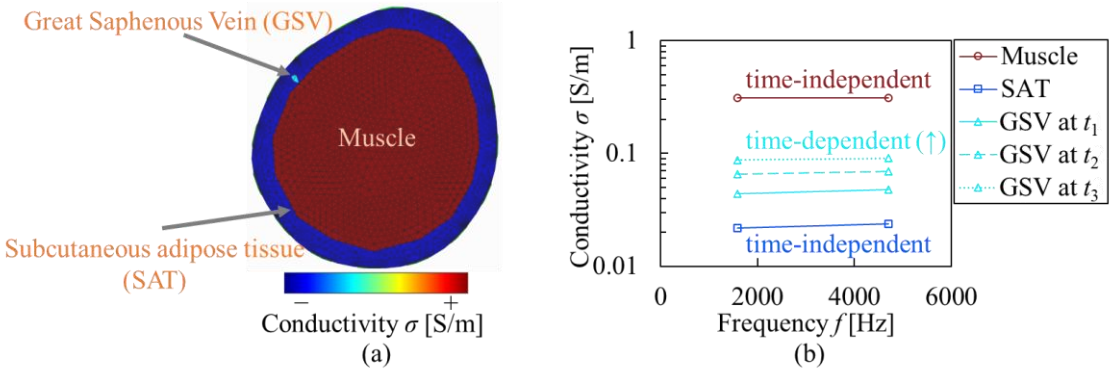

Figure 6.12. (a) Human calf on axial-plane including muscle, SAT, and GSV. (b) Conductivity values under conditions simulating unstable-background fields. †Raw values are adapted from reference data [24].

heuristically for each application since it is one of the key parameters influencing the reconstruction result significantly. For instance, the LSTC of the target is vanished by inappropriate c. The maximum iteration number $iter^{max}$ for all algorithms is set to $iter^{max} = 50$ in order to examine the change for various iteration numbers by three metrics which are 1) the temporal-mean localization error $<LE>$, 2) the spectral error SE, and 3) the image noise IN [41]

$$< LE >= \frac{1}{K}\sum_{k=1}^{K}\left|\frac{r_k - r^{true}}{r^{true}}\right| \tag{6.24}$$

$$SE = \sqrt{\frac{1}{K}\sum_{k=1}^{K}\left(< \Delta\tilde{\boldsymbol{\sigma}}_k >^{perturb} - < \Delta\tilde{\boldsymbol{\sigma}}_k >^{true}\right)^2} \tag{6.25}$$

$$< IN >= \frac{1}{K}\sum_{k=1}^{K}\frac{std(\mathbf{x}_k)}{< \Delta\boldsymbol{\sigma}_k >^{perturb}} \tag{6.26}$$

where r_k is the distance between the origin and the center of gravity of the reconstructed perturbation $\Delta\boldsymbol{\sigma}_k^{perturb}$, $\langle\Delta\tilde{\boldsymbol{\sigma}}_k\rangle^{perturb}$ is the normalized value with mean 0 and standard deviation 1 of the spatial-mean conductivity $<\Delta\boldsymbol{\sigma}_k>^{perturb}$ at the k-th arbitrary time within the $\Delta\boldsymbol{\sigma}_k^{perturb}$, $std(\cdot)$ is the symbol of the standard deviation, and $\mathbf{x}_k$ is the conductivity distribution not belonging to the $\Delta\boldsymbol{\sigma}_k^{perturb}$. Here the $\Delta\boldsymbol{\sigma}_k^{perturb}$ is defined as the connected pixels with conductivity distribution higher than half of the global maxima. The superscripts *true* indicate the true value of each metric. In ideal conditions, the value of $<LE>$, SE, and IN are 0.

6.5.4.2. Simulation results

Figure 6.13(a) and **(c)** show the $\Delta\boldsymbol{\sigma}$ at $iter = 15$ reconstructed by each algorithm under the unstable-background fields and the corresponding normalized spatial-mean conductivity $\langle\Delta\tilde{\boldsymbol{\sigma}}_k\rangle^{perturb}$, respectively. **Figure 6.13(b)** shows the ideal reconstruction image. Moreover, Fig. 11(d) shows $<LE>$, SE, and IN of each algorithm. Since the reconstruction performance does not vary with iteration number significantly, as described below, the $\Delta\boldsymbol{\sigma}$ at $iter = 15$ is shown; however, the appropriate iteration number varies the different conditions and should be considered. While the reconstructed perturbation $\Delta\boldsymbol{\sigma}_k^{perturb}$ due to the presence of GSV is distinguished by SBL algorithms, the Gauss-Newton algorithm is not able to show the $\Delta\boldsymbol{\sigma}_k^{perturb}$ distinctly and suffers from the artifacts. Moreover, the $\langle\Delta\tilde{\boldsymbol{\sigma}}_k\rangle^{perturb}$ is the farthest from the ground truth among the algorithms. The Gauss-Newton algorithm simply takes frequency differences without using temporal correlation or sparsity, therefore unable to cancel the influence of the unstable-background fields. On the other hand, in the SBL

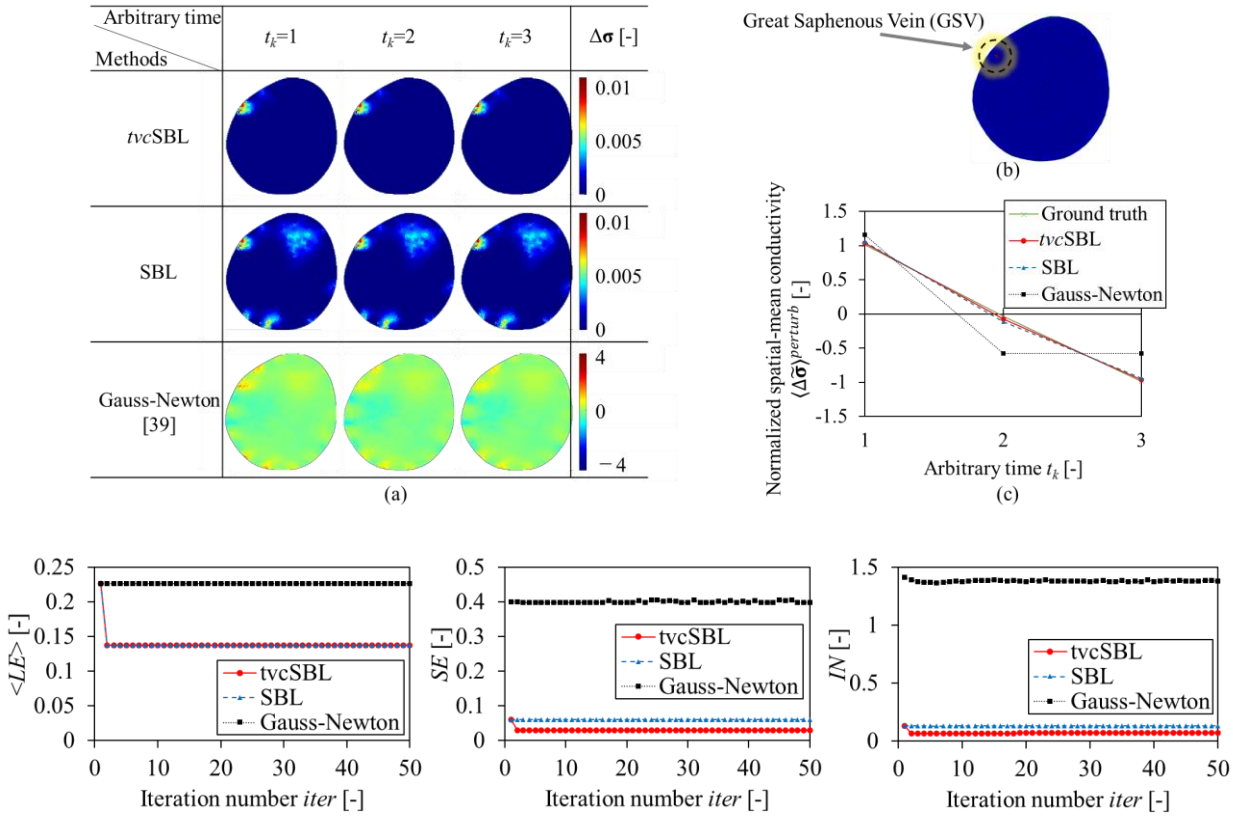

Figure 6.13. (a) Frequency-difference conductivity distribution Δσ of numerical simulation by *tvc*SBL-*fd*EIT, SBL-*fd*EIT, and Gauss-Newton algorithm under the unstable-background fields. (b) Ideal reconstruction image. (c) Normalized spatial-mean conductivity $\langle\Delta\tilde{\sigma}_k\rangle^{perturb}$ of each algorithm and ground truth. (d) Temporal-mean localization error <*LE*>, spectral error *SE*, and image noise *IN* of each algorithm.

algorithms, the $\Delta\sigma_k^{perturb}$ is clearly distinguished at the correct position. Regarding the $\langle\Delta\tilde{\sigma}_k\rangle^{perturb}$ in **Figure 6.13(c)**, even though the *tvc*SBL-*fd*EIT is slightly closer to the ground truth than the SBL-*fd*EIT, both estimates the spectral well. However, the SBL-*fd*EIT shows the artifacts as well as the $\Delta\sigma_k^{perturb}$, which is probably due to the unstable-background fields. This phenomenon highlights the advantage of the *tvc*SBL-*fd*EIT with the aid of SAT separation by time variation constraint.

Three metrics by all algorithms are largely independent of the iteration numbers, with the SBL algorithms performing better than the Gauss-Newton algorithm. The temporal-mean localization error <*LE*> is same by the *tvc*SBL-*fd*EIT and the SBL-*fd*EIT, which scores <*LE*>=0.139 ± 0.012. For GSV localization, only *iter*=2 is sufficient under this condition by both algorithms. The spectral error *SE* is 0.031 ± 0.004 and 0.061 ± 0.001 by the *tvc*SBL-*fd*EIT and the SBL-*fd*EIT, respectively, which indicates the *tvc*SBL-*fd*EIT estimates the

temporal change of frequency-difference better due the improved noise robustness by the SAT separation. The image noise *IN* is 0.072 ± 0.009 and 0.132 ± 0.001 by the *tvc*SBL-*fd*EIT and the SBL-*fd*EIT, respectively. Similarly to the result of *SE*, the SAT separation contributes to noise suppression, which is crucial to monitoring the LSTC.

In terms of the reconstruction performance, the minimum error bound δ^{min} should also be considered. In the case of a relatively low measurement noise, a small δ^{min} is preferred, e.g., $\delta^{min} = 1 \times 10^{-5}$ in the simulation; otherwise, the sparsest solution is not obtained. In contrast, noisy measurement requires larger δ^{min}, e.g., $\delta^{min} = 1 \times 10^{-2}$ in the experiment. Furthermore, the various normalizations of impedance **Z** also influence the value range, e.g., our recent ratiometric preprocessing [42] results in different optimum δ^{min}. Therefore, when the SBL algorithms are independent of the iteration numbers, as in this simulation, the optimum δ^{min} gets larger, which should be adjusted by trial and error.

It is worth mentioning that the computation time t^{comp} to reconstruct the $\Delta\boldsymbol{\sigma}$ by the *tvc*SBL-*fd*EIT is 10.9 times faster than t^{comp} by the SBL-*fd*EIT (t^{comp} = 14.76s and 160.43s, respectively) by a PC (DAIV-DGZ510, MouseComputer Co., Ltd.) with 3.6GHz Intel Core i7-7700 CPU and 32 GB RAM. Even though the computational complexity is high mainly due to the column-vectorization of the sensitivity matrix, i.e., $\tilde{\mathbf{J}} = \mathbf{J} \otimes \mathbf{I} \in \mathbb{R}^{MK \times NK}$, the approximation of the original multiple measurement vector (MMM) space instead of blocked column vector (BCV) space [20] contributes to improving the efficiency. More importantly, the SAT separation in the *tvc*SBL-*fd*EIT reduces the elements used in the computation for achieving more efficient computation. The real-time monitoring of the LSTC by further improving the computation efficiency is investigated in future studies.

6.5.5. Impedance variation

Figure 6.14(a) shows the original dataset of impedance used in the reconstruction (subject No.1 as representative). As expected, the impedance **Z** is higher in lower frequency f_1 than in higher frequency f_2. Although the amplitude of **Z** appears to be high and fluctuates, the datasets remain in the tolerable range considering the fact that we used a wearable sensor consisting of dry electrodes.

Moreover, **Figure 6.14(b)** shows the temporal change of the average impedance <**Z**>. It shows the clear trends along with an experimental protocol of prolonged standing and leg elevation. Not only the temporal change but also the local-spatiotemporal change (LSTC) can be investigated using our proposed *tvc*SBL-*fd*EIT,.

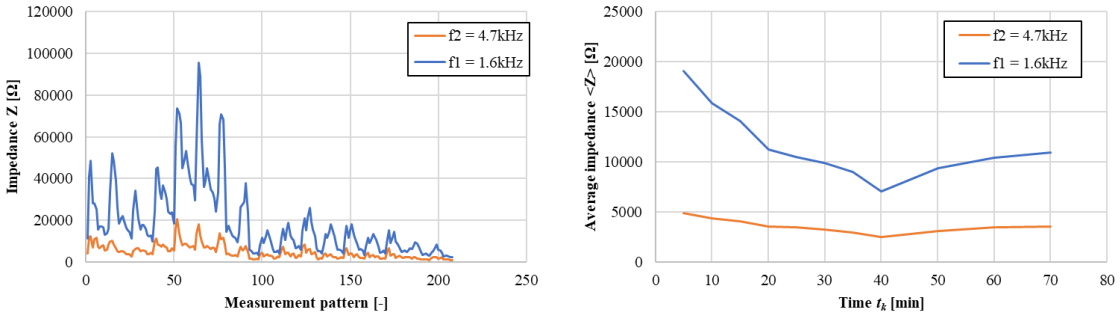

Figure 6.14. Impedance variations at two frequencies over (a) measurement pattern and (b) time.

Regarding a large variation in the correlation between the spatial-mean conductivity $\langle\Delta\boldsymbol{\sigma}\rangle^{SAT}$ and the conventional impedance z^{BIA} as in **Figure 6.7**, no correlation was found in the correlation R (between the spatial-mean conductivity $\langle\Delta\boldsymbol{\sigma}\rangle^{SAT}$ and the conventional impedance z^{BIA}) with the fat thickness (defined as between the top skin and the deep fascia), BMI or lean muscle mass (right leg) (correlation coefficients: 0.158, 0.445, and 0.024, respectively), as shown in **Figure 6.15**.

One expectation is that the susceptibility to edema originates mainly from other causes, such as hormones [43], instead of subcutaneous fat or muscle mass. Furthermore, variations in the respective values due to the different nature of the BIA and EIT electrodes might also need to be considered, which is discussed below. Regarding respective value ranges, as suggested, while z^{BIA} ranges from 170 to 340[Ω], $\langle\Delta\boldsymbol{\sigma}\rangle^{SAT}$ ranges from 10 to 1400[-]. It should be considered that z^{BIA} is an absolute value, whereas $\langle\Delta\boldsymbol{\sigma}\rangle^{SAT}$ reconstructed using the normalized difference in z^{EIT} as an input value, is a relative value. Since EIT needs to solve the inverse problem and is sensitive to many types of errors, difference EIT (e.g., time-difference, frequency-difference) is usually preferred over absolute EIT. Since individual errors vary considerably, EIT is often applied to assess dynamic trends rather than magnitude.

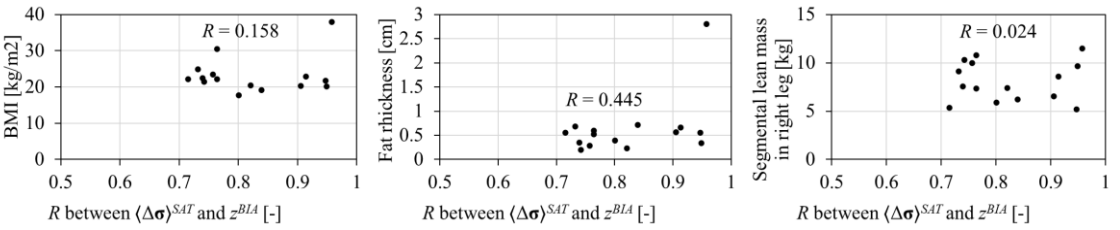

Figure 6.15. Correlation R (between the spatial-mean conductivity $\langle\Delta\boldsymbol{\sigma}\rangle^{SAT}$ and the conventional impedance z^{BIA}) with the fat thickness (defined as between the top skin and the deep fascia), BMI or lean muscle mass (right leg).

Although there remains much significant work to be done to assess the magnitude under various conditions, this is out of our objectives in this chapter since we focus on local-spatiotemporal change (LSTC).

Figure 6.16 shows a box-and-whisker plot of the time variation of the average impedance <**Z**> (averaged over all 208 measurement patterns) for each subject in order to discuss the importance of the magnitude assessment. The temporal variations between subjects and the magnitude itself are quite different, which ranges from 2000 to 25000[Ω] (almost one order of magnitude). As for BIA with flat surface electrode used in this chapter (metallic material-based; InBody S10, InBody Japan Inc.), the body segments are assumed as five cylinders that are not localized, so the sensitivity to LSTC is low, whereas the measurement is stable, so the magnitude is also stable. On the other hand, as for EIT with textiles electrode used in this chapter (silver yarn electrodes attached to a flexible cloth made up of polyester), due to the localization on the electrode layer, it is highly sensitive to 'local' change of interest. However, it is also sensitive to errors depending on contact pressure and skin conditions, so the magnitude is not stable. These temporal variations in EIT measurement will be investigated in the future, e.g., using pressure sensors [44] as a reference to examine the effect of various contact pressures on z^{BIA} and $\langle \Delta \boldsymbol{\sigma} \rangle^{SAT}$, especially in the case of wearable sensors.

6.5.6. Study limitations

Some limitations of this chapter need to be mentioned. The first limitation is the small number of subjects, including 9 males and 6 females. The experiments in this chapter are mainly designed to investigate the performance of *tvc*SBL-*fd*EIT for monitoring LSTC of volume/concentration in ECF. Nevertheless, $\langle \Delta \boldsymbol{\sigma} \rangle^{SAT}$ in the separated SAT had a significantly

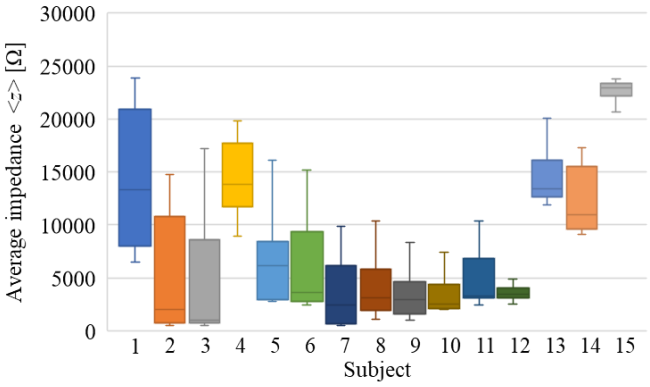

Figure 6.16. Box-and-whisker plot of the time variation of the average impedance <Z> (averaged over all 208 measurement patterns) for each subject.

strong positive correlation with conventional impedance z^{BIA}; therefore, it would be ideal to repeat this chapter with larger groups. Moreover, the indirect effect due to sex and gender differences as well as occupational characteristics will be investigated in future studies since those factors may affect leg edema during prolonged standing [45]. However, more importantly, in this exploratory study, the trend represented by the normalized value, i.e., $\widetilde{\langle \Delta\boldsymbol{\sigma} \rangle^{\mathrm{SAT}}}$, had similarities amond male subjects and female subjects. The second limitation is that only the impedance magnitude value is used in order to avoid the complexity in the sensitivity computation and data acquisition system. For the better understanding of the frequency-dependency, dielectric properties should be incorporated into the analysis [46], which is beyond the scope of this article. A new reconstruction algorithm that enables joint optimization of spectroscopic and tomographic aspects is under consideration in our lab for near future biomedical monitoring modalities.

6.6. Summary

Local-spatiotemporal change (LSTC) in extracellular fluid (ECF) in subcutaneous adipose tissue (SAT) has been monitored for evaluating leg edema by time-variation-constraint sparse Bayesian learning (*tvc*SBL) implemented into frequency-difference electrical impedance tomography (*fd*EIT) (*tvc*SBL-*fd*EIT). This method is qualitatively and quantitatively evaluated by an experimental protocol of prolonged standing and leg elevation. The key findings of this research are:

(1) The *tvc*SBL-*fd*EIT was proposed for monitoring the LSTC by iteratively extracting the temporal correlation of frequency-difference conductivity distribution $\Delta\boldsymbol{\sigma}$ in the SAT separated by the time variation constraint

(2) The proposed *tvc*SBL-*fd*EIT accurately reconstructed $\Delta\boldsymbol{\sigma}$ whose spatial-mean conductivity $\langle \Delta\boldsymbol{\sigma} \rangle^{SAT}$ in the separated SAT had a strong positive correlation with conventional impedance z^{BIA} by bioelectrical impedance analysis (BIA), which scored correlation coefficient $0.715 < R < 0.957$ ($n = 15$, $p < 0.05$)

(3) Frequency-dependency of conductivity distribution $\boldsymbol{\sigma}$ in ECF and the local maximum position of $\Delta\boldsymbol{\sigma}$ were investigated. The frequency-dependency of $\boldsymbol{\sigma}$ was

decreased due to the increase of the sodium ion concentration in ECF in SAT. Moreover, the local maximum position of $\Delta\boldsymbol{\sigma}$ was associated with great saphenous vein (GSV) position, which had a significant LSTC in $\Delta\boldsymbol{\sigma}$. Furthermore, the key parameters of the reconstruction performance under the unstable-background fields are investigated by comparing them to the conventional algorithms.

Appendix. Inference procedure

The inference procedure (Equations (6.8)-(6.11)) is described here, where only the critical information is provided. Given the additive noise model with zero-mean Gaussian distribution as represented in Equations (6.3) and (6.6), from the relationship between the conjugate prior distribution of the Gaussian distribution, in the case where the prior distribution (Equation (6.4)) and noise distribution (Equation (6.6)) are Gaussian, the posterior (Equation (6.9)) is also Gaussian. Therefore, the exponent part of the posterior distribution is calculated as follows

$$\begin{aligned} &-\frac{1}{2}(\Delta\boldsymbol{\sigma}*-\overline{\Delta\boldsymbol{\sigma}*})^T(\boldsymbol{\Sigma}^{post})^{-1}(\Delta\boldsymbol{\sigma}*-\overline{\Delta\boldsymbol{\sigma}*}) \\ &=-\frac{1}{2}(\Delta\boldsymbol{\sigma}*)^T(\boldsymbol{\Sigma}^{post})^{-1}\Delta\boldsymbol{\sigma}*+(\Delta\boldsymbol{\sigma}*)^T(\boldsymbol{\Sigma}^{post})^{-1}\overline{\Delta\boldsymbol{\sigma}*}+const. \end{aligned} \tag{6.a1}$$

where *const.* is the term that is not containing $\Delta\boldsymbol{\sigma}*$. Similarly to Equation (6.a1), the exponent part of Equations (6.8) is calculated as follows

$$\begin{aligned} &-\frac{1}{2}[(\Delta\boldsymbol{\sigma}*)^T(\boldsymbol{\Sigma}^{pre})^{-1}\Delta\boldsymbol{\sigma}*+\frac{1}{\lambda}(\Delta\mathbf{Z}*-\tilde{\mathbf{J}}\Delta\boldsymbol{\sigma}*)^T(\Delta\mathbf{Z}*-\tilde{\mathbf{J}}\Delta\boldsymbol{\sigma}*)] \\ &=-\frac{1}{2}(\Delta\boldsymbol{\sigma}*)^T[(\boldsymbol{\Sigma}^{pre})^{-1}+\frac{1}{\lambda}\tilde{\mathbf{J}}^T\tilde{\mathbf{J}})]\Delta\boldsymbol{\sigma}*+\frac{1}{\lambda}(\Delta\boldsymbol{\sigma}*)^T\tilde{\mathbf{J}}^T\Delta\mathbf{Z}*+const. \end{aligned} \tag{6.a2}$$

which is then compared to Equation (6.a1) in order to acquire the mean vector $\overline{\Delta\boldsymbol{\sigma}*}\in\mathbb{R}^{NK}$ and the posterior covariance matrix $\boldsymbol{\Sigma}^{post}\in\mathbb{R}^{NK\times NK}$ as follows

$$\overline{\Delta\boldsymbol{\sigma}*}=\left[\lambda(\boldsymbol{\Sigma}^{pre})^{-1}+\tilde{\mathbf{J}}^T\tilde{\mathbf{J}}\right]^{-1}\tilde{\mathbf{J}}^T\Delta\mathbf{Z}*=\frac{1}{\lambda}\boldsymbol{\Sigma}^{post}\tilde{\mathbf{J}}^T\Delta\mathbf{Z}* \tag{6.a3}$$

$$\boldsymbol{\Sigma}^{post}=\left[(\boldsymbol{\Sigma}^{pre})^{-1}+\frac{1}{\lambda}\tilde{\mathbf{J}}^T\tilde{\mathbf{J}}\right]^{-1} \tag{6.a4}$$

Equations (6.a3) and (6.a4) are exactly the same as Equations (6.10) and (6.11).

References

[1] B. H. Cornish *et al.*, “Early diagnosis of lymphedema using multiple frequency bioimpedance,” *Lymphology*, vol. 34, no. 1, pp. 2–11, 2001.

[2] L. M. Ebah *et al.*, “Subcutaneous interstitial pressure and volume characteristics in renal impairment associated with edema,” *Kidney Int.*, vol. 84, no. 5, pp. 980–988, 2013, doi: 10.1038/ki.2013.208.

[3] S. K. Das, “Body composition measurement in severe obesity,” *Curr. Opin. Clin. Nutr. Metab. Care*, vol. 8, no. 6, pp. 602–606, 2005, doi: 10.1097/01.mco.0000171122.60665.5f.

[4] K. Aukland and R. K. Reed, “Interstitial-lymphatic mechanisms in the control of extracellular fluid volume,” *Physiol. Rev.*, vol. 73, no. 1, pp. 1–78, 1993.

[5] L. L. Ploutz-Snyder, S. Nyren, T. G. Cooper, E. J. Potchen, and R. A. Meyer, “Different effects of exercise and edema on T2 relaxation in skeletal muscle,” *Magn. Reson. Med.*, vol. 37, no. 5, pp. 676–682, 1997, doi: 10.1002/mrm.1910370509.

[6] M. Essig *et al.*, “Cardiovascular remodelling and extracellular fluid excess in early stages of chronic kidney disease,” *Nephrol. Dial. Transplant.*, vol. 23, no. 1, pp. 239–248, 2008, doi: 10.1093/ndt/gfm542.

[7] S. F. Khalil, M. S. Mohktar, and F. Ibrahim, “The theory and fundamentals of bioimpedance analysis in clinical status monitoring and diagnosis of diseases,” *Sensors (Switzerland)*, vol. 14, no. 6, pp. 10895–10928, 2014, doi: 10.3390/s140610895.

[8] M. Y. Jaffrin and H. Morel, “Body fluid volumes measurements by impedance: A review of bioimpedance spectroscopy (BIS) and bioimpedance analysis (BIA) methods,” *Med. Eng. Phys.*, vol. 30, no. 10, pp. 1257–1269, 2008, doi: 10.1016/j.medengphy.2008.06.009.

[9] J. Yao and M. Takei, “Application of Process Tomography to Multiphase Flow Measurement in Industrial and Biomedical Fields: A Review,” *IEEE Sens. J.*, vol. 17, no. 24, pp. 8196–8205, 2017, doi: 10.1109/JSEN.2017.2682929.

[10] D. S. Holder, *Electrical impedance tomography: methods, history and applications*. Bristol, UK: IOP Publishing, 2005.

[11] S. Leonhardt *et al.*, “Electric impedance tomography for monitoring volume and size of the urinary bladder,” *Biomed. Tech.*, vol. 56, no. 6, pp. 301–307, 2011, doi: 10.1515/BMT.2011.022.

[12] C. J. C. Trepte *et al.*, “Electrical impedance tomography (EIT) for quantification of pulmonary edema in acute lung injury,” *Crit. Care*, vol. 20, p. 18, 2015, doi: 10.1186/s13054-015-1173-5.

[13] R. J. Sadleir, T. Tang, A. S. Tucker, P. Borum, and M. Weiss, “Detection of intraventricular blood using EIT in a neonatal piglet model,” in *Proceedings of the 31st Annual International Conference of the IEEE Engineering in Medicine and Biology Society: Engineering the Future of Biomedicine, EMBC 2009*, 2009, pp. 3169–3172, doi: 10.1109/IEMBS.2009.5334510.

[14] R. Ogawa, M. R. Baidillah, S. Akita, and M. Takei, “Investigation of physiological swelling on conductivity distribution in lower leg subcutaneous tissue by electrical impedance tomography,” *J. Electr. Bioimpedance*, vol. 11, no. May, pp. 19–25, 2020.

[15] P. N. Darma, M. R. Baidillah, M. W. Sifuna, and M. Takei, “Real-time dynamic imaging method for flexible boundary sensor in wearable electrical impedance tomography,” *IEEE Sens. J.*, vol. 20, no. 16, pp. 9469–9479, 2020, doi: 10.1109/JSEN.2020.2987534.

[16] A. Peyman, C. Gabriel, and E. H. Grant, “Complex permittivity of sodium chloride solutions at microwave frequencies,” *Bioelectromagnetics*, vol. 28, no. 4, pp. 264–274, 2007, doi: 10.1002/bem.20271.

[17] M. W. Sifuna, M. R. Baidillah, D. Kawashima, P. N. Darma, E. O. Odari, and M. Takei, “Determination of sensitive frequency margin for aggregated protein concentration quantification by fd-electrical impedance tomography,” *Meas. J. Int. Meas. Confed.*, vol. 186, no. September, p. 110135, 2021, doi: 10.1016/j.measurement.2021.110135.

[18] M. E. Tipping, “Sparse Bayesian Learning and the Relevance Vector Machine,” *J. Mach. Learn. Res.*, vol. 1, no. 3, pp. 211–244, 2001, doi: 10.1162/15324430152748236.

[19] L. Shen *et al.*, “Sparse Bayesian learning for identifying imaging biomarkers in AD prediction,” in *Medical Image Computing and Computer-Assisted Intervention – MICCAI 2010.*, 2010, no. 6363 LNCS, pp. 611–618, doi: 10.1007/978-3-642-15711-0_76.

[20] Z. Zhang and B. D. Rao, “Sparse Signal Recovery with Temporally Correlated Source Vectors Using Sparse Bayesian Learning,” *IEEE J. Sel. Top. Signal Process.*, vol. 5, no. 5, pp. 912–926, 2011.

[21] S. Liu, J. Jia, Y. D. Zhang, and Y. Yang, “Image Reconstruction in Electrical Impedance Tomography Based on Structure-Aware Sparse Bayesian Learning,” *IEEE Trans. Med. Imaging*, vol. 37, no. 9, pp. 2090–2102, 2018, doi: 10.1109/TMI.2018.2816739.

[22] M. Vauhkonen, P. A. Karjalainen, and J. P. Kaipio, “A kalman filter approach to track fast impedance changes in electrical impedance tomography,” *IEEE Trans. Biomed. Eng.*, vol. 45, no. 4, pp. 486–493, 1998, doi: 10.1109/10.664204.

[23] N. K. Chada, M. A. Iglesias, L. Roininen, and A. M. Stuart, “Parameterizations for ensemble Kalman inversion,” *Inverse Probl.*, vol. 34, no. 5, 2018, doi: 10.1088/1361-6420/aab6d9.

[24] D. Andreuccetti, R. Fossi, and C. Petrucci, “An internet resource for the calculation of the dielectric properties of body tissues in the frequency range 10 Hz - 100 GHz,” *IFAC-CNR, Florence (Italy), Based data Publ. by C Gabriel al. 1996.*, 1997.

[25] S. Liu, R. Cao, Y. Huang, T. Ouypornkochagorn, and J. Ji, “Time Sequence Learning for Electrical Impedance Tomography Using Bayesian Spatiotemporal Priors,” *IEEE Trans. Instrum. Meas.*, vol. 69, no. 9, pp. 6045–6057, 2020, doi: 10.1109/TIM.2020.2972172.

[26] S. Liu, Y. Huang, H. Wu, C. Tan, and J. Jia, “Efficient Multitask Structure-Aware Sparse Bayesian Learning for Frequency-Difference Electrical Impedance Tomography,” *IEEE Trans. Ind. Informatics*, vol. 17, no. 1, pp. 463–472, 2021, doi: 10.1109/TII.2020.2965202.

[27] G. C. Cawley and N. L. C. Talbot, “Preventing over-fitting during model selection via bayesian regularisation of the hyper-parameters,” *J. Mach. Learn. Res.*, vol. 8, pp. 841–861, 2007.

[28] A. Adler and R. Guardo, “Electrical impedance tomography: Regularized imaging and contrast detection,” *IEEE Trans. Med. Imaging*, vol. 15, no. 2, pp. 170–179, 1996, doi: 10.1109/42.491418.

[29] W. S. Douglas and N. B. Simpson, “Guidelines for the management of chronic venous leg ulceration. Report of a multidisciplinary workshop,” *Br. J. Dermatol.*, vol. 132, no. 3, pp. 446–452, 1995, doi: 10.1111/j.1365-2133.1995.tb08681.x.

[30] J. Schöberl, “An advancing front 2D/3D-mesh generator based on abstract rules,” *Comput. Vis. Sci.*, vol. 1, no. 1, pp. 41–52, 1997, doi: 10.1007/s007910050004.

[31] C. Stick, P. Stöfen, and E. Witzleb, “On physiological edema in man’s lower extremity,” *Eur. J. Appl. Physiol. Occup. Physiol.*, vol. 54, pp. 442–449, 1985, doi: 10.1007/BF02337192.

[32] V. O. W. Man, G. S. Lepar, M. C. Morrissey, and J. K. Cywinski, “Effect of neuromuscular electrical stimulation on foot/ankle volume during standing,” *Med. Sci. Sports Exerc.*, vol. 35, no. 4, pp. 630–634, 2003, doi: 10.1249/01.MSS.0000058432.29149.08.

[33] R. Pethig and D. B. Kell, “The passive electrical properties of biological systems: Their

significance in physiology, biophysics and biotechnology," *Phys. Med. Biol.*, vol. 32, no. 8, pp. 933–970, 1987, doi: 10.1088/0031-9155/32/8/001.

[34] P. P. John, "The Role of Sodium in the Production of Edema," *N. Engl. J. Med.*, vol. 239, no. 10, pp. 353–362, 1948.

[35] T. K. Bera, "Bioelectrical Impedance Methods for Noninvasive Health Monitoring: A Review," *J. Med. Eng.*, vol. 2014, no. 381251, pp. 1–28, 2014, doi: 10.1155/2014/381251.

[36] B. J. Thomas, L. C. Ward, and B. H. Cornish, "Bioimpedance spectrometry in the determination of body water compartments: Accuracy and clinical significance," *Appl. Radiat. Isot.*, vol. 49, no. 5–6, pp. 447–455, 1998, doi: 10.1016/S0969-8043(97)00052-3.

[37] M. R. Chester, M. J. Rys, and S. A. Konz, "Leg swelling, comfort and fatigue when sitting, standing, and sit/standing," *Int. J. Ind. Ergon.*, vol. 29, no. 5, pp. 289–296, 2002, doi: 10.1016/S0169-8141(01)00069-5.

[38] P. Deurenberg and M. Deurenberg-Yap, "Validity of body composition methods across ethnic population groups," *Acta Diabetol.*, vol. 40, no. SUPPL. 1, pp. 246–249, 2003, doi: 10.1007/s00592-003-0077-z.

[39] M. Vauhkonen, D. Vadâsz, P. A. Karjalainen, E. Somersalo, and J. P. Kaipio, "Tikhonov regularization and prior information in electrical impedance tomography," *IEEE Trans. Med. Imaging*, vol. 17, no. 2, pp. 285–293, 1998, doi: 10.1109/42.700740.

[40] A. Adler *et al.*, "GREIT: A unified approach to 2D linear EIT reconstruction of lung images," *Physiol. Meas.*, vol. 30, no. 6, 2009, doi: 10.1088/0967-3334/30/6/S03.

[41] L. Fabrizi, A. McEwan, T. Oh, E. J. Woo, and D. S. Holder, "An electrode addressing protocol for imaging brain function with electrical impedance tomography using a 16-channel semi-parallel system," *Physiol. Meas.*, vol. 30, no. 6, 2009, doi: 10.1088/0967-3334/30/6/S06.

[42] R. Ogawa, M. R. Baidillah, P. N. Darma, D. Kawashima, S. Akita, and M. Takei, "Multifrequency Electrical Impedance Tomography with Ratiometric Preprocessing for Imaging Human Body Compartments," *IEEE Trans. Instrum. Meas.*, vol. 71, 2022, doi: 10.1109/TIM.2022.3166796.

[43] S. Cho and J. E. Atwood, "Peripheral edema," *Am. J. Med.*, vol. 113, no. 7, pp. 580–586, 2002, doi: 10.1016/S0002-9343(02)01322-0.

[44] B. Taji, A. D. C. Chan, and S. Shirmohammadi, "Effect of Pressure on Skin-Electrode Impedance in Wearable Biomedical Measurement Devices," *IEEE Trans. Instrum. Meas.*, vol. 67, no. 8, pp. 1900–1912, 2018, doi: 10.1109/TIM.2018.2806950.

[45] J. W. Bahk, H. Kim, K. Jung-Choi, M. C. Jung, and I. Lee, "Relationship between prolonged standing and symptoms of varicose veins and nocturnal leg cramps among women and men," *Ergonomics*, vol. 55, no. 2, pp. 133–139, 2012, doi: 10.1080/00140139.2011.582957.

[46] M. R. Baidillah, A. A. S. Iman, Y. Sun, and M. Takei, "Electrical Impedance Spectro-Tomography Based on Dielectric Relaxation Model," *IEEE Sens. J.*, vol. 17, no. 24, pp. 8251–8262, 2017, doi: 10.1109/JSEN.2017.2710146.

Chapter 7 Conclusions

7. Conclusions

7.1. Summary of Research

The aim of this thesis is to monitor extracellular fluid (ECF) in subcutaneous adipose tissue (SAT) for evaluating physiological edema.

In this regards, the novelties of present study are: 1) to evaluate physiological edema on conductivity distribution $\boldsymbol{\sigma}$ in lower leg subcutaneous tissue; 2) to study on the relationship between frequency-dependence and absolute conductivity value in the reconstructed image through the miniature EIT sensor as fundamental research towards developing data preprocessing; 3) to develop multifrequency EIT (*mf*-EIT) with a ratiometric preprocessing for boosting robustness under high conductivity contrast of biological tissue and suppressing excessive noise; 4) to monitoring of local-spatiotemporal change (LSTC) in the extracellular fluid (ECF) by time-variation-constraint sparse Bayesian learning (*tvc*SBL) implemented into frequency-difference EIT (*fd*EIT). The details of present study explained in this thesis can be summarized as follow:

Chapter 1

The background of this study was explained in detail. The physiology of edema, especially lymphedema, were explained with its recent monitoring techniques and problems. In this chapter, the main objectives to overcome the problems has been clarified.

Chapter 2

In order to solve the current issues and to deeply understand the physiological edema, the basic knowledge of electrical impedance tomography (EIT) for visualization measurement were explored. In this chapter, the EIT overview and the electrical properties of biological tissues have been clarified.

Chapter 3

In this chapter, the investigation of physiological swelling on conductivity distribution in lower leg subcutaneous tissue by EIT is described. The image-based reference EIT (IBR-EIT) with fat-weighted threshold method has been proposed in order to assess the physiological condition change or heterogeneity of subcutaneous adipose tissue (SAT) by localizing the abnormalities within the compartment. The proposed method is evaluated by a physiological swelling experiment with a wearable 16 EIT electrodes sensor where BIS is

applied as a comparative method. The experimental results show that the proposed IBR-EIT appears to identify the physiological swelling condition and effectively remove the unexpected background noise. Furthermore, the conductivity variation in SAT shows a good correlation with extracellular water volume change measured by BIS; the correlation coefficient $R^2 = 0.927$. In conclusion, the proposed method provides a great prospect for SAT assessment.

Chapter 4

In this chapter, the investigation of the relationship between frequency-dependence and absolute conductivity value in the reconstructed image is described through the miniature EIT sensor as fundamental research towards the development of data preprocessing. The use of 3D cell culture for tissue engineering and regenerative medicine applications often challenges conventional biochemical and optical assays. Impedance-based cellular assays have shown their potential to retrieve dielectric parameters about cell behaviour, such as viability, proliferation, and differentiation for 2D adherent cell culture. Herein, simultaneous 3D impedance imaging and viability measurements of multiple large (>2mm) 3D cell cultures embedded in collagen gels are demonstrated. The method is facilitated by low-resistance 3D printed scaffolds that can hold a 3D cell–gel system throughout cell culture while being transparent to impedance imaging. It is shown in silico and in vitro that frequency-difference electrical impedance tomography (*fd*EIT) can non-destructively and in a label-free way differentiate a variety of cell concentrations with a single miniature sensor in real time. Moreover, the relationships between frequency-dependence and absolute conductivity value in *fd*EIT image are numerically explained using multiple samples. This study paves the way toward developing *fd*EIT imaging for the quantitative and non-invasive evaluation of tissue engineering products.

Chapter 5

In this chapter, the development of multifrequency EIT (*mf*-EIT) with a ratiometric preprocessing for boosting robustness under high conductivity contrast of biological tissue and suppressing excessive noise is described. In addition to the micro-scale *fd*EIT as a cellular assay, the macro-scale *fd*EIT as point-of-care imaging is highly desired since reference data over time is not necessary. Reconstructing the structural images of human body compartments could be possible using electrical impedance tomography (EIT), but the reconstructed image deteriorates due to high conductivity contrast μ between anomaly and background. In this

chapter, a multifrequency EIT with a ratiometric preprocessing (ratiometric EIT) has been developed in order to minimize μ while maintaining high distinguishability without any *a priori* information. The preprocessing of ratiometric EIT is achieved by extending the framework of ratiometric methods that uses the ratio of two measurement signals. Based on the proposed ratiometric preprocessing, ratiometric frequency-difference adjacent EIT (*rfda*-EIT) is newly derived. The *rfda*-EIT is qualitatively and quantitatively evaluated by numerical simulation under the variant conditions of μ (= 95%-10%) and experiment with eight subjects' calves. As the results, the *rfda*-EIT scores the area ratio error of subcutaneous adipose tissue (SAT) 17.09% < ARE^{SAT} < 28.13%, the position error of bone tibia 0.14% < PE^{tibia} < 10.19%, the position error of bone fibula 9.51% < PE^{fibula} < 1.74%, and the correlation coefficients 0.79 < CC < 0.91 in the numerical simulation. The total-mean area ratio error <ARE^{SAT}> by the *rfda*-EIT is lower than the error by the classical frequency-difference adjacent EIT (*fda*-EIT) from 12.70% to 5.18% in the experiment. Moreover, the true positive rate TPR^{tibia} for the bone tibia detection by the *rfda*-EIT is increased from 50.0% to 87.5% as compared with the rate by the *fda*-EIT.

Chapter 6

In this chapter, the monitoring of local-spatiotemporal change (LSTC) in the extracellular fluid (ECF) by time-variation-constraint sparse Bayesian learning (*tvc*SBL) implemented into frequency-difference EIT (*fd*EIT) is described. Local-spatiotemporal change (LSTC) of frequency-difference conductivity distribution $\Delta\boldsymbol{\sigma}$ in extracellular fluid (ECF) has been monitored in subcutaneous adipose tissue (SAT) to evaluate leg edema by time-variation-constraint sparse Bayesian learning (*tvc*SBL) implemented into frequency-difference electrical impedance tomography (*fd*EIT) (*tvc*SBL-*fd*EIT). The *tvc*SBL-*fd*EIT has three steps which are Step 1: formulation of blocked column vector (BCV), Step 2: SAT separation by time variation constraint, and Step 3: temporal correlation extraction by hyperparameter learning. The *tvc*SBL-*fd*EIT is qualitatively and quantitatively evaluated by numerical simulation under the unstable-background fields and experiment with 15 subjects' calves. Two types of numerical simulations are conducted to model lymphedema (LE) and venous edema (VE) that cause LSTC in $\boldsymbol{\sigma}$ of subcutaneous tissue fluids in human calf phantom which consists of three parts: great saphenous vein (GSV) as ROI and SAT and muscle as background. From the results, LSTC in $\boldsymbol{\sigma}$ are clearly extracted only near GSV by the proposed method, even in a field where the time-varying $\boldsymbol{\sigma}$ in the background is large. Furthermore, the

accuracy of the proposed method is evaluated under the variant conditions of conductivity ratios of SAT and muscle relative to GSV, i.e., $\rho^{GSV/SAT}$ and $\rho^{GSV/muscle}$, respectively, and area ratio accuracy ARA^{GSV} is the highest in the case where $\rho^{GSV/SAT} = \rho^{GSV/muscle}$, which achieves $ARA^{GSV} = 2.241$ regardless of the values of $\rho^{GSV/SAT}$ and $\rho^{GSV/muscle}$. Moreover, the *tvc*SBL-*fd*EIT was applied to the monitoring of 15 subjects' calves along with an experimental protocol of prolonged standing and leg elevation. The spatial-mean conductivity $<\Delta\boldsymbol{\sigma}>^{SAT}$ in the separated SAT has a strong positive correlation with conventional impedance z^{BIA} by bioelectrical impedance analysis (BIA) (correlation coefficient $0.715 < R < 0.957$; $n = 15$, $p < 0.05$), which is decreased during the prolonged standing while $<\Delta\boldsymbol{\sigma}>^{SAT}$ is increased during the leg elevation. Frequency-dependency of $\Delta\boldsymbol{\sigma}$ is associated with LSTC of sodium ion concentration in ECF while the local maximum position of $\Delta\boldsymbol{\sigma}$ is associated with the great saphenous vein (GSV) position. Furthermore, the superiority of the proposed algorithm is numerically evaluated under the unstable-background fields.

7.1. Future Work

Based on this study, we recommend the following procedure to apply EIT as a new monitoring method for physiological edema assessment:

1) A fat-weighted threshold method is applied if appropriate to assess the physiological condition change or heterogeneity of subcutaneous adipose tissue (SAT).

2) Quantitative analysis in the field of current density and potential distribution is necessary to understand the feasibility of differentiation of multiple samples using frequency-difference electrical impedance tomography (*fd*EIT)

3) Ratiometric preprocessing is selected for boosting robustness under high conductivity contrast of biological tissue and suppressing excessive noise while maintaining high distinguishability without any *a priori* information.

4) Local-spatiotemporal change (LSTC) of frequency-difference conductivity distribution $\Delta\boldsymbol{\sigma}$ in extracellular fluid (ECF) is desired to be monitored in subcutaneous adipose tissue (SAT) to evaluate physiological edema by time-variation-constraint sparse Bayesian learning (*tvc*SBL) implemented into frequency-difference electrical impedance tomography (*fd*EIT) (*tvc*SBL-*fd*EIT).

We realize this study still has more work to be accomplished. According to the proposed results of this study, some promising consideration analysis of future development to expand

the capability of EIT towards the early diagnosis of lymphedema are as follows:

1) In the work of chapter 3, the increase in measurement speed must be taken into account since edema could have progressed even within one measurement due to the slow measurement speed. Since one of the advantages of EIT is its possibility for real-time monitoring, some approaches, such as sensitivity matrix calculation based on machine learning and prior learning of hyperparameters in SBL, will be investigated.

2) The simulations in Chapter 4 were very simple, even with multiple samples; therefore, analysis with more structurally and electrically complex geometries is desirable.

3) In the work of chapter 5, ratiometric preprocessing, optimization of a weighted average rather than just an average will be investigated since its weights apparently vary between individuals, which depends on the proportion of biological tissue.

4) In the work of chapter 6, the optimization of *tvc*SBL-*fd*EIT through the update of sensitivity matrix **J** (e.g., discrete cosine transform), which enhance the sparsity, as well as the extension of the exploited correlations towards the spatial and frequency correlations will be studied. Moreover, generalization of the SAT separation, i.e., the selection of the threshold "*c*", will be desired since *c* varies widely depending on the clinical conditions, which should be adopted according to the individual application. It is expected to vary depending on fat thickness, water content, the skin conditions with which the electrodes contact the subject, etc. Furthermore, instead of focusing only on changes within the SAT, some clinical applications may rather focus only on changes within the muscle. The *c* is heuristically determined as the 25th percentile of elements based on a priori information about the relationship between $\boldsymbol{\sigma}$ of SAT and other biological tissues such as muscle, which was sufficient for the current image reconstruction problem. However, the in-depth consideration of the theoretical approach to optimize the *c* will be investigated. As an example, given that the proposed method follows a Bayesian framework, we plan to investigate whether a statistical choice for *c* would improve the reconstruction performance.

5) All the physiological work must be noted with some limitations. For example, in the work of chapter 6, the first limitation is the small number of subjects, including 9 males and 6 females. The experiments in this chapter are mainly designed to investigate the performance of *tvc*SBL-*fd*EIT for monitoring LSTC of volume/concentration in ECF. Nevertheless, $\langle \Delta\boldsymbol{\sigma} \rangle^{SAT}$ in the separated SAT had a

significantly strong positive correlation with conventional impedance z^{BIA}; therefore, it would be ideal to repeat this study with larger groups. Moreover, the indirect effect due to sex and gender differences as well as occupational characteristics will be investigated in future studies since those factors may affect leg edema during prolonged standing. The second limitation is that only the impedance magnitude value is used in order to avoid the complexity in the sensitivity computation and data acquisition system. For a better understanding of frequency-dependency, dielectric properties should be incorporated into the analysis. A new reconstruction algorithm that enables joint optimization of spectroscopic and tomographic aspects is under consideration for biomedical monitoring modalities. Furthermore, validation of changes in the concentration of various extracellular fluid components with their dielectric properties during prolonged standing will be investigated.

6) Clinical tests to extend the capability of EIT for early diagnosis of lymphedema will be conducted.

Ethical approval and informed consent

According to Chiba University ethical code, all subjects gave written informed consent for the study after receiving a detailed explanation for the purposes, potential benefits, and risks associated with participation. All study procedures were conducted in accordance with the Declaration of Helsinki and research code of ethics of Chiba University, and were approved by the Committee for Human Experimentation of Chiba University. The number of ethical approvals for our experiments by the committee of human experimentation of Chiba University is 29-13.

Nomenclatures

Chapter 2

$\boldsymbol{\sigma}$	: Conductivity distribution
$\mathbf{V}$	: Boundary voltage
I	: Current
$\mathbf{Z}$	: Impedance in the measurement domain
$\boldsymbol{\Omega}$	: Measuement domain
$\partial\Omega$	: Domain boundary
$\boldsymbol{\varphi}$	: Electrical potential
ω	: Angular frequency
E	: Electric field
H	: Magnetic field
D	: Electric flux density
B	: Magnetic flux density
ε_r	: Relative permittivity
ε_0	: Vacuum permittivity
μ_r	: Relative permeability
μ_0	: Vacuum permeability
$\mathbf{J}$	: Sensitivity matrix
$u(i^e)$	: Potential field produced by injecting current i into the e-th electrode
$u(i^m)$	: Potential field produced by injecting current i into the m-th measured voltage pattern
v_m	: Measured voltage at m-th measured electrode pattern ($1 \leq m \leq M$)
σ_n	: Conductivity at n-th mesh ($1 \leq n \leq N$)
λ	: Regularization hyperparameter
it	: Iteration number
χ	: Characteristic function to specify conductivity

Chapter 3

$\boldsymbol{\sigma}$	: Conductivity distribution

Ω : Sensing domain

$\mathbf{V}$: Boundary voltage

$\mathbf{S}$: Sensitivity matrix

λ : Regularization hyperparameter

$\mathbf{R}$: Diagonal matrix

$\boldsymbol{\sigma}^{abs}$: Conductivity distribution reconstructed using absolute EIT

$<\boldsymbol{\sigma}^{fat}>$: Spatial-mean of the estimated conductivity distribution in SAT layer

$<\boldsymbol{\sigma}^{muscle}>$: Spatial-mean of the estimated conductivity distribution in muscle

$\boldsymbol{\sigma}^{diff}$: Difference in conductivity distribution compared to $\boldsymbol{\sigma}^{abs}$.

$\boldsymbol{\sigma}^{tdEIT}$: Conductivity distribution reconstructed using time-difference EIT

Chapter 4

$\boldsymbol{\sigma}$: Conductivity distribution

$\Delta\boldsymbol{\sigma}$: Conductivity changes

γ : Surface tension

z_m : Impedance

$\mathbf{Z}_{obj}$: Object frequency

$\mathbf{Z}_{ref}$: Reference frequency

$\Delta\mathbf{Z}$: Impedance difference

$\mathbf{J}$: Sensitivity matrix

$\mathbf{R}(\Delta\boldsymbol{\sigma})$: Regularization term

$||\cdot||_{TV}$: TV norm

k : Iteration number

Ω : Sensing domain

R_{max} : Diameter of the ROI circle

$\Delta\sigma_i^*$: n-th element of final conductivity distribution

$\Delta\boldsymbol{\rho}^*$: Normalized resistivity changes

j : Current density

φ : Electric potential

x : Position inside the simulated domain

Chapter 5

z_m : Raw impedance

z^{ref} : Reference impedance

$\boldsymbol{\sigma}$: Conductivity distribution

μ : Conductivity contrast

$\Delta\boldsymbol{\sigma}$: Conductivity changes

m : Measurement number ($1 \leq \zeta \leq M$)

n : Spatial resolution ($1 \leq n \leq N$)

ξ : Selected measurement number as a denominator ($1 \leq \xi \leq M$)

f : Frequency number ($1 \leq f \leq F$)

t : Time number

$e_{f,t}$: Spectral-temporal error

$\mathbf{S}$: Sensitivity matrix

Λ : Inverse operator

k : Iteration number

Ω : Sensing domain

opt : Symbol of optimal value

$*$: Symbol of ratiometric value

$\langle \cdot \rangle$: Symbol of average value

$\mathbf{L}$: Regularization matrix

λ : Regularization hyperparameter

χ : Characteristic function to specify conductivity

$\sigma^{bg}{}_f$: Background conductivity

$\sigma^{a}{}_f$: Anomaly conductivity

R : Radius

$\mathbf{r}$: Position vector from origin O ($\mathbf{r} = (x,y)$)

$\partial\Omega$: Domain boundary

δ : Noise on a circular measurement system

u : Voltage

E : Distinguishable region

ΔE : Changes of distinguishable region

Chapter 6

$\boldsymbol{\sigma}$: Conductivity distribution

$\mathbf{Z}$: Impedance

$\mathbf{B}$: Positive-definite matrix

z^{ref} : Reference impedance

$\boldsymbol{\gamma}$: Prior variance vector

t_k : Time number

$\Delta\boldsymbol{\sigma}$: Frequency-difference conductivity distribution

$\boldsymbol{\varepsilon}$: Noise matrix

$\mathbf{J}$: Sensitivity matrix

f_1 : Low-frequency

f_2 : High-frequency

Δk : Time step size in discretization

$\boldsymbol{\Sigma}^{pre}$: Prior covariance matrix

$\boldsymbol{\Sigma}^{post}$: Posterior covariance matrix

λ : Noise variance

$\boldsymbol{\nu}$: Temporal standard deviation image

c : Thresholding value

$\boldsymbol{\Theta}$: Hyperparameter matrix

$L(\boldsymbol{\Theta})$: Likelihood function

$Q(\boldsymbol{\Theta})$: Q-function

$iter$: Iteration number

β : Regularization parameter for temporal correlation

$\|\cdot\|_F$: Frobenius norm of a matrix

δ^{min} : Minimum error bound

$iter^{max}$: Maximum iteration number

z^{BIA} : Impedance measured by BIA

$\langle \widetilde{\Delta \boldsymbol{\sigma}} \rangle^{SAT}$: Normalized spatial-mean conductivity

L^{ECF} : Extracelluler fluid (ECF) volume

L^{ICF} : Intracellular fluid (ICF) volume

Na^{+ECF} : Sodium ion concentration in ECF

Na^{+ICF} : Sodium ion concentration in ICF

Acknowledgements

My deepest gratitude to my supervisor, **Prof. Masahiro Takei**, is his intensive advice, kindness, support, guidance, and assistance in completing this thesis and my extraordinary life towards the implementation of the technology. Without his guidance and support, I would not have been able to pursue my research life. My gratitude is dedicated as well to my supervisor at the University of Edinburgh, **Prof. Pierre-Olivier Bagnaninchi** and **Prof. Jiabin Jia,** who made my adventurous research indispensable in my life, including biotechnology combined with my mechanical engineering knowledge, and made my study abroad precious surrounded by leading international researchers.

I would like to dedicate this achievement to my dear parents, **Yoshio Ogawa** and **Noriko Ogawa**, my dear brothers, **Yoshika Ogawa** and **Yuto Ogawa**, and my beloved girlfriend, **Hina Shibata**. Without their love, supports, and encouragement during this journey, I would not have been here at this moment.

Immeasurable appreciation and most profound gratitude for the help and support are extended to the following persons who, in one way or another, have contributed to making this study possible:

I would like to send my gratitude to **Prof. Shinsuke Akita**, **Prof. Mariko Masujima**, **Dr. Marlin Ramadhan Baidillah**, **Dr. Panji Nursetia Darma**, and **Dr. Daisuke Kawashima** for their help and advice. Also, my deepest gratitude to all members of Takei Laboratory of Chiba University, Japan, for their warmness and never-ending support: Dr. Prima Asmara Sejati, Dr. Sun Bo, Ms. Reiko Oike, Mr. Tomoki Asazuma, Mr. Mutsumi Satoh, and those who helped me with my experiments and business development. At the same time, I wish to express my gratitude to **Ms. Toshie Sano**, the secretary of our laboratory, for her special concern and invaluable support for administrative matters as well as her treasuring suggestions and instructions for student life. Not to forget, I would like to send my gratitude to my seniors and staff at Chiba University. They always support me during this journey.

Moreover, I would like to send my gratitude to **Dr. Hancong Wu** and **Dr. Amelia Hallas-Potts**, for their help and advice. Also, my deepest gratitude to all members of the Scottish Centre for Regenerative Medicine for their warmness and never-ending support: Dr. Jonathan H. Mason, Dr. Graham Anderson, Dr. Yunjie Yang, and those who helped my study abroad. Not to forget, I would like to send my gratitude to my seniors and staff at the

University of Edinburgh. They always support me during this journey.

Furthermore, I would like to gratefully acknowledge the support of the “Tobitate Ryugaku JAPAN Nihondaihyou Program” Scholarship from JASSO and the support of the “Research Fellowships for Young Scientists (DC1)” Fellowship from JSPS.

Finally, I would like to thank our lab members from Japan and other countries for their kindest support during the journey. They always encouraged me to get rid of difficulties and troubles. Therefore, I would not have accomplished the present achievement without their selfless love and understanding.

Published Journal Paper

1. **Ryoma Ogawa**, Marlin Ramadhan Baidillah, Shinsuke Akita, Masahiro Takei, “Investigation of Physiological Swelling on Conductivity Distribution in Lower Leg Subcutaneous Tissue by Electrical Impedance Tomography”, Journal of Electrical Bioimpedance, 11-1, 19-25, 2020.
2. **Ryoma Ogawa**, Amelia Hallas-Potts, Hancong Wu, Jiabin Jia, Pierre-Olivier Bagnaninchi, “Measuring 3D cell culture viability in multiple 3D printed scaffolds within a single miniature electrical impedance tomography sensor”, Advanced Engineering Materials, 23-10, 2100338, 2021.
3. **Ryoma Ogawa,** Marlin Ramadhan Baidillah, Panji Nursetia Darma, Daisuke Kawashima, Shinsuke Akita, and Masahiro Takei, “Multifrequency Electrical Impedance Tomography with Ratiometric Preprocessing for Imaging Human Body Compartments,” IEEE Transactions on Instrumentation and Measurement, 71, 1-14, 2022.
4. 小川良磨，秋田新介，武居昌宏，”スパースベイズ学習(SBL)による時間・空間局所的変化を抽出できる電気インピーダンストモグラフィ(EIT)の画像再構成アルゴリズム”，日本機械学会論文集（生体工学，医工学，スポーツ工学，人間工学）88-910, 22-00090, 2022.

   Ryoma Ogawa, Shinsuke Akita, Masahiro Takei, “Image reconstruction algorithm of spatiotemporal local change-extractable electrical impedance tomography(EIT) by sparse bayesian learning (SBL),”Transactions of the Japan Society of Mechanical Engineers (JSME), 88-910, 22-00090, 2022 (in Japanese).